Propagation of Cosmic Rays -
Studying supernova remnants as sources for the galactic flux and the influence of the solar magnetic field

Dissertation

zur Erlangung des Grades eines
Doktors der Naturwissenschaften
in der Fakultät für Physik und Astronomie
der Ruhr-Universität Bochum

vorgelegt von

Mike Kroll

geboren in

Unna

Bochum, Juni 2017

1. Gutachter:	Prof. Dr. Julia Becker Tjus
2. Gutachter:	PD Dr. Horst Fichtner

Datum der Disputation:	19. Juli 2017

» *Natur ist überall, in uns und außer uns; es gibt nur etwas, das nicht ganz Natur ist, sondern vielmehr ihre Überwindung und Deutung: die Kunst.* «

Franz Marc

Contents

Acknowledgements **v**

1 Introduction **1**

2 Cosmic Rays **5**

2.1 The primary cosmic ray spectrum 6

2.2 Acceleration processes 9

2.2.1 Fermi acceleration 11

2.2.2 Second order Fermi acceleration 12

2.2.3 First order Fermi acceleration 16

2.3 Stellar evolution and supernova explosion 18

2.4 Propagation of cosmic rays 23

2.4.1 Single particle propagation 24

2.4.2 Multi particle propagation 25

2.4.3 Crank-Nicholson method 26

2.4.4 The Runge-Kutta algorithm 27

3 Detectors in Astroparticle Physics **29**

3.1 Gamma-rays and their detection 30

3.1.1 Tibet AS-Gamma Experiment 31

3.2 Neutrinos 32

3.3 The IceCube Neutrino Observatory 33

3.3.1 Cherenkov radiation 36

3.3.2 Neutrino detection with IceCube 36

3.3.3 High energy neutrinos detected with IceCube 37
3.4 The AMS-02 detector 39

4 The solar magnetic field 41
4.1 Solar cycle 42
4.2 Sun spot number and features 42
4.2.1 The latitude diagram 42
4.2.2 Bipolar regions 44
4.3 The Zeeman effect and its application 45
4.3.1 Zeeman splitting 45
4.3.2 Magnetograms - Applied Zeeman effect 48
4.4 Potential Field Source Surface Model 49
4.4.1 General information on the model 49
4.4.2 Basic concept 50
4.4.3 Advantages & critics of the PFSS model 53
4.5 Sun shadow of cosmic rays 55
4.5.1 Basic concept and benefits of a Sun shadow analysis 55
4.5.2 Results of Sun shadow analyses of IceCube and Tibet-III . . 56

5 Supernova remnants as cosmic ray sources 59
5.1 Propagation in GALPROP 60
5.1.1 Gamma-ray measurements and corresponding cosmic ray spectra 61
5.1.2 Propagation of SNR spectra toward Earth 63
5.1.3 Individual SNR normalization 67
5.1.4 Cosmic ray nuclei 68
5.1.5 GALPROP settings 69
5.2 Results and conclusions 72
5.2.1 Validation of the method 72
5.2.2 Results for the individual SNRs 77
5.2.3 Discussion of uncertainties 78
5.3 Discussion & outlook 83
5.3.1 Discussion 83
5.3.2 Outlook 85

6 Simulating the Sun Shadow **87**
6.1 Setup of the simulation 88
6.2 Test of simulations 89
6.2.1 Homogeneous field 89
6.2.2 The ideal dipole field 91
6.3 Description of the method 95
6.3.1 Advantages and disadvantages 95
6.4 Study of the solar magnetic field 96
6.4.1 Solar activity 97
6.4.2 Including the magnetic field in the simulation 98
6.4.3 The magnetic field of December 2015 98
6.5 Simulation of the solar cosmic ray shadow 100
6.5.1 The cosmic ray Sun shadow 101
6.5.2 Averaged relative deficit 105
6.5.3 Averaged total absorption 107
6.6 One-dimensional analysis of the shadow 108
6.6.1 Temporal behavior of the shadow depth 111
6.7 Correlation of start and end positions 112
6.8 Summary & Outlook 114

7 Conclusion & Outlook **117**
7.1 Conclusion 117
7.2 Outlook 120

Bibliography **123**

Appendix **139**
Cosmic ray shadow 140
Deficit Analysis 149
Total Absorption 150
One Dimensional Analysis 151

Acknowledgements

Throughout the doctoral program at the Ruhr-Universität Bochum at the chair of Plasma- and Astroparticle Physics I was allowed to collaborate with wonderful people all over the world. The entire three years have become an important chapter in my own life that I do not wish to miss. At this point, I would like to say thanks to all people that have influenced my work:

Ich möchte mich sehr herzlich bei meiner Doktormutter Prof. Dr. Julia Becker-Tjus bedanken. Die unterstützenden Gespräche über die Analysen während der gesamten Zeit waren von bester Qualität und halfen mir sehr. Auch die zahlreichen Konferenzen in Europa und Amerika sowie Forschungsaufenthalte prägten meine Zeit als Doktorand zum Besten.

Ein weiteres herzliches Dankeschön gilt meinem Zweitbetreuer und -gutachter PD Dr. Horst Fichtner. Die bereichernden Gespräche bezüglich meiner Arbeit halfen mir sehr und erweiterten mein physikalisches Verständnis.

Vielen Dank an die gesamte Arbeitsgruppe TP IV, die mich in allen Fragen rund um meine Dissertation und Analysen mit tiefgreifendem Wissen unterstützte. Besonders bedanken möchte ich mich bei Fabian Bos, mit dem ich gemeinsam studierte, im Auslandssemester war und promovierte. Vielen Dank für schöne und unvergessliche Zeit.

I would like to warmly thank the entire IceCube group in Madison for the hospitality and being so supportive. I wish to thank Francis Halzen, Markus Ahlers

and Paolo Desiati for fruitful discussions and comments about my work. Another thanks goes to Carlos A. Argüelles Delgado for being a good friend and our good physics talks.

I am deeply grateful to James R. Doing for his language support and corrections, and, most of all, for being a great friend and host whenever I was in Madison.

Ein besonderes Dankeschön geht an meine Eltern Sigrid und Christof für Eure uneingeschränkte Unterstützung in allen Bereichen. Vielen Dank Marvin, für all unsere unterstützenden Gespräche und Ermutigungen. Ohne Euch als Stärkung an meiner Seite wäre diese Zeit nicht möglich gewesen. Ein weiteres herzliches Dankeschön gilt meiner Freundin Lais, die mich in dieser Zeit auch besonders unterstützt hat.

This work utilizes data obtained by the Global Oscillation Network Group (GONG) Program, managed by the National Solar Observatory, which is operated by AURA, Inc. under a cooperative agreement with the National Science Foundation. The data were acquired by instruments operated by the Big Bear Solar Observatory, High Altitude Observatory, Learmonth Solar Observatory, Udaipur Solar Observatory, Instituto de Astrofísica de Canarias, and Cerro Tololo Interamerican Observatory.

Dedicated to my parents Sigrid and Christof
and
to my brother Marvin

CHAPTER 1

Introduction

Investigations into particles of astronomical origin and particles interacting with environments in the Universe belong to the field of astroparticle physics. There are at least three different classes of particles in the Universe that can be used to retrieve information about their origin, composition, and energy. Experiments analyze the information brought to Earth by charged cosmic rays, radiation covering different energy bands, and neutrinos. Each of these have their advantages and disadvantages. Cosmic rays, for example, are charged, and galactic magnetic fields cause a deflection such that on Earth a nearly isotropic flux is measured. Due to this deflection, no claims with regard to their source are possible, however, their energy can be measured, providing valuable information about sources in general. Gamma-rays are not charged and can carry information about their origin. Combined with the spectrum, they are excellent candidates for investigating galactic and extragalactic objects. The gamma-ray signal, however, is ambiguous because leptonic processes may contribute to a hadronic signal. The third class is neutrinos. These elementary particles are uncharged and they barely interact with matter. In particular, neutrino detection is a very recent method in the field of astroparticle physics, because extensive research regarding the construction site and the detector design are required.

The focus of this thesis is the study of cosmic rays and their propagation. After first being detected in the early 20th century, there was rapid development in the analysis of the spectrum and composition of cosmic rays. With better understanding and experiments adjusted to higher sensitivities, further aspects have been studied, including the identification of their origin and the modeling of their propagation through space.

The explosion of a star releases an enormous amount of energy, which is assumed to also transmitted to cosmic rays. One goal of this thesis is to investigate whether this amount is sufficient to explain the cosmic ray flux up to 10^{15} eV. Gamma-ray data are used to identify a sample of potential cosmic ray emitters. These sources are the hypothesis that supernova remnants can reproduce the observed cosmic ray spectrum.

The second goal of this thesis is the simulation of the deficit in the cosmic ray flux when the detector is directed toward the Sun. Experimental data provided by the IceCube Neutrino Observatory, which also allows for an indirect measurement of cosmic rays, has seen this shadow. Due to the temporal variation in the magnetic flux, a temporal effect was also observed in the Sun shadow analysis. In this thesis, the measurement of the magnetic field serves as an input parameter for the simulation, and cosmic rays can be propagated through the field. Previous work has been supplemented with a larger energy range and includes the rotation of the Sun. The shadow can be simulated averaged over a month.

The outline of this thesis is the following: Chapter 2 gives an introduction to the field of astroparticle physics, in which the focus lies on cosmic ray particles, in particular their sources, acceleration, and propagation. The working principles of gamma-ray, neutrino, and cosmic ray detectors is described in Chapter 3. In Chapter 4, the solar magnetic field is investigated. Here, the solar cycle and the Sun spot number are related to the strength of the magnetic field. Moreover, mechanisms used to measure the magnetic field are presented, and the Potential Field Source Surface model is introduced as a representative model for the solar magnetic field. This chapter is concluded with a presentation of current findings of Sun (and Moon) shadow analyses. In Chapter 5, supernova remnants are investigated as sources for providing the cosmic ray flux up to an energy of 10^{15} eV measured on

Earth. Gamma-ray measurements have identified 21 remnants with an hadronic component in their spectrum, and their total energy gives an estimate of the total energy in cosmic rays. The ejected cosmic rays are propagated to Earth using the propagation code GALPROP. The spectrum obtained is compared to measurement data. In Chapter 6, the deficit of cosmic ray data when pointing the detector toward the Sun is simulated. The effects of the magnetic field are investigated for three different energies, $E_{\mathrm{CR}} = 10$ TeV, $E_{\mathrm{CR}} = 40$ TeV, and $E_{\mathrm{CR}} = 100$ TeV. The time period used is in accordance with the visibility of the Sun for the IceCube detector and is thus November through February. Ten years are analyzed. The overall summary and conclusion of this thesis are given in Chapter 7, along with an outlook for future possibilities and relevance of these findings to further investigations. The Appendix includes detailed plots of the Sun shadow analysis.

CHAPTER 2

Cosmic Rays

Cosmic rays are defined as charged nuclei that are of astrophysical origin. They can be divided into primaries and secondaries. Primaries originate from and are accelerated at a source while secondaries are products of primary particle interactions with interstellar gas. Primary cosmic rays include protons, in particular, but also heavier nuclei such as helium, carbon, oxygen, and even iron. The nuclei of lithium, beryllium, and boron, provided they are not a product of the nucleosynthesis in a star, belong to the group of secondaries [1].
The detection method used to observe cosmic rays depends upon their energy. Experiments are arranged with an increased sensitivity in the desired energy range. Balloon flights, satellites, and ground-based detection arrays contribute to the observations. For ground-based arrays, a high altitude provides the advantage of having less atmosphere with which the cosmic rays interact.

The existence of cosmic rays was discovered by Victor Hess and others, who studied ionizing radiation in the early 20th century. This radiation increased as the balloon carrying the experiment rose, and he thus concluded the existence of an extraterrestrial radiation, see [2]. Hess was awarded the 1936 Nobel Prize in Physics [3]. Reviews of cosmic rays can be found in e.g. [4–6].

2.1 The primary cosmic ray spectrum

The energy spectrum of cosmic rays describes the differential number of particles with an energy E per energy $\mathrm{d}E$. Mathematically, it can be represented by a broken power law, which indicates non-thermal processes as these result in such a spectrum, see e.g. [7]. Generally, the flux is a function of energy per units of area, time, and solid angle. The differential flux can be written as [8]

$$\frac{\mathrm{d}N}{\mathrm{d}E} \propto E^{-\alpha_{\mathrm{CR}}} \tag{2.1.1}$$

where the spectral index α_{CR} is broken (see e.g. Ref. [8] and references therein)

$$\alpha_{\mathrm{CR}} \approx \begin{cases} 2.67 & \text{for} \quad \log(E/\mathrm{eV}) < 15.4 \\ 3.10 & \text{for } 15.4 < \log(E/\mathrm{eV}) < 18.5 \\ 2.75 & \text{for } 18.5 < \log(E/\mathrm{eV}). \end{cases} \tag{2.1.2}$$

The differential spectrum is shown in Fig. 2.1 as a function of energy. It is very steep and therefore weighted by the factor $E^{2.6}$ GeV for visual purposes. In doing so, the representative features in the spectrum, such as *knee* and *ankle*, are easier to identify.

The *knee* can be found within the energy range $10^{15} < E < 10^{16}$ eV, where the spectrum breaks and is described by a greater power law index. At higher energies, the spectrum is steeper until it reaches the *ankle* at $E \approx 10^{18.5}$ eV, where the spectrum flattens again. A less prominent change in the shape of the spectrum is the *second knee*, which can be found at about $E \approx 8 \cdot 10^{16}$ eV, reported by the KASCADE-Grande group, among others [9].

Scientists are still debating where these particles come from, which sources are capable of accelerating particles to even the highest energies, and, lastly, what causes the discriminable features in the spectrum. Supernova remnants find most acceptance for accelerating cosmic rays up to the *knee* energy, and the steepening is explained by the lack of a source that can accelerate this number of particles to higher energies, see e.g. [1]. Besides supernova remnants, the propagation of particles through the Galaxy and their confinement in this object might also contribute to the spectrum [10]. Further, it is believed that particles with energies up to the

ankle are of galactic origin, while the highest energies must be extragalactic.

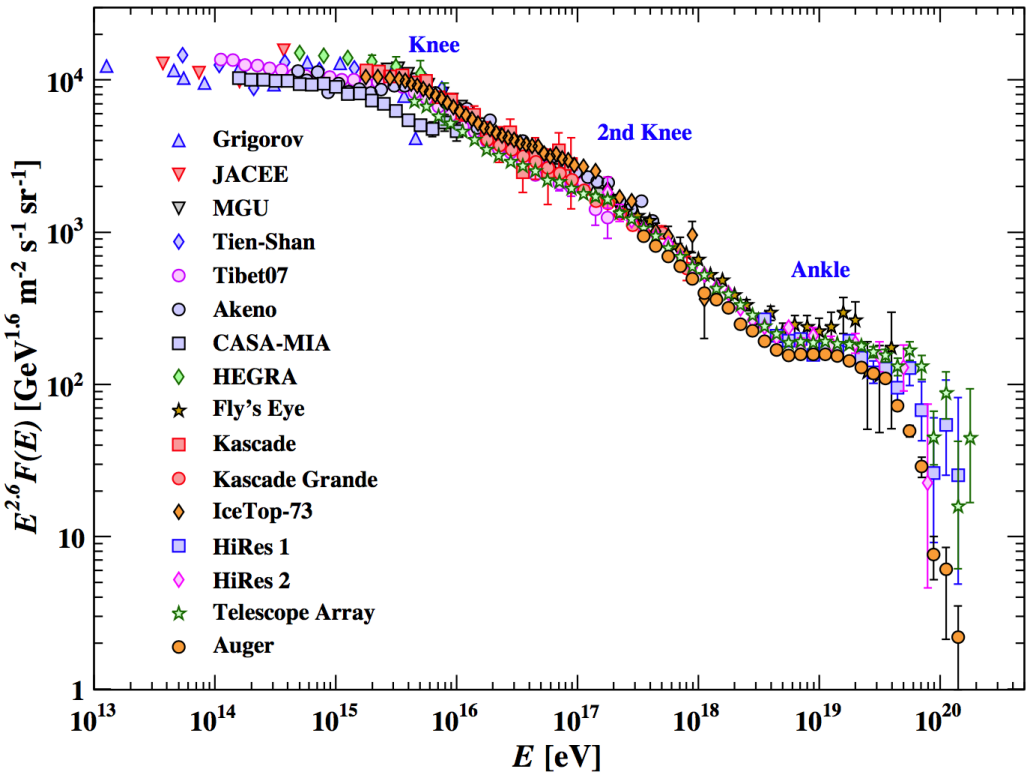

Figure 2.1: *The combined all-particle Cosmic Ray energy spectrum as a function of energy. Each data point has been measured in air shower experiments. Figure taken from [1].*

In contrast to the galactic flux below 10^{18} eV, the *ankle* might reflect the fact that the extragalactic flux provides a contribution at the highest energies [11]. The interaction of protons with the cosmic microwave background (CMB) at higher energies, $p\gamma_{\mathrm{CMB}} \rightarrow \Delta^{+}$, is a possible reason for the cutoff of the spectrum at $E \approx 5 \cdot 10^{19}$ eV. This is also known as the Greisen-Zatsepin-Kuzmin (GZK) cutoff, see [12, 13].

Spectral measurements of cosmic rays with energies $E_{\mathrm{CR}} \leq 100$ TeV can be conducted directly using balloons and satellites. The balloon experiment CREAM reports a break in the nuclei spectra in the case of helium and heavier nuclei. This break appears in the energy range 100 GeV $\leq E_{\mathrm{CR}}/A \leq 1$ TeV, where A is the atomic mass number, see e.g. [14, 15]. The recent release of updated spectra of proton [16] and helium [17] could confirm the break in the latter in both elements at even higher significance [18].

The first detailed study of the cosmic ray composition in the *knee* region was provided by the experiments KASCADE and KASCADE-Grande, see [19, 20]. This experiment is sensitive to energies around the *knee* through the measurement of air showers, induced by high-energy cosmic rays. The data allow for an occurrence of a break in the iron spectrum at approximately $E_{\mathrm{CR}} \approx 10^{17}$ eV. Such a feature favors a heavy nuclei composition at energies greater than the *knee*, which is predicted by a cut-off in the spectrum proportional to the atomic number. The data of the *iron-knee*, spectral behavior, and composition especially at high energies are associated with high uncertainty, and hence, analytical techniques and experimental setups must therefore be improved in the future.

The IceCube experiment provides a valuable contribution for the research of cosmic rays by using the air shower array IceTop, from which composition studies will benefit, see in particular [21]. The composition has been analyzed at even higher energies by the Auger collaboration. Studies in the energy range 10^{15}eV $\leq E_{\mathrm{CR}} \leq 10^{17}$ eV report an increasing of particle masses, while in the subsequent energy decade the mass becomes lighter again. Auger data lets assume a heavier composition and is compatible data obtained from TA [22] and HiRes [23].
Indeed, their results show a heavy nuclei contribution with masses $A > 4$ for energies above the *ankle*, i.e. $10^{18.5}$ eV, see [24, 25].

2.2 Acceleration processes

The measured cosmic ray data raise the question of how particles can reach such high energies and what the underlying accelerating processes are. In an initial approach, general conditions should be defined for a source that accelerates particles. The geometry of the source defines a region in which the particles are accelerated. Hence, the maximum energy is related to both the geometrical size of the source and to its power, i.e. how energetic the source is in terms of accelerating particles. If the Larmor radius r_L becomes larger than the size L of the accelerator, the particles escape. This limit defines the maximum momentum

$$L \sim r_L = \frac{p_{\max}}{ZeB}. \tag{2.2.1}$$

The maximum energy gained, including $\beta = v/c$, then yields

$$E_{\max} = \beta c Z e B L. \tag{2.2.2}$$

In the above equations, Ze is the charge of the particle and B the magnetic field strength. The parameter $E_{\max}$ is the maximum energy a particle can acquire through acceleration. This relation is also known as the *Hillas criterion*, see [26].

Figure 2.2 shows the Hillas plot that relates the magnetic field to the extension of the source. Using the Hillas criterion, Eq. (2.2.2), the absolute maximum energy of particles in an accelerator of size L can be determined. The plot shows one line representing the acceleration of protons to $E_{\mathrm{p}} = 10^{21}$ eV, as well as the acceleration of iron nuclei to $E_{\mathrm{Fe}} = 10^{20}$ eV, represented by the lower solid line.
However, the Hillas criterion is only a necessary condition, the proper description of the acceleration process determines the actual maximum energy, with an absolute limit at the Hillas criterion. Another limiting factor are energy losses. As cosmic rays are charged, they can lose energy through radiation when they are deflected and decelerated from their original trajectory. The interaction with other particles or gamma-rays will also lead to a reduction in energy. Therefore, in a successful acceleration, the energy gain processes dominate over the losses [27]. In the following subsections, the different acceleration mechanisms will be described in detail.

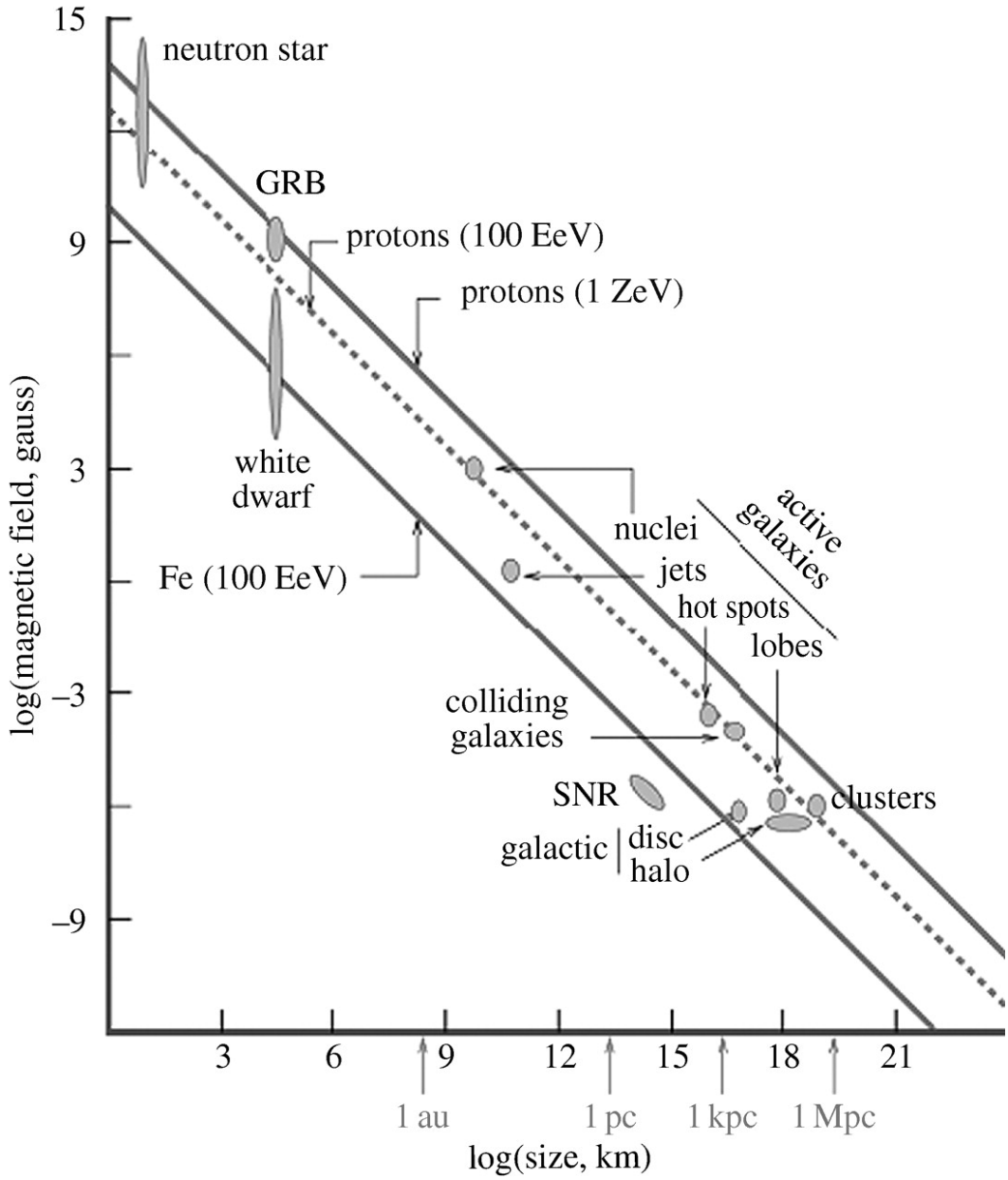

Figure 2.2: *The Hillas Plot. The magnetic field versus the size of the source is shown in a double logarithmic scale. Figure taken from [28].*

2.2.1 Fermi acceleration

Enrico Fermi proposed an acceleration mechanism of charged particles in astrophysical shocks, and publishing his idea in his article "*On the origin of the Cosmic Radiation*", see [29]. Technically, this mechanism works for both electrons/positrons and protons/heavier nuclei, referred to as leptonic and hadronic acceleration, respectively.

There are two Fermi acceleration types, namely that of second and first order. Mainly, a particle is assumed to gain a proportional amount of energy to its current energy when a specific interaction occurs [30],

$$\Delta E = \xi E. \tag{2.2.3}$$

After n cycles, the energy of the particle is

$$E = E_0(1+\xi)^n, \tag{2.2.4}$$

or, expressed by the number of cycles that a particle needs to reach energy E

$$n = \frac{\ln(E/E_0)}{\ln(1+\xi)}. \tag{2.2.5}$$

The number of particles that have been accelerated to an energy greater than E is [30]

$$N(>E) \propto \sum_{m=n}^{\infty} (1 - P_{\text{esc}}), \tag{2.2.6}$$

with P_{esc} as the probability of a particle to escape the acceleration region. The combination of Eqs. (2.2.5) and (2.2.6) leads to the energy distribution

$$N(>E) \propto \frac{1}{P_{\text{esc}}} \left(\frac{E}{E_0}\right)^{-\alpha} \tag{2.2.7}$$

$$\alpha = \frac{\ln\left(\frac{1}{1-P_{\text{esc}}}\right)}{\ln(1+\xi)} \approx \frac{P_{\text{esc}}}{\xi}. \tag{2.2.8}$$

The above equations show that a system in which particles undergo a repeated acceleration indeed lead to a power-law spectrum. The index, however, is dependent upon the source. With this generalized concept, two kinds of acceleration have been formulated.

2.2.2 Second order Fermi acceleration

This type of acceleration was originally proposed by Fermi [29], and *second order* refers to the end result. The basic idea concerns particles that travel through space and hit dense plasma clouds containing a turbulent magnetic field. The incoming particle can hit the cloud basically from all directions. When velocity vector orientation is parallel the particle can catch up to the cloud, since its velocity is close to the speed of light and thus much greater than the cloud's velocity. Assuming that the particle is always reflected by the cloud, only in the head-on collision scenario will the particle gain energy, because the cloud basically has an infinite mass, and the particle gains the cloud's kinetic energy. In the other case, the particle will suffer a loss in energy. A visual representation of this idea is presented in Fig. 2.3. The scattering does not happen as a result of particle interactions, as the cloud is not dense enough. Also, such interactions would result in thermalization and an energy gain would not be the result. The incident cosmic ray particle will be deflected by the magnetic field contained in the cloud.

Gaisser shows in his book [31] a step by step calculation of the second order Fermi acceleration and in the following the major steps shall be picked up on. In analogy to Fig. 2.3 (a) E_1 is the incident particle energy and as it enters the cloud the particle scatters off the irregular magnetic fields elastically, and after a few such scatterings the particle moves along with the cloud. Hence, in the rest frame the total energy of the particle is

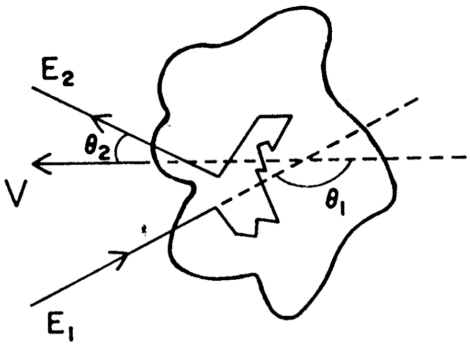

(a) Sketch of a particle entering a gas cloud with an angle $180° - \theta_1$*. The particle is scattered off of the cloud by its magnetic field and hence gains energy. Figure taken from [31].*

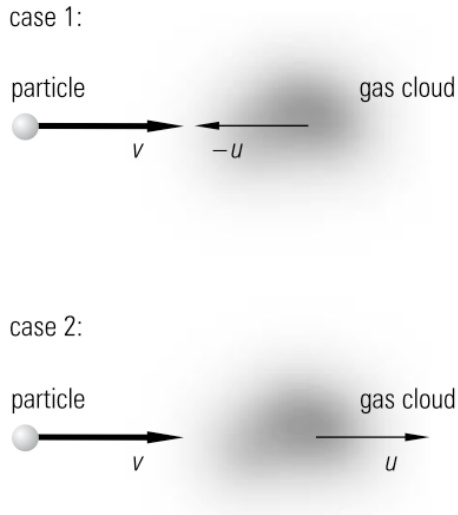

(b) Sketch of two simplified cases of how a particle can hit a moving gas cloud. In case one, the velocity vectors are oppositely oriented, in case two, particle and cloud propagate into the same direction. Figure taken from [30].

Figure 2.3: *This figure explains Fermi's idea graphically. In* ***(a)*** *the detailed interaction of a particle is shown. It can be imagined that it is not reflected only once but rather on a number of magnetic field walls. The sketch in* ***(b)*** *shows in an 1-dimensional scenario the two different options of how the particle can interact with the cloud. The reality, in a 3D case, is naturally more complicated.*

$$E_1' = \gamma E_1(1 - \beta \cos\theta_1), \tag{2.2.9}$$

with θ_1 the as the angle between the velocity vectors if the incoming particle and the cloud. Since all scatterings conserve energy it is $E_2' = E_1'$ with E_2' the particle's energy after leaving the cloud. But from the view point of an external observer the leaving energy is

$$E_2 = \gamma E_2'(1 + \beta \cos\theta_2'). \tag{2.2.10}$$

The combination of the above two equations and $\beta = V/c$ with the speed of the gas cloud V yields

$$\frac{\Delta E}{E_1} = \frac{1 - \beta\cos\theta_1 + \beta\cos\theta_2' - \beta^2\cos\theta_1\cos\theta_2'}{1-\beta^2} - 1. \tag{2.2.11}$$

For a hit with the shock front of the cloud the mean energy change has to be averaged over the possible angles of both incoming and outgoing in order to obtain the fractional energy gain ξ, see Eq. (2.2.3). It has to be assumed that there is no preferred direction for the outgoing angle θ_2 in the rest frame of the cloud, and thus

$$\frac{\mathrm{d}n}{\mathrm{d}\cos\theta_2'} = \text{const.} \qquad \text{for } -1 \leq \cos\theta_2' \leq 1. \tag{2.2.12}$$

This result concludes an isotropic flux and this means for Eq. (2.2.11)

$$\frac{\langle\Delta E\rangle_2}{E_1} = \frac{1-\beta\cos\theta_1}{1-\beta^2} - 1. \tag{2.2.13}$$

In the next step the incoming angle has to be averaged. One way is to calculate the probability for a collision with the cloud. This probability is proportional to the relative velocity of the cloud and the particle $\delta v = c - V\cos\theta_1$. Again, with no preferred incoming direction, the normalized distribution is [31]

$$\frac{\mathrm{d}n}{\mathrm{d}\cos\theta_1} = \frac{c - V\cos\theta_1}{2c} \qquad \text{for } -1 \leq \cos\theta_1 \leq 1. \tag{2.2.14}$$

Now, with $\langle\cos\theta_1\rangle = \frac{1}{3}V/c$ the fractional energy yields

$$\xi = \frac{\langle\Delta E\rangle_{1,2}}{E_1} = \frac{1+\frac{1}{3}\beta^2}{1-\beta^2} - 1. \tag{2.2.15}$$

In the case of a not relativistically moving cloud Eq. (2.2.15) can be approximated to

$$\xi \approx \frac{4}{3}\beta^2. \tag{2.2.16}$$

In the discussion of the above equation, as the end result of the second-order Fermi acceleration, it becomes clear that the energy gain is not very big due to the small β and thus the acceleration is a slow process. Equation (2.2.11) even allows for an energy loss, namely when the particle hits the cloud head-on but propagates through the magnetic fields to the end and exits the cloud at the back.

It can be shown that the spectral index calculates to [31]

$$\alpha \approx \left(\frac{4}{3}c\ \beta^2\ \varrho_c\ \sigma_c\ T_{esc}\right)^{-1}, \tag{2.2.17}$$

with the cloud's density ϱ_c, cross section σ_c and the escape time of particles out of the Galaxy $T_{esc} \approx 10^7$ years [31]. The spectral index is thus not unique and can vary extremely due to the large number of different combinations of the parameters in Eq. (2.2.17). This actually contradicts observations of a constant power-law behavior over many decades.

The previously discussed slow energy gain along with the fairly undetermined spectral index makes this process not very attractive as the primary acceleration process. For propagation simulations through the Galaxy it is still used despite the criticism and is known as the diffusive re-acceleration [32].

2.2.3 First order Fermi acceleration

The Fermi acceleration of the first order refers again to the end result. It will be shown that $\xi \propto \beta$, and hence the acceleration will be much more efficient. In astrophysical shocks, when an interstellar gas cloud is hit by another, which moves faster than the speed of sound in the hit cloud, particles undergo a repeated acceleration of this kind. This quite special constellation of a fast moving incoming plasma occurs for example in the event of a star explosion. It can also explain strong and irregular magnetic fields, in which collisionless scatterings dominate over particle interactions. Such an event of a supernova explosion provides the motivation of extending Fermi's firstly proposed acceleration mechanism.

In this section, the basic calculation steps will be presented following Gaisser's approach [31]. The sketch in figure 2.4 demonstrates how the particle is scattered off of the magnetic fields close to the shock plane.

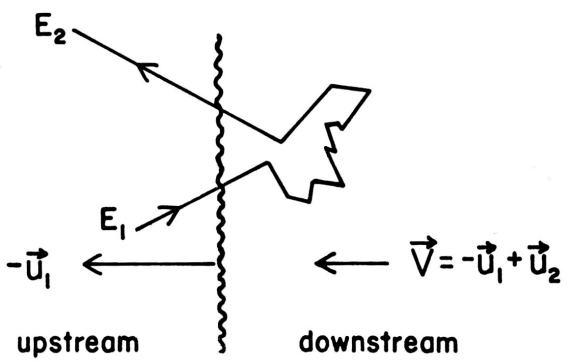

Figure 2.4: *Sketch of a cosmic ray particle hitting the shock front of a moving cloud. Figure taken from [31].*

For reasons of simplicity a plane shock front will be considered, moving with the velocity $-u_1$ while the shocked gas is slower than the shock front and moves with the velocity u_2. The relation $|u_2| < |u_1|$ can thus be applied. In the laboratory frame the shocked gas moves in Fig. 2.4 to the left with $V = -u_1 + u_2$. With the already known use of $\beta = V/c$ equation (2.2.11) defines the relation between the velocity of the gas after the shock to the gas before the shock. The two regions are called *downstream* and *upstream*, respectively [31].

The calculation of the angular averages makes the difference in calculating the fraction of additional energy per shock event.

In the case of a plane shock front the angular average is

$$\frac{\mathrm{d}n}{\mathrm{d}\cos\theta_2'} = 2\cos\theta_2' \qquad \text{for } 0 \leq \cos\theta_2' \leq 1. \tag{2.2.18}$$

A negative value is not allowed because particles can only leave the shock via the upstream region. This restricts the average to $\langle\cos\theta_2'\rangle = 2/3$, and the fractional energy gain yields

$$\frac{\langle\Delta E\rangle_2}{E_1} = \frac{1 - \beta\cos\theta_1 + \frac{2}{3}\beta - \frac{2}{3}\beta^2\cos\theta_1}{1-\beta^2} - 1. \tag{2.2.19}$$

The incoming particle distribution requires particles to enter the shock from the right, see Fig. 2.4. No positive cosine values are accepted in this case and thus $\langle\cos\theta_2'\rangle = -2/3$. The energy gain can now be determined and is

$$\xi = \frac{\langle\Delta E\rangle_{1,2}}{E_1} = \frac{1 + \frac{4}{3}\beta + \frac{4}{9}\beta^2}{1-\beta^2} - 1. \tag{2.2.20}$$

In the case of a non-relativistic shock the above equation simplifies to

$$\xi \approx \frac{4}{3}\beta = \frac{4}{3}\frac{u_1 - u_2}{c}. \tag{2.2.21}$$

The spectral index requires information about the escape probability, which physically is the ratio of particles suffering the shock and those in the downstream region. The first rate is obtained by folding the flux with the plane shock and integrating this result for particles traveling towards the shock

$$\int_0^1 \int_0^{2\pi} \mathrm{d}\cos\theta \; \mathrm{d}\phi \; \frac{c\varrho_{\mathrm{CR}}}{4\pi} = \frac{c\varrho_{\mathrm{CR}}}{4}. \tag{2.2.22}$$

The escape probability is given by

$$P_{\mathrm{esc}} = 4\,\frac{\varrho_{\mathrm{CR}}\;u_2}{c\;\varrho_{\mathrm{CR}}} = 4\frac{u_2}{c}. \tag{2.2.23}$$

Thus, the spectral index, is obtained by

$$\alpha = \frac{P_{\text{esc}}}{\xi} \approx \frac{3}{u_1/u_2 - 1}. \tag{2.2.24}$$

The above equations lead to the desired spectrum with a realistic spectral index

$$\frac{\mathrm{d}N(E)}{\mathrm{d}E} \sim E^{-2}. \tag{2.2.25}$$

In contrast to Eq. 2.2.17 the spectral index for the first order Fermi acceleration is independent from the absolute velocity value of the cloud. It only depends on the ratio of up- and downstream velocities.

2.3 Stellar evolution and supernova explosion

In this section, the evolution of stars is briefly outlined and the main processes are described. The focus is put on those stars that eventually explode at the end of their evolution in a supernova. Reviews on this topic can be found in e.g. [33, 34]

The birth of a star occurs due to the contraction of a gas cloud. The gas is bound by gravitation and the cloud starts heating up due to the increased pressure. In the Hertzsprung-Russell diagram, the luminosity is plotted versus the surface temperature of stars, see Fig. 2.5. A new-born star can typically be found in the bottom-right corner in the diagram due to the comparably low temperature and luminosity. Depending on its mass, the future evolution of a star can be predicted. A main sequence star will initiate the proton-proton cycle, i.e. the fusion chain of protons to helium. For details about the helium production, see [33].

When approximately 10% of the hydrogen in a star has been fused to helium, the star leaves the main sequence. The total energy of a star is proportional to its mass, however, the rate at which nuclei fuse to heavier elements depends more heavily on its mass, see e.g. [33]. It has been found that the time that stars spend in the regime of the main sequence is proportional to M^{-3}, where M is the mass of the star. Hence, low mass stars can be found for much longer in the main sequence.

For stars with initial masses less than approximately 1.5 $M_\odot$, with $M_\odot$ as the so-

lar mass, the star will eventually become a white dwarf. The helium core in the center of the star grows as long as the hydrogen fuses. For other nuclear fusions the temperature is not sufficiently high, and thus it contracts to a low luminosity object. The surface temperature of a white dwarf is about 10,000 K and its radius is approximately 3,000 km [33].

Massive stars with masses $M \geq 8M_\odot$ take a completely different path. Nuclear fusions can continue beyond helium, because the helium core reaches temperatures greater than 10^8 Kelvin. These reactions occur in shells surrounding the core, and the temperature is so high that helium ions fuse to carbon and even oxygen. Once the helium reservoir is exhausted, the density increases due to the gravitational potential, which in turn leads to even higher temperatures.
Further steps in the reaction chain result in neon, magnesium, silicon, and even heavier elements. The higher the atomic number, the faster the reaction takes place. While heavier elements are generated, the star proceeds toward the red giant bubble in the HR-diagram, Fig. 2.5. The occurance of super giants (top right corner in Fig. 2.5) and rare blue giants (top left corner in Fig. 2.5) can be explained by details during the evolution.
When the core of the giant has accumulated heavy ions and the temperature has risen to 10^9 Kelvin, neutrinos produced. One part results from the reaction $p + e^- = n + \nu_e$, referred to as *neutronization*. The other process creating neutrinos results from stellar photons producing electron and positron pairs via pair production, which in turn annihilated into two photons in earlier stages. However, the increasing temperature eventually favors the channel of electron and positron interactions producing neutrinos and antineutrinos, instead of photons. Despite the small neutrino cross section, high densities of $\gtrsim 10^{14}$ kg/m^3 [34] cause scattering and absorption of neutrinos before escaping the star and carrying away the energy that has been transmitted to them. The radiation pressure counteracts the gravitation potential but this hydrostatic equilibrium cannot be maintained any longer. Neutrino emission is the major factor for energy loss of stars in these final stages.

When the temperature is around $3 \cdot 10^9$ Kelvin the heavy elements begin to fuse until the core is enriched with iron. Further nucleosynthesis would consume energy because the binding energy per nucleon is the highest for iron. When the core's

mass exceeds the Chandrasekhar limit, $M_{Ch} = 1.4M_{\odot}$, even the pressure caused by electrons due to Pauli's exclusion principle cannot prevent a further contraction. The disintegration of elements consume energy and therefore the temperature decreases. Electrons interact with the protons, $p + e^- \rightarrow n + \nu_e$, and the loss of leptons decreases the pressure.

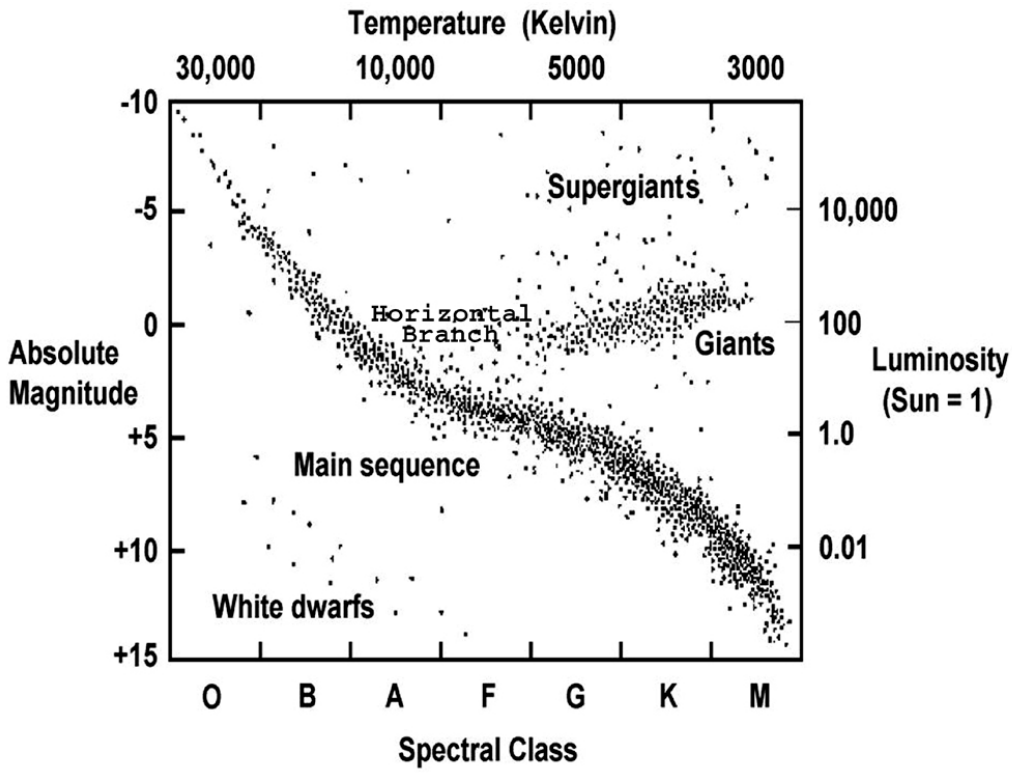

Figure 2.5: *The Hertzsprung-Russell diagram shows the evolution of a star. Starting from the bottom-right corner, a star moves along the main sequence until it has reached the end of its lifetime. The initial mass decides about whether the star turns into a white dwarf or continues as a giant and eventually explode in a supernova event. Figure taken from [35].*

The pressure inside the core, however, stays almost constant because of gravitation, and eventually the core collapses. Within seconds, the core's radius decreases by more than 90% of it's original size [33]. The core collapse causes a density that is greater than the nuclear density, i.e. the density becomes greater than 10^{14} g/cm^3 [33].

The inner core, however, bounces back, because a further collapse is impossible. The outer part that is still falling toward the gravitational center is met by the reflected masses and a shock front moving outward is created. The shock propagates through the entire core, which holds 10^{51} ergs of energy. The outer shells are heated and ejected with high velocity [33]. This matter expands into space, known as a supernova explosion.

Supernovae are usually classified by two types, namely type I and type II. The difference of both types appears in the absorption lines. Type I supernovae do not contain hydrogen lines, while type II supernovae do.

Figure 2.6 shows an X-ray image of the supernova remnant Puppis A. The estimated age ranges between 3,700 years [36] and 4,450 years [37]. The distance to Earth has been calculated to be 2.2 kpc based on HI and CO absorption lines [38], although the analysis of the 1667-MHz ground state hydroxyl (OH) indicates a distance of approximately 1.3 kpc [39]. The spectral energy distribution (SED) shows the processes contributing to the spectrum, see Fig. 2.7. The low energy bump is solely caused by synchrotron radiation, while the higher energetic component represents the composition of the π^0-decay, bremsstrahlung, and Inverse Compton scattering, see e.g. [40, 41].

The estimation of the total cosmic ray budget released in an explosion can be used to calculate the contribution of SNRs to the cosmic ray flux. Approximately, $E_{\mathrm{SN}} = 10^{51}$ erg are released, and the total cosmic ray luminosity for $E_{\mathrm{CR}} < 10^{15}$ eV within uncertainties yields $L_{\mathrm{SN}} \approx 2 \times 10^{41}$ erg $\cdot$ s^{-1}, see e.g. [42]. By further assuming that a constant rate of $\eta = 10\%$ of the total energy converts to hadronic cosmic rays, this can already explain the total cosmic ray energy budget. The luminosity is then obtained, see e.g. [43]

$$L_{CR} \approx 2 \times 10^{41} \left(\frac{\eta}{0.1}\right) \left(\frac{\nu_{\mathrm{SNR}}}{0.02\,\mathrm{yr}^{-1}}\right) \left(\frac{E_{\mathrm{SN}}}{10^{51}\,\mathrm{erg}}\right). \tag{2.3.1}$$

This simple calculation demonstrates that SNRs are capable of providing the measured flux up to $E_{\mathrm{CR}} \approx 10^{15}$ eV by making only a few reasonable assumptions.

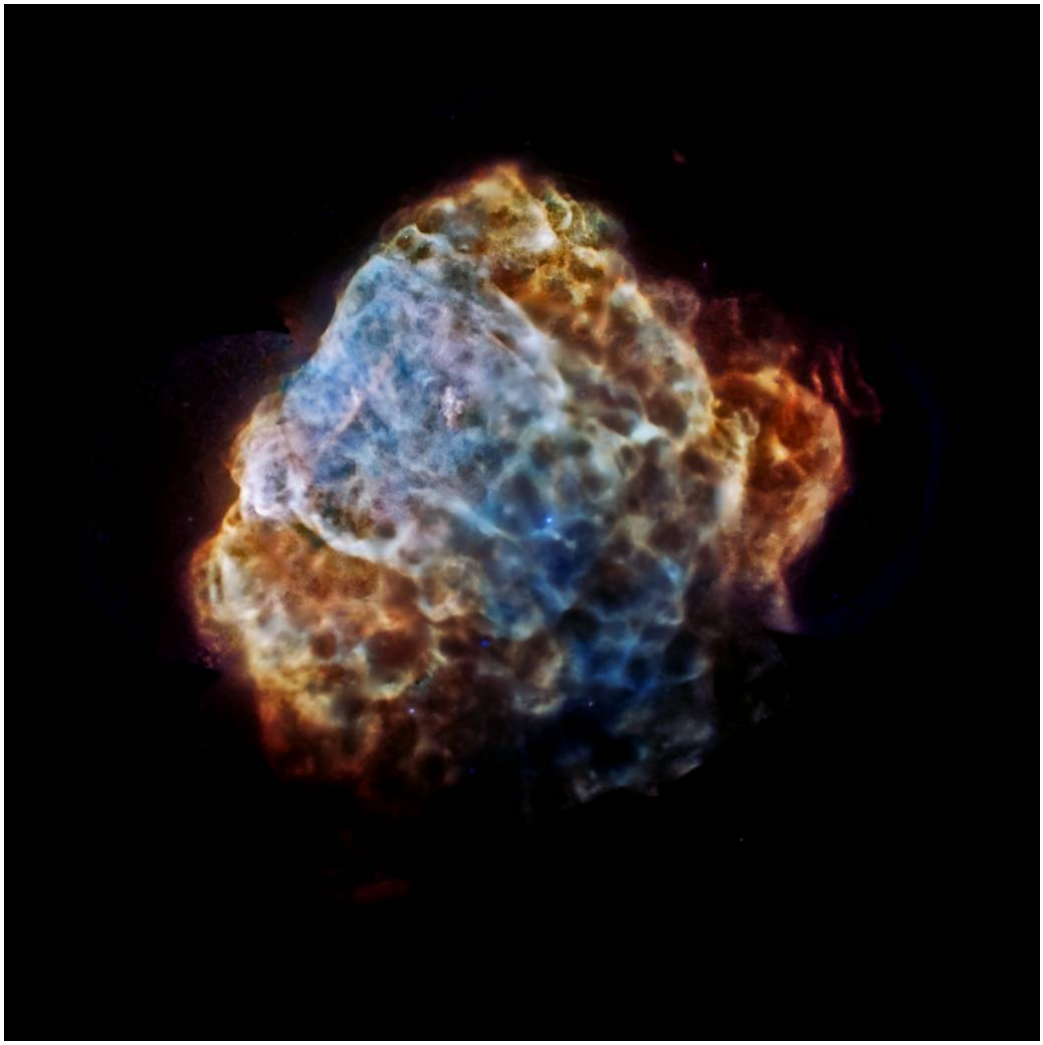

Figure 2.6: *The supernova remnant Puppis A exposed in X-ray light with data combined from NASA's Chandra X-Ray Observatory and ESA's XMM-Newton. Low-energy X-rays are indicated by red color, and high-energy X-rays are shown in blue, while green indicates an intermediate energy. Source taken from [44].*

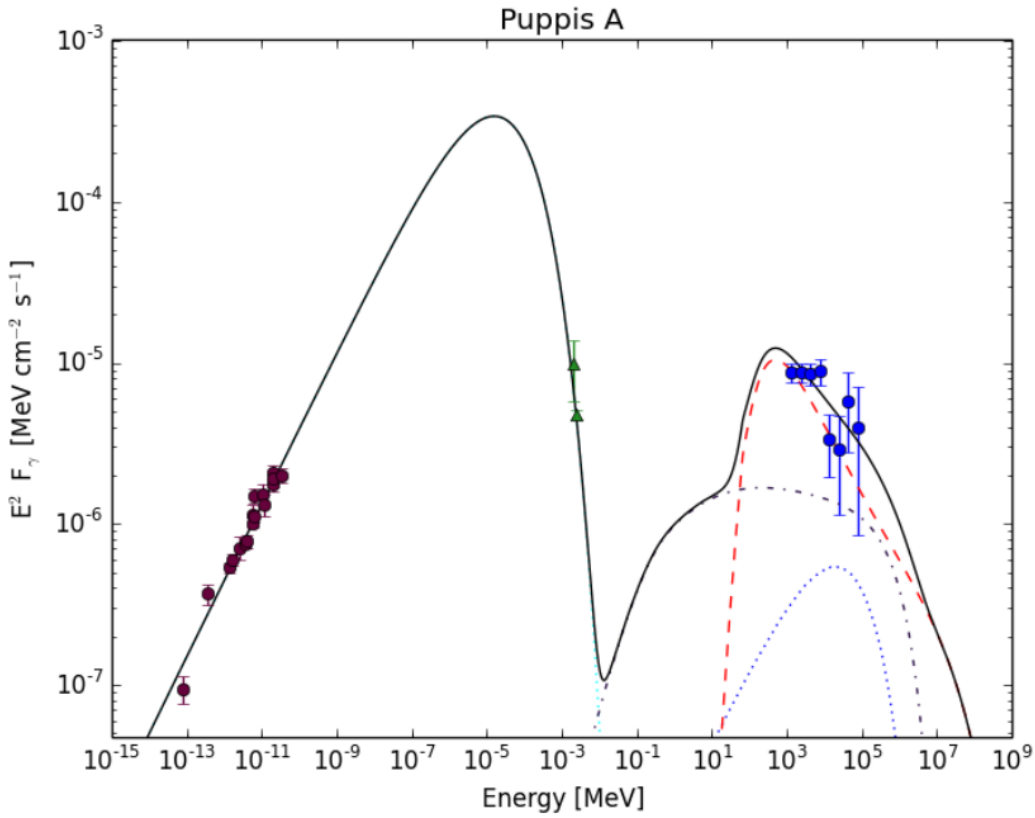

Figure 2.7: *The blue data points are Fermi data, ROSAT data are shown as green triangles, and data in the radio energy regime is indicated by purple bullets. The red dashed line indicates the contribution through π^0-decay photons, the black dotted-dashed line represents the bremsstrahlung component, and the blue dotted line corresponds to the Inverse Compton scattering. Figure taken from [40].*

2.4 Propagation of cosmic rays

In this section, an overview of simulation techniques for cosmic ray propagation is given. Two fundamentally different approaches, namely the single- and multi particle approach, define the state-of-the-art propagation techniques. Advantages and disadvantages of each concept are reviewed and respective software is presented.

2.4.1 Single particle propagation

One advantage of simulating single particles is that the propagation path can be followed. External fields, such as the electromagnetic fields influence the trajectory of charged particles. In the Galaxy, cosmic rays are deflected by these fields, in particular when the particle's energy is low because the gyroradius is proportional to the energy. Stellar objects can provide a strong magnetic field, but also by the galactic magnetic field. In general, the equation of motion is solved numerically.

This approach is implemented in the CRPropa 3.0 code, which is designed for extragalactic propagation [45]. In this version of the code, particle energies below 10 PeV consume so much computing capacities such that galactic cosmic ray propagation is not applicable. The CRPropa framework is publicly available for usage and proposals for extensions can be made. Recently updated to version CRPropa 3.1 [46], it is now possible to simulate single particles with energies as low as hundreds of PeV up to ZeV. Energies of a few TeV can be simulated, as well, but here, stochastic differential equations are used within the multi particle approach, see the following subsection.

The deflection and resulting trajectory can be calculated by solving a coupled system of differential equations in cgs units is

$$\frac{\mathrm{d}\vec{p}}{\mathrm{d}t} = q\left(\vec{E} + \frac{\vec{u}\times\vec{B}}{c}\right), \quad \text{and} \tag{2.4.1}$$

$$\frac{\mathrm{d}\vec{x}}{\mathrm{d}t} = \vec{u}. \tag{2.4.2}$$

In the above equations, $\vec{p} = m\gamma\vec{u}$ is the relativistic momentum of a particle, the parameter q stands for the electric charge, $\vec{u}$ for the particle's velocity and $\vec{E}(\vec{x},t)$ and $\vec{B}(\vec{x},t)$ denote the electric and magnetic field strength, respectively. By integrating the equation of motion, i.e. Eq. (2.4.1), the path of the particle is obtained.

In Chapter 6, the equation of motion is numerically integrated following the implementation of [47] and using the Runge-Kutta integration method, see subsection 2.4.4 for details.

2.4.2 Multi particle propagation

The purpose of propagating multi particles is to understand the global picture, i.e. the slope of the cosmic ray spectrum measured on Earth, rather than tracing one individual particle and understanding all its interactions. Here, a diffusion tensor is introduced in order to describe the diffusion of particles. Models for diffusion include the *leaky box model*, see e.g. [31], or even more complex ones, such as in [48–50].

When particles are ejected from a source, their initial energy spectrum is altered through processes of advection, adiabatic cooling, and diffusion in space and momentum. The equation that accounts for these processes is the Parker transport equation, see e.g. [46]

$$\frac{\partial n}{\partial t} = \nabla \cdot (\hat{\kappa} \nabla n) - \vec{u} \cdot \nabla n + \frac{1}{p^2} \frac{\partial}{\partial p} \left(p^2 \kappa_{pp} \frac{\partial n}{\partial p} \right) + \frac{1}{3} (\nabla \vec{u}) \frac{\partial n}{\partial \ln p} + S(\vec{x}, p, t), \tag{2.4.3}$$

with n as the particle density, $\vec{u}$ as the advection speed, $\hat{\kappa}$ as the spatial diffusion tensor, the absolute momentum is denoted by the parameter p, κ_{pp} stands for re-acceleration, and $S(\vec{x}, p, t)$ is the source distribution.
This equation defines the basis for the simulation codes GALPROP [51], DRAGON [52], and PICARD [53].
GALPROP is a program that allows a user-defined source distribution. Boundary conditions for the propagated particles can also be defined, such as convection (galactic wind), diffusive re-acceleration, energy loss processes, and nuclear fragmentation. Further, radioactive decays and the production of secondary particles are also included [51].
The DRAGON code is based on the propagation routine used in GALPROP, however, it is able to include further transport parameters, such as anisotropic spatial diffusion [52].
In PICARD, a steady state solution can be computed for the propagation. No adjustments of numerical parameters need to be made prior to the simulation. Multi-grids are used for the integration and it is also claimed to be significantly faster that GALPROP [53], allowing a finer resolution of the Galaxy.

2.4.3 Crank-Nicholson method

The Crank-Nicholson approach for numerically solving partial differential equations follows the finite difference approach. It can be organized in a Runge-Kutta algorithm. The applicable differential equation[1] has the shape of a diffusion equation

$$\frac{\partial \psi}{\partial t} = F\left(\psi, x, t, \frac{\partial \psi}{\partial x}, \frac{\partial^2 \psi}{\partial x^2}\right). \tag{2.4.4}$$

In the following, the notation $\psi_i^n = \psi(i\Delta x, n\Delta t)$ will be used. By averaging the methods of forward Euler at n, and backward Euler at $n+1$ [55]

$$\frac{\psi_i^{n+1} - \psi_i^n}{\Delta t} = F^n\left(\psi, x, t, \frac{\partial \psi}{\partial x}, \frac{\partial^2 \psi}{\partial x^2}\right) \qquad \text{(forward)} \tag{2.4.5}$$

$$\frac{\psi_i^{n+1} - \psi_i^n}{\Delta t} = F^{n+1}\left(\psi, x, t, \frac{\partial \psi}{\partial x}, \frac{\partial^2 \psi}{\partial x^2}\right) \qquad \text{(backward)}, \tag{2.4.6}$$

the result of the Crank-Nicholson method is [55]

$$\frac{\psi_i^{n+1} - \psi_i^n}{\Delta t} = \frac{1}{2}\left[F^n\left(\psi, x, t, \frac{\partial \psi}{\partial x}, \frac{\partial^2 \psi}{\partial x^2}\right) + F^{n+1}\left(\psi, x, t, \frac{\partial \psi}{\partial x}, \frac{\partial^2 \psi}{\partial x^2}\right)\right]. \tag{2.4.7}$$

This equation can be used to solve the transport equation (5.1.1) for steps in time. With coefficients α_k the solution yields [54]

$$\begin{aligned}\frac{\psi_i^{t'+1} - \psi_i^t}{\Delta t} &= \frac{\alpha_1 \psi_{i-1}^{t'} - \alpha_2 \psi_i^{t'} + \alpha_3 \psi_{i+1}^{t'}}{2\Delta t} \\ &\quad + \frac{\alpha_1 \psi_{i-1}^{t} - \alpha_2 \psi_i^{t} + \alpha_3 \psi_{i+1}^{t}}{2\Delta t} + q_i.\end{aligned} \tag{2.4.8}$$

[1] For simplicity reasons, the case of one dimension is presented. Higher dimensions require a generalization. In GALPROP, a numerical approximation is used, which, at small times scales, has been proved to solve the equation still at a high accuracy. See [54] for discussion and further details.

In equation (2.4.8), the notation $t' = t + \Delta t$ applies. The next step is obtained through

$$\begin{aligned}\psi_i^{t'} &= \psi_i^t + \frac{\alpha_1}{2}\psi_{i-1}^{t'} - \frac{\alpha_2}{2}\psi_i^{t'} + \frac{\alpha_3}{2}\psi_{i+1}^{t'} \\ &+ \frac{\alpha_1}{2}\psi_{i-1}^{t} - \frac{\alpha_2}{2}\psi_i^{t} + \frac{\alpha_3}{2}\psi_{i+1}^{t} + q_i\Delta t. \end{aligned} \tag{2.4.9}$$

This method makes use of both implicit and explicit terms. It is stable for all α and Δt. Starting with a large Δt, it will be iterated until a the solution is stable. For $\alpha \ll 1$ the solution is accurate, while for all other cells it is stable but not accurate. Then, Δt will be reduced by half until $\alpha \ll 1$ for all cells. The solution is then accurate and stable in all cells. Further details on the exact implementation in GALPROP can be found in [54].

2.4.4 The Runge-Kutta algorithm

A useful method to integrate differential equations numerically is the Runge-Kutta algorithm, which can be used with an adaptive step control. The method is generally used for differential equations of the form

$$\frac{\mathrm{d}y}{\mathrm{d}t} = f(t, y), \qquad \text{with the initial condition} \tag{2.4.10}$$

$$y(t_0) = y_0. \tag{2.4.11}$$

The next step is calculated by

$$y_{n+1} = y_n + \frac{1}{6}(K_1 + 2K_2 + 2K_3 + K_4) \approx y(t_{n+1}). \tag{2.4.12}$$

The coefficients in Eq. (2.4.12) are defined in the following manner

$$K_1 = \delta t \cdot f\left(t_n, y_n\right) \tag{2.4.13}$$

$$K_2 = \delta t \cdot f\left(t_n + \frac{\delta t}{2}, y_n + \frac{K_1}{2}\right) \tag{2.4.14}$$

$$K_3 = \delta t \cdot f\left(t_n + \frac{\delta t}{2}, y_n + \frac{K_2}{2}\right) \tag{2.4.15}$$

$$K_4 = \delta t \cdot f\left(t_n + \delta t, y_n + K_3\right). \tag{2.4.16}$$

An implemented adaptive step control can ensure that the value of the parameter δt is chosen in such a way that the particle's momentum and position are within a pre-defined tolerance. Such feature is provided by the open accessible GSL library (GNU Scientific Library) [56].

CHAPTER 3

Detectors in Astroparticle Physics

In astroparticle physics, a sound knowledge of the cosmic ray spectrum is essential in order to understand the acceleration processes and interactions in the sources themselves. With the first discovery in the 1910's the scientific society has been introduced to a completely new field of particle physics. Shortly thereafter, new kinds of detection methods were developed. When cosmic rays reach Earth, they enter the atmosphere and due to their cross section and their likeliness to interact with atmospheric molecules, no primary particle is able to reach the ground. This is the reason why most instruments have to make use of an indirect detection method by registering secondary particles. Space-based detectors, for example satellites with a detection chamber or balloon experiments, can even apply a direct detection method.

This section will concentrate on the various detection methods by describing those detectors whose results are most crucial for this thesis. With respect to the course of this thesis, both the ground-based Tibet array and the new generation neutrino experiment IceCube will be described, and a limited selection of their achievements will be presented. These two experiments have measured the Sun shadow, which will be highlighted from a different perspective later in this paper. As an example for a space-based detector, a description of the AMS-02 detector closes this chapter.

3.1 Gamma-rays and their detection

The signature of gamma-rays is ambiguous. The leptonic processes bremsstrahlung and Inverse Compton may contribute to the signal that is expected to come from a π^0 decay, see e.g. [57,58], which produces astrophysical gamma-rays, see Eq. (3.2.5).

There are two features that indicate a π^0 decay. First, the cutoff in the gamma-ray spectrum at about $E_{\text{cutoff,HE}} \geq 100$ TeV occurs at such high energies that leptonic processes can basically be excluded, see e.g. [59]. By assuming that 10% of the primary energy transfers into photons, the original proton has been accelerated to $E_{\text{p}} = 1$ PeV. Experimental data provided by HAWC and CTA will soon allow a search of those sources accelerating cosmic rays to such high energies.
The second aspect refers to the low-energy cutoff. It is apparent at $E_{\text{cutoff,LE}} \approx 70$ MeV and reflects the minimum energy of a gamma-ray from a π^0 decay at rest, see equation (3.2.5).
With data from the Fermi satellite, such a cutoff could be confirmed for the three supernova remnants W44, IC443, and W51C, see [60–62]. These three remnants provide the first evidence of SNRs actually accelerating cosmic rays and have a very steep spectrum[1] with an energy cutoff in the TeV regime. Due to the steepening of the cosmic ray spectrum by diffusion in the Galaxy of about $E^{-0.3} - E^{-0.5}$, it is important that the average spectral index at the source is around $E^{-2.2} - E^{-2.4}$, see e.g. [40].

Approximately 30 SNR objects with a gamma-ray spectrum have been identified with imaging air Cherenkov telescopes at TeV energies [63]. In some cases, the high-energy cutoff cannot be found, but the spectrum in gamma-rays is known up to $E_{\gamma,\text{max}} \approx 10$ TeV, corresponding to $E_{\text{p,max}} \gtrsim 100$ TeV primary energy.

In light of these findings, the spectra obtained suggest that SNRs are possible candidates for the acceleration of cosmic rays, and thus contribute to the cosmic ray spectrum. In the following, the Tibet AS-Gamma experiment is presented as an example of gamma-ray detection.

[1] $\alpha_{\text{W44}} = 2.6, \alpha_{\text{IC443}} = 2.7, \alpha_{\text{W51C}} = 2.4$, see Chapter 5 for details.

3.1.1 Tibet AS-Gamma Experiment

The Tibet Air Shower Array is located at Yangbajing in Tibet, China, at an altitude of 4,300m above sea level [64]. It consists of scintillation detectors arranged in an octet symmetry with a varying distance to one another. In its center the distance is equal, whereas closer to the outer edges, the distance becomes longer. The conceptual sketch is shown in Fig. 3.1.

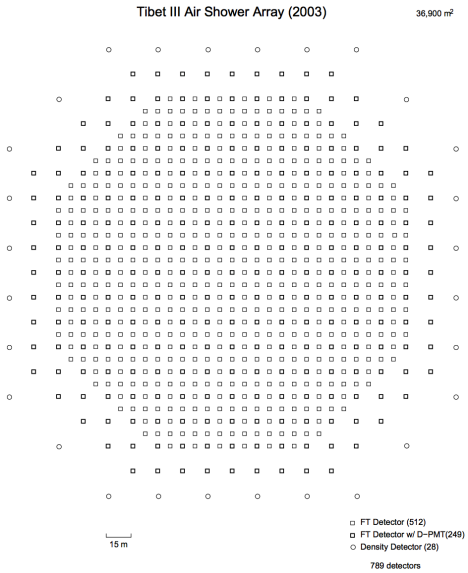

(a) Sketch of the geometrical arrangement of the scintillator detection tanks of the Tibet AS-Gamma array. Figure taken from [65].

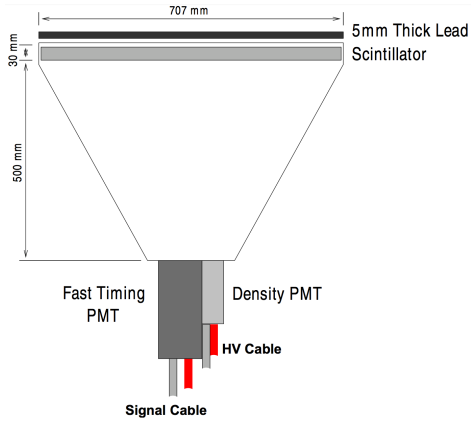

(b) Sketch of one scintillator detector as used by the Tibet experiment. Figure taken from [65].

Figure 3.1: *Figure presents the basic experimental construction of the Tibet AS-Gamma array. In* ***(a)****, a heads-on overview of the arrangement of the detector array is given. The sketch in* ***(b)*** *shows the individual detector construction and its functionality.*

The experiment underwent a continuous expansion of the detector array in size. The first stage of this detector, referred to as the Tibet-I surface, was finished in the year 1990 and consisted of 65 plastic scintillation detectors. Today's configuration comprises 761 improved scintillation tanks [65], see Fig. 3.1b.

3.2 Neutrinos

The existence of astrophysical neutrinos proves hadronic interactions, which makes them valuable transmitters. Their detection is highly desirable but also a great challenge [66]. The proof of their existence has recently been presented by the IceCube collaboration [67, 68]. Neutrino production can occur in astrophysical shocks when a proton interacts with a photon or another proton. In both cases, pions are produced that subsequently decay into neutrinos. The main interaction channels are [8, 69]

$$p\,\gamma \rightarrow \Delta^+ \rightarrow \begin{cases} p\,\pi^0 & \text{, ratio } 2/3 \\ n\,\pi^+ & \text{, ratio } 1/3 \end{cases} \tag{3.2.1}$$

$$p\,p \rightarrow \begin{cases} p\,p\,\pi^0 & \text{, ratio } 2/3 \\ p\,n\,\pi^+ & \text{, ratio } 1/3. \end{cases} \tag{3.2.2}$$

Negatively charged pions are produced by neutrons interacting with a gamma particle or a proton, see equations above. Kaons become more important when the energy is high. The lifetime of pions[2] suggest that they decay before they are able to interact with other particles. In the decay chain of charged pions neutrinos are produced, while neutral pions decay mainly into two gamma quanta [8, 69]

$$\pi^+ \rightarrow \mu^+\,\nu_\mu \rightarrow e^+\,\nu_e\,\bar{\nu}_\mu\,\nu_\mu, \tag{3.2.3}$$

$$\pi^- \rightarrow \mu^-\,\bar{\nu}_\mu \rightarrow e^-\,\bar{\nu}_e\,\nu_\mu\,\bar{\nu}_\mu, \tag{3.2.4}$$

$$\pi^0 \rightarrow 2\,\gamma. \tag{3.2.5}$$

When charged pion decays occur at the same rate, the flavor ratio yields [8]

$$(\nu_e\ :\ \nu_\mu\ :\ \nu_\tau) = (\bar{\nu}_e\ :\ \bar{\nu}_\mu\ :\ \bar{\nu}_\tau) = (1\ :\ 2\ :\ 0). \tag{3.2.6}$$

Neutrinos oscillate in their flavor because of a phase difference between mass eigenvalues when they propagate. Therefore, the flavor ratio expected on Earth is [8]

[2] Lifetime of π^0 [69]: $\tau_{\pi^0} = (8.52 \pm 0.18) \cdot 10^{-17}$ s
Lifetime of $\pi^\pm$ [69]: $\tau_{\pi^\pm} = (2.6033 \pm 0.0005) \cdot 10^{-8}$ s

$$(\nu_e \ : \ \nu_\mu \ : \ \nu_\tau) = (\bar{\nu}_e \ : \ \bar{\nu}_\mu \ : \ \bar{\nu}_\tau) = (1 \ : \ 1 \ : \ 1). \tag{3.2.7}$$

The condition for a successful oscillation and an equal distribution of all flavors is that the path length is greater than the size of the solar system, roughly speaking.

The the transmitted amount of energy in proton interactions to neutrinos is proportional and is $E_\nu = E_p/20$ [70]. Therefore, a neutrino with $E_\nu \approx 2$ PeV neutrino results from a cosmic ray with $E_{\mathrm{CR}} \approx 40$ PeV primary energy. By investigating data already obtained from the full IceCube detector, a total number of 54 such neutrino events have been found within 3 years, with at a background of $\sim 4-6$ atmospheric neutrinos per year. Other analyses confirm these results [71,72]. From these few events, it is not yet possible to present a sound point-source study, but rather they represent a diffuse flux from a region containing several sources. Other claims admit only $2-4$ events per year or less from galactic sources [40]. With a longer time of active data collection by the IceCube detector and its successor IceCube-Gen2, as well as KM3NeT, an increase of astrophysical neutrino data can be expected, which will increase statistics and pointing information. It is hoped that neutrino astrophysics will have a major impact on the study of flux from Galactic and extragalactic sources, i.e. the energy range between the *knee* and the *ankle*.

3.3 The IceCube Neutrino Observatory

The IceCube Neutrino Observatory is located at the geographic South Pole. It consists of 5,160 Digital Optical Modules, so-called DOMs, which are attached to 86 strings [73]. The vertical spacing of the DOMs is 17 m to and the horizontal spacing of the strings is 105 m, see [73]. This setup spans a total volume of approximately one cubic kilometer. Figure 3.2 shows a detailed sketch of the detector.

The depth in which IceCube is situated allows the detection of neutrinos, because the ice is under such high pressure and so pure that there are virtually no interferences with other substances. The ice therefore transmits light, mainly evoked by Cherenkov radiation.
The absorption of secondary particles in the upper atmosphere or the ground re-

sults in lower background noise, which promotes the advantage of this location even more. However, the trigger rate is dominated by atmospheric muons with a rate of 3000 s^{-1}, see [74]. The ratio of atmospheric muons to atmospheric neutrinos is roughly 10^{11}:10^5, see e.g. [8, 75].

After researching the functionality of such a detection technique, for example its location and other operational issues, IceCube reached its full configuration in December 2010. Since then, it has collected data continuously. The fact that neutrinos only interact via the weak force allows them to pass through the Earth from all directions, even from the North Pole [76]. Therefore, the detector is active at all times. The detection of neutrinos, however, is very difficult and requires high sensitivities and a massive detection medium. Due to the fact that atmospheric muons dominate IceCube's trigger rate, sophisticated analyses are required to isolate neutrino events, see [76] for further details. The underlying processes of neutrino interaction are described in the following subsections.

Neutrinos of energies in the PeV range can be detected in the upper limit of the sensitivity. Thus, the detector makes the highest energetic events accessible for particle investigations and allows the study of astrophysical sources such as supernova explosions, gamma-ray bursts, or neutrinos emerging from black holes or neutron stars, see e.g. [8].
An extension to the detecting architecture is realized by strings with DOMs attached, but with lesser distance compared to the usual arrangement. Lower energetic events can thus be registered. This region is called DeepCore, and the focus is very diverse, as its data can be used to conduct a variety of studies, for example dark matter searches or the basic neutrino properties, see [77]. DeepCore detects with an energy range of 10 GeV $\leq E_\nu \leq$ 100 GeV [78], while IceCube measures higher energies.

The IceTop array consists of 81 stations that are equipped with two particle detectors each [79]. The lower energy threshold is between $100 - 300$ TeV. Their goal is to reveal the induced air showers by high energy particles that interact with the upper atmosphere molecules. Further, cosmic ray composition and anisotropy studies are the principal goal of IceTop, see e.g. [80–84].

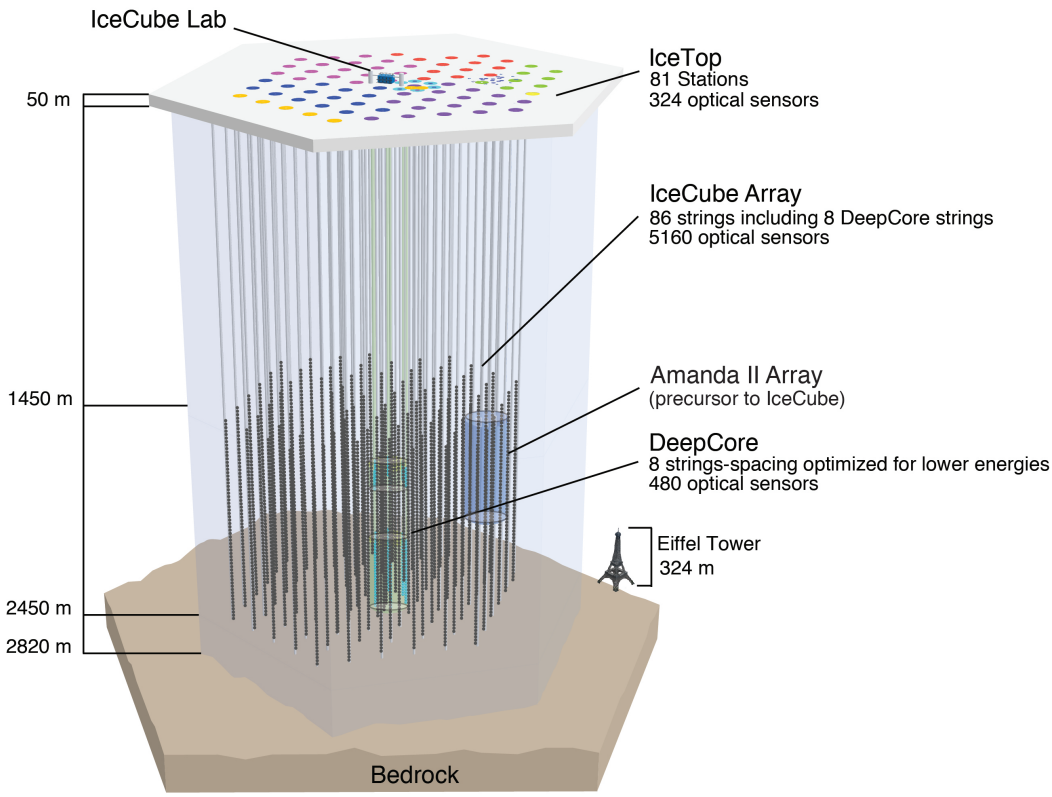

Figure 3.2: *Figure shows a detailed sketch of how the IceCube neutrino detector is designed. Located at the South Pole, the detector elements are situated approximately 1.5 km below the surface. IceTop is an additional array focusing on cosmic ray detection, while DeepCore measures low energy neutrino events by an increased density of the measuring instruments. IceCube's predecessor AMANDA is also shown. Figure taken from [85].*

3.3.1 Cherenkov radiation

In a dielectric medium, for example in ice, high energetic charged particles can exceed the local speed of light. With the particles velocity v and the refractive index n, the condition

$$v > \frac{c}{n} \tag{3.3.1}$$

must be fulfilled in order to produce a light cone. This effect and the emitted radiation is known as Cherenkov radiation. For ice, the refractive index is $n_{\text{ice}} = 1.3$, meaning a particle velocity of $v = 0.75c$ is sufficient enough to evoke this effect. The opening angle ϑ is determined by

$$\cos(\vartheta) = \frac{c}{nv}. \tag{3.3.2}$$

IceCube and many other experiments make use of this effect and successfully investigate cosmic rays and neutrinos. Cherenkov light can be detected not only by astrophysical observatories but also by accelerator experiments, making it a desirable tool for many high energy physics investigations.

3.3.2 Neutrino detection with IceCube

In order to detect neutrinos, a detection medium is required, which is the main reason why IceCube operates far below the surface where the ice is dense. The interaction probability is hereby increased. Two channels exist through which neutrinos can interact: the neutral (NC) and the charged current (CC)

$$\nu_\ell + N \rightarrow \ell + X \qquad \text{(charged current)} \tag{3.3.3}$$

$$\nu_\ell + N \rightarrow \nu_\ell + N \qquad \text{(neutral current).} \tag{3.3.4}$$

According to the standard model of particles, the neutrino can be of three flavors, namely the electron, muon, and tau flavor, denoted by ν_e, ν_μ, and ν_τ, see e.g. [86]. The equations above represent interaction through the weak force. Mediator particles are the $W^\pm$ bosons and the Z_0 boson for the charged and the neutral current.

In the case of the charged current a lepton of the same flavor will be produced, resulting in a distinctive signature. For example, an electron neutrino interacts with a nucleon producing an electron and a hadronic cascade. In the case of muon neutrino interactions, the produced muon evokes a track-like Cherenkov signature in the detectors. These muons travel along distances that are typically much larger than the detector dimensions, only losing part of their energy via processes, such as Cherenkov radiation, bremsstrahlung, and photo-nuclear interactions, before finally decaying. The tau flavor is very rare due to its high mass and has not yet been observed with IceCube. It would create a *double bang*, meaning two cascades. The first hadronic cascade is produced in the charged current interaction of a tau neutrino with a nucleon. The second cascade results from the decay of the tau. Such an event has not yet been detected, but the geometrical size of the detector plays an important role, because the second cascade could have had occurred outside of the detector and hence was not seen in the data. The neutral current induces a hadronic cascade, as well, and parts of the neutrino's energy are transmitted to the nucleon.

3.3.3 High energy neutrinos detected with IceCube

From 2010 through 2014, with a total lifetime of 1347 days, IceCube discovered 54 neutrino events with an energy greater than 60 TeV. The map in Figure 3.3 shows the sky in galactic coordinates and records 54 so-called High Energy Starting Events (HESE) [87]. Veto regions, which are the boundaries of the detector are used to separate muons from neutrino events. If a Cherenkov signature is detected within these regions, the event is excluded from the HESE sample.
Their origin, however, cannot solely be identified with galactic objects, and a study that searches for clustering is not yet at a stage with sufficiently significant statistics. The analysis of the energetically highest neutrino events reported an up-going muon with an energy of $E_\mu = 2.6 \pm 0.3$ PeV [88].
The authors of [87] present a search for high-energy events that have been detected by IceCube. Further, they have discovered an astrophysical neutrino flux that exceeds the atmospheric background. In Fig. 3.4, the registered events in a period of 1,347 days from the years 2010 through 2014 are shown as a function of deposited energy.

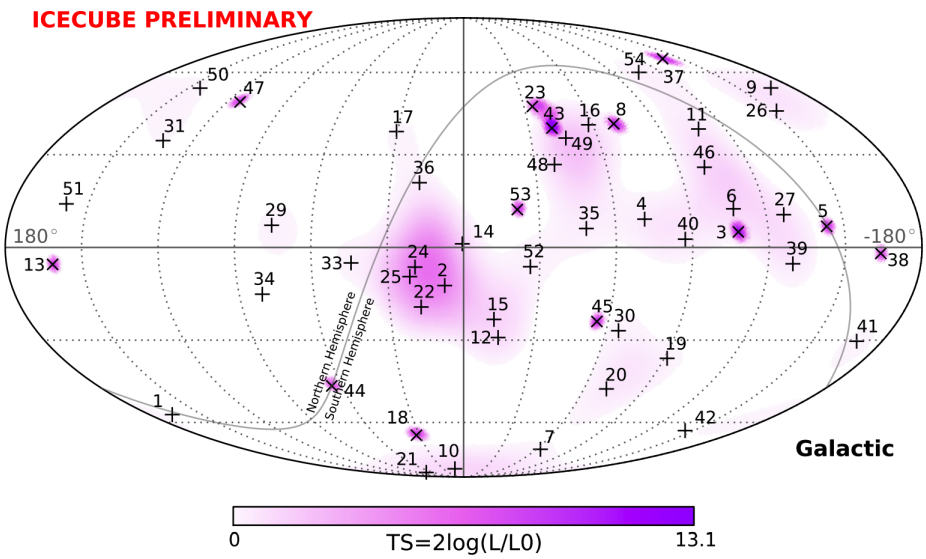

Figure 3.3: *This map in galactic coordinates shows neutrino events with their reconstructed direction at the time of their arrival. Track events are indicated by the "×" marker and those that have induced a shower are emphasized by the "+" marker. Figure taken from [87].*

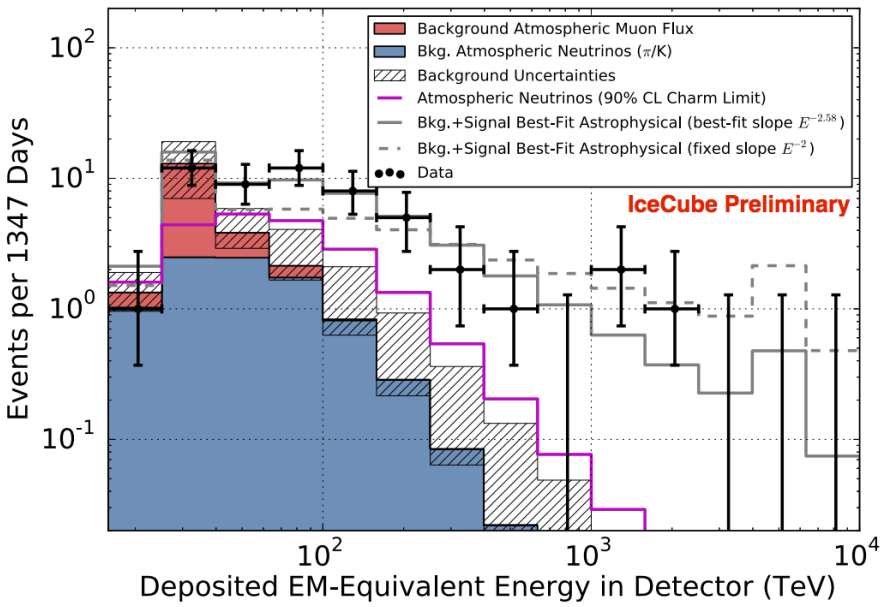

Figure 3.4: *In IceCube, a total number of 54 events have been measured in 1,347 days and this Figure shows them as a function of deposited energy. The uncertainty of the predictions of the atmospheric muons is 1σ. Figure taken from [87].*

3.4 The AMS-02 detector

The Alpha Magnetic Spectrometer Experiment (acronym: AMS-02) is a space-based cosmic ray detector that is mounted on the International Space Station (ISS) and was installed in May, 2011 [89]. Scientific goals cover a precise description of cosmic ray composition, search for dark matter and primordial antimatter.

The instrument consists of several individual detectors, see Fig. 3.5. A silicon tracker consists of nine planes, leading to high precision measurements of matter/antimatter ratios. Antimatter particles' curvatures are influenced by a strong magnet inside the detector and thus can be distinguished from common matter.

The Transition Radiation Detector (TRD) [90] identifies particles by detecting X-ray radiation. An electron, for example, emits X-rays when it passes through the TRD, which consists of alternating layers of plastic, felt and vacuum. The changing refraction index causes the electron to lose energy. A proton, on the contrary, will not emit X-rays.

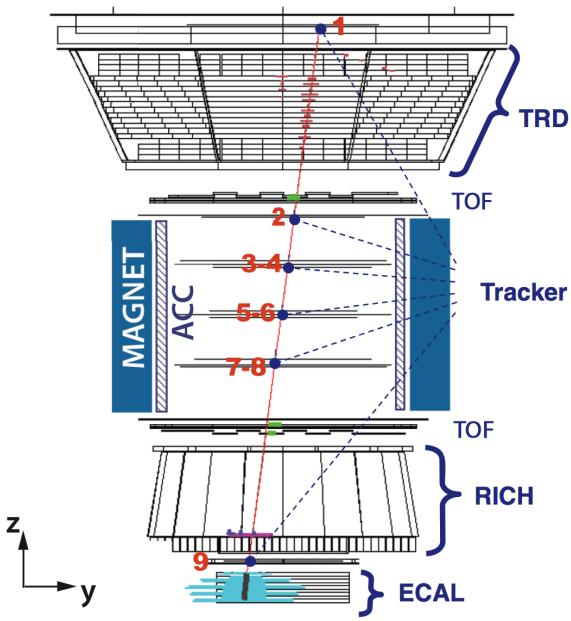

Figure 3.5: *The AMS-02 detector. The schematic view shows the individual detector system that complete the detector. Figure taken from [89].*

A further instrument is the the Electromagnetic CALorimeter (ECAL). One func-

tion of ECAL is the identification of protons and positrons. Both particles have the same charge and a low energy proton may have the same rigidity as a positron, making the identification difficult. The same is valid for electrons and antiprotons. The other function of ECAL is the detection of gamma-rays. Gamma-rays up to $E_\gamma \approx 300$ GeV can be resolved at high precision [91].

The Time-of-Flight (ToF) measures the particle's velocity, charge and direction [92]. It operates as a stop-watch for the AMS-02 detector and has a time resolution of $1.5 \cdot 10^{-10}$ s. Its goal is to trigger the other detector systems of the incident particle.

The Anti-Coincidence Counter System (ACC) is composed of 16 scintillator panels and detects particles with a precision of 99.99% that enter or exit the detector from the sides. In particular, the measurement of anti-nuclei benefits from this system because it prevents confusion about charge and momentum measurements. In combination with the ECAL, the total acceptance is 0.095 m^2sr [93]

The silicon Tracker mounted on AMS-02 measures the particle rigidity and specific energy loss. It is located in a $B = 0.8$ T magnetic field [94].

The Ring Imaging CHerenkov detector is able to resolve velocity and charge of a detected particle at high precision. The particles evoke Cherenkov radiation, which is converted into an electric current by photomultiplier tubes. The uncertainty of the velocity is $8 \cdot 10^{-3}$ for helium and is even lower for elements with higher atomic numbers [95]. The mass can be determined via the rigidity measured by the Tracker, charge obtained by the Tracker, ToF, and RICH, and the velocity, which can is obtained by RICH and ToF.

CHAPTER 4

The solar magnetic field

The Sun has been an object of special interest to many ancient populations and beliefs. Solar eclipses were already registered by the Babylonians. The oldest record is of about the year 1300 BC, see [96]. The invention of the optical telescope made a detailed record of Sun spots possible.

Since the 19th century the Sun has been studied extensively and newly developed instruments have made accessible further aspects of solar physics. For example, the optical spectrum indicates dark features, firstly noted by William Hyde Wollaston in 1802, see [97]. A few years later, in 1814, Joseph von Fraunhofer rediscovered these lines independently, and investigated their wavelength carefully [98]. These absorption lines are named after him, the Fraunhofer lines.
Samuel Heinrich Schwabe first observed a regular variation in the number of dark spots on the surface of the Sun in the years 1826 to 1843, see [99]. His work has been extended by Rudolf Wolf who observed Sun spots, too [100].

A direct measurement of the magnetic field is limited to regions that can be probed by spacecrafts. For example, the field could be measured by the Helios space probes not closer than 60 solar radii distance from the Sun [101]. At this distance, the strength of the magnetic field of the Sun has decreased significantly and only a fraction of the total magnetic flux can be investigated [102]. Therefore, other methods

have to be used in order to achieve a solid description of the Sun's magnetic field.

This chapter presents a few of relevant concepts and describes detection methods. Numerical approaches to extend experimentally obtained data will also be discussed.

4.1 Solar cycle

Dark regions on the surface of the Sun indicate strongly magnetized spots and vary over time. Their magnetic field was firstly measured by G.E. Hale in 1908, see [103]. Figure 4.1 shows the relation of the magnetic flux to the Sun spot number over time, and a 11-year cycle is apparent. However, a full solar magnetic cycle has a duration of about 22 years, see e.g. [102]. On longer time scales, a modulation of the solar activity is observable, see the lower graph of Fig. 4.2.

4.2 Sun spot number and features

The invention of the telescope opened up the possibility to count dark regions on the solar surface, and since the early 16th century a measure for the dark regions has been recorded. The definition of the Sun spot number goes back to that time [104]. Figure 4.1 shows the correlation of the Sun spot number (lowest graph) to the total magnetic flux at the surface, to the radio flux at a wavelength of $\lambda = 10.7$ cm and the solar irradiance measured on the Earth. It is therefore a reliable measure of the solar activity [105].

4.2.1 The latitude diagram

The upper part of Figure 4.2 shows the arrangement of the Sun spots and their movement over time. In the beginning of each cycle, they are found on a belt at $\pm 30°$ latitude. Gradually, these spots drift toward the equator of the Sun and by the end of each cycle they have almost reached it [102]. The latitude diagram has a symmetric structure, called the *butterfly* pattern.

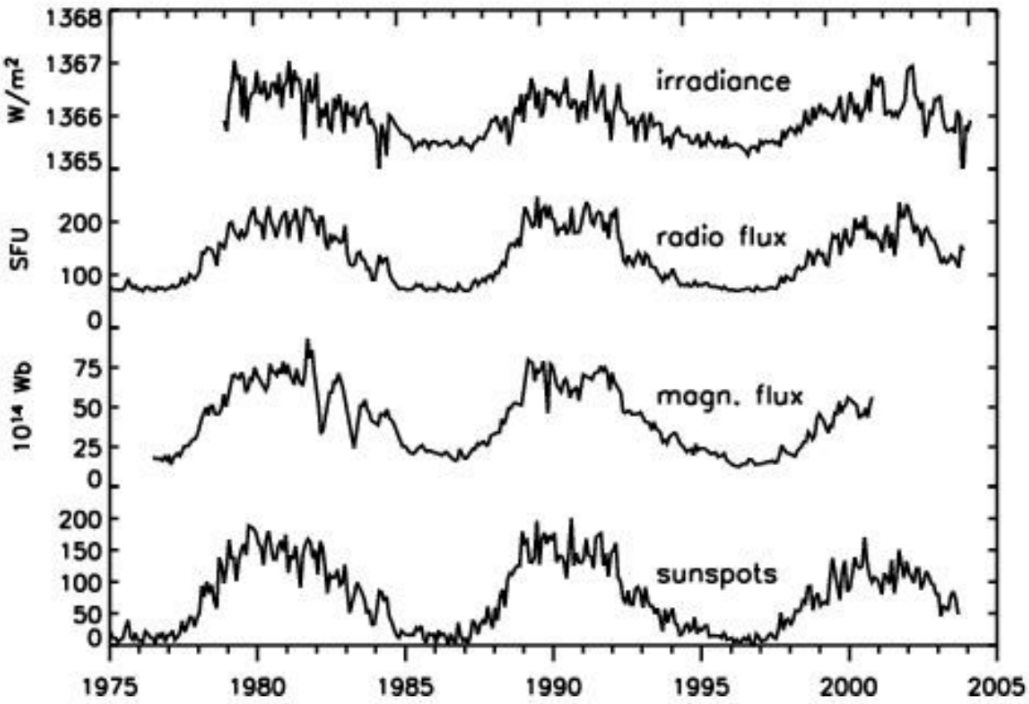

Figure 4.1: *Figure shows the correlation between quantities related to solar activity versus time. From top to bottom: The total solar irradiance at the top of atmosphere of the Earth; the radio flux at* $E = 2.8$ *GHz in solar flux units (SFU). 1 SFU =* $10^{-22} J\, s^{-1} m^{-2} Hz^{-1}$*; the total magnetic flux in the photosphere of the Sun; the Sun spot number provided by the Royal Observatory of Belgium. Figure taken from [102], see references therein.*

4.2.2 Bipolar regions

The polarization of Sun spots follows certain rules, firstly noted by Hale and Nicholson, see [106]. Studying the bipolar regions turned out to be valuable for modeling solar activity and the solar cycle, see [102] for further details.
In detail, the rules are the following, see [102]:

- During the 11-year cycle the magnetic orientation of the bipolar regions will not change.
- The magnetic field of the Northern and the Southern hemispheres is exactly oppositely oriented.
- With the change of the solar cycle also the magnetic orientation of the bipolar regions changes.

These rules were derived from observing the behavior of the Sun spot number. Consequently, the magnetic orientation will repeat after two cycles, which is 22 years for the Sun.

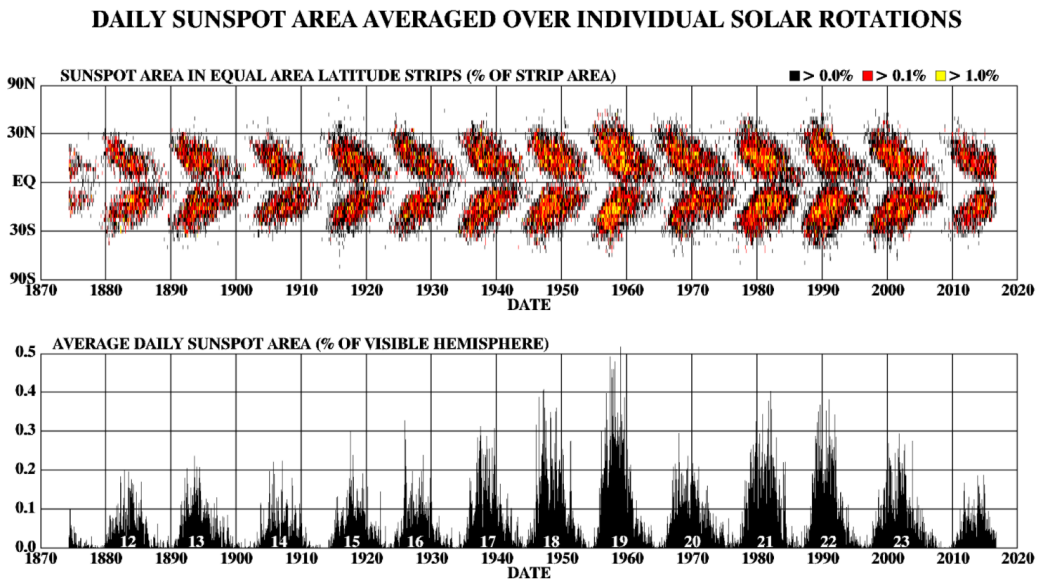

Figure 4.2: *The Greenwich Observatory has collected information about the number of Sun spots and their position and size. The upper plot shows that the Sun spots are not randomly distributed over the solar surface but are arranged in a certain pattern. Throughout time, a movement toward the equator can be noted, resulting in a butterfly structure. Figure taken from [107]*

4.3 The Zeeman effect and its application

In the presence of an external magnetic field, spectral lines are observed to be shifted in wavelength, and thus energy levels are shifted. In this section, the Zeeman splitting of a spectral line will be reviewed and it will be described how it can be applied in order to obtain information about the magnetic field of the Sun.

4.3.1 Zeeman splitting

In quantum mechanics, the Hamiltonian operator describes the total energy of a system. A perturbation can be added as a potential so that

$$H = H_0 + V_M \tag{4.3.1}$$

entirely describes the system, with H_0 the Hamiltonian of an atom, and V_M the magnetic perturbation term. The perturbation due to an external magnetic field can be defined through

$$V_M = -\vec{\mu}_j \cdot \vec{B}, \tag{4.3.2}$$

with $\vec{\mu_j}$ the total magnetic moment and $\vec{B}$ the magnetic field. The total angular momentum $\vec{J}$ is a superposition of the orbital electron angular momentum $\vec{L}$ and the spin $\vec{S}$ of the electrons, i.e. $\vec{J} = \vec{S} + \vec{L}$, and consequently, $\vec{\mu}_j$ is the magnetic moment corresponding to $\vec{J}$. Thus, the total magnetic moment is

$$\vec{\mu}_j = -\frac{\mu_B \left(g_\ell \vec{L} + g_s \vec{S} \right)}{\hbar}. \tag{4.3.3}$$

In the above equation, μ_B is the Bohr magneton and $g_\ell = 1$ and $g_s \approx 2$ is the absolute value of the electron spin g-factor [108], and $\hbar = h/2\pi$, and Planck's constant $h = 6.626 \cdot 10^{-34}$ Js. The magnetic moment can therefore be simplified to

$$\vec{\mu}_j = -\frac{\mu_B}{\hbar}\left(\vec{L} + 2\vec{S}\right). \tag{4.3.4}$$

The quantum numbers ℓ, s, j, and m_j define the state of an atom and the following relations hold

$$\vec{J}^2\psi = \hbar^2\ j(j+1)\ \psi, \tag{4.3.5}$$
$$\vec{S}^2\psi = \hbar^2\ s(s+1)\ \psi, \tag{4.3.6}$$
$$\vec{L}^2\psi = \hbar^2\ \ell(\ell+1)\ \psi, \tag{4.3.7}$$
$$J_z = \hbar\ m_j\ \psi, \tag{4.3.8}$$

It can be shown that all allowed combinations result in a splitting of each energy level into $2j+1$ sub-levels, with $j = \ell \pm s$.

The Landé factor of each energy level is an important quantity to describe the energy shift of a spectral line. It can be defined as [109]

$$g = 1 + \frac{j(j+1) + s(s+1) - \ell(\ell+1)}{2j(j+1)}. \tag{4.3.9}$$

The difference in wavelengths is a function of the involved magnetic field strength B and includes the two Landé factors corresponding to the energy level. The wavelength shift from the original wavelength λ_0 to the new one yields [109]

$$\Delta\lambda_B = \lambda - \lambda_0 = \frac{e}{4\pi c m_e} g^* \lambda^2 B \tag{4.3.10}$$

with $g^* = gm - g'm'$ and using prime notation for the higher energy levels. The traditional labelling of a normal and anomalous Zeeman effect refers to the initial and final conditions. When the transition occurs between singlet states, that is when $s = 0$, it is called the normal Zeeman effect. Usually, however, the total spin of both the initial and the final state is nonzero, and the name given for this process is the anomalous Zeeman effect.

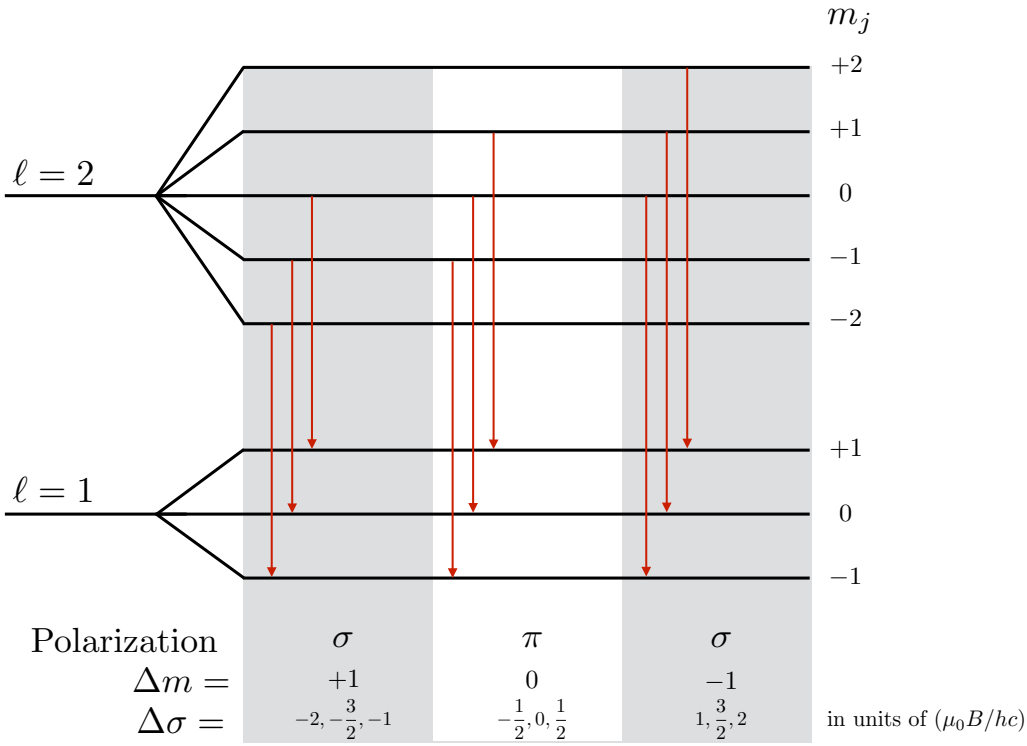

Figure 4.3: *Schematic view of Zeeman triplets in an external magnetic field. The relevant magnetic number are shown along to the Landé factors. Polarization is determined by Δm. Source adapted from [110].*

Two components of the Zeeman triplet are energetically shifted, denoted as σ, and one component, π, remains unshifted, see Fig. 4.3. Depending on the observer's view, not all components are visible. For example, in the case of the longitudinal Zeeman effect the line of sight is in the direction of the magnetic field, and only the two σ components are visible, and they show a circular polarization.

When the observer is perpendicular to the magnetic field, it is called the transverse Zeeman effect, and all three lines are visible and linearly polarized. The π component points perpendicularly to the B-field, while the σ components is linearly polarized in the parallel direction to the magnetic field, see [109].

The above rules are valid for absorption lines only. For emission, the circular polarization is reversed and in the case of the transverse Zeeman effect, parallel

and perpendicular must be exchanged [109].

4.3.2 Magnetograms - Applied Zeeman effect

A magnetogram is an image of a magnetic field, mainly used for visualizing the magnetic field of the Sun. The field can be mapped, and thus, magnetic changes in different regions become apparent. Figure 4.4 shows a magnetogram of the Sun (left), and a close-up image (right), in which more details are visible.

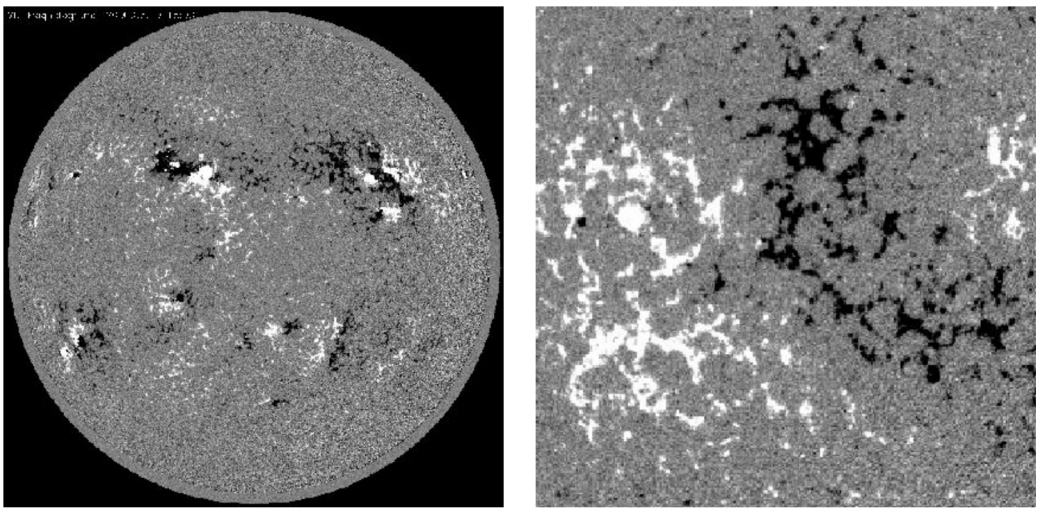

Figure 4.4: *Figure shows the distribution of magnetic flux on the solar surface. Black and white spots indicate positive and negative magnetic polarity, respectively. Left: A magnetic image of the Sun, showing the visible hemisphere. Image taken on July 31, 2000. Large bipolar regions and unipolar regions are visible. Right: A close-up shot that covers an area of* $160 \cdot 10^9 m^2$. *Figure taken from [102], see references therein.*

So-called magnetographs are capable of recording such a map, however, some instruments can only map the longitudinal component, for example the Michelson Doppler Imager onboard the Solar and Heliospheric Observatory (SOHO), see e.g. [111]. The magnetic fields in the photosphere of the Sun are studied in order to analyse the convection zone, as well as the structure of the corona [111].

The National Solar Observatory (NSO) Global Oscillation Network Group (GONG) is a union of several ground-based observation sites [112]. On their webpage [113],

Integral Carrington Rotation Magnetogram Synoptic Maps are published, of which the magnetic field of the Sun within a given time frame can be extracted. These maps are obtained by the SOLIS vector magnetograph [114], which additionally measures the perpendicular components of the field.

4.4 Potential Field Source Surface Model

The Potential Field Source Surface model for the global coronal magnetic field (PFSS) is a model that approximates large-scale structures in the field and this section will give an overview about its basic properties. The model can be refined by the usage of magnetograms, which can serve as a basis for obtaining the actual magnetic field of the Sun. Schatten, Wilcox, and Ness [115], as well as Altschuler and Newkirk [116], were the first to publish this model.

4.4.1 General information on the model

The idea of developing a potential field model in order to describe the magnetic structure of the Sun is based upon the study of energy densities of both the total magnetic field and the transverse component, as well as the thermal energy of the plasma and the plasma flow near the solar surface, see [116, 117]. From the comparison of these features, the authors of [115] found that below a distance of approximately two solar radii, $2R_\odot$, the thermal energy is the dominating quantity over the thermal and the bulk flow energy of the plasma. With increasing distance, the relative energy of the plasma, compared to the total magnetic energy, rises, and at approximately $20R_\odot$, it has reached the point where it eventually dominates over the total magnetic energy.
Based upon these findings, Schatten et al. drew the conclusion that below $2R_\odot$ the field can be effectively approximated by a potential field model, which drives the plasma flow [115].

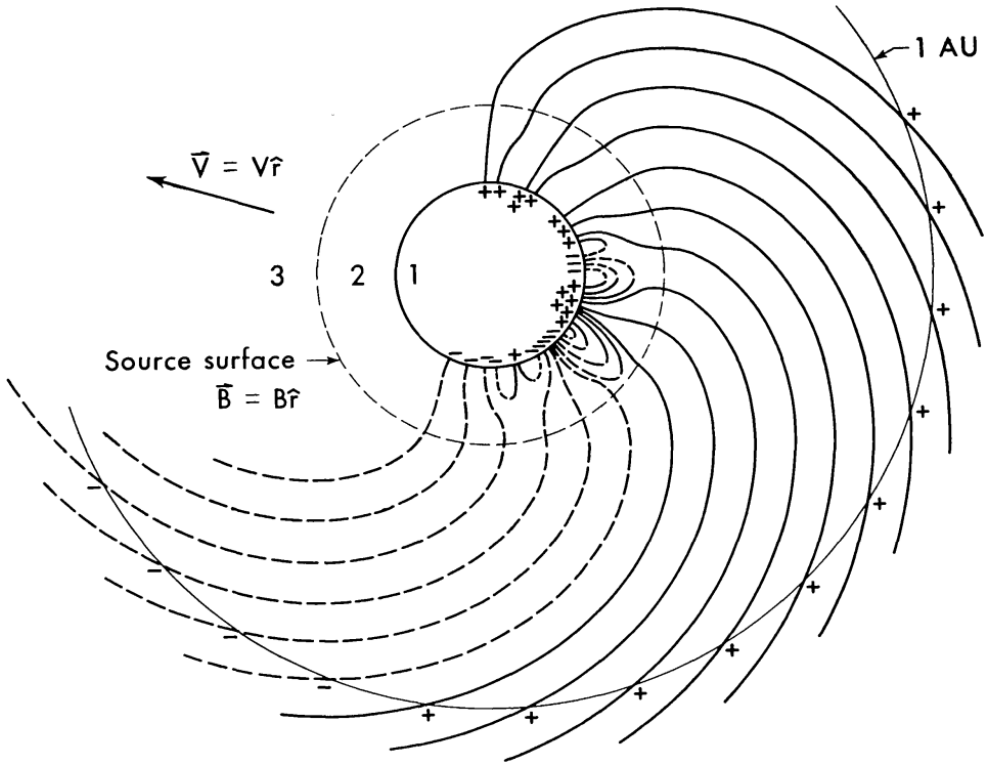

Figure 4.5: *Sketch of the basic idea of how magnetic field lines arrange within the PFSS model in the ecliptic plane. The two magnetic orientations are represented by solid and dashed lines, as well as the "+" and "−" sign. Region 1, the Sun, generates magnetic fields. Region 2, contains closed field lines, so-called magnetic loops. At the source surface, i.e. the boundary region between regions 2 and 3, transverse components are cancelled and thus the field is oriented radially at this boundary. Farther, due to the Suns rotation, the field lines are twisted. This effect leads to the Parker spiral [118]. Figure taken from [115].*

4.4.2 Basic concept

Figure 4.5 shows an illustration of the magnetic field as suggested by the PFSS model. The region between the solar surface and the source surface, $R_\odot < r < R_S$, is a complex field with strong magnetic fields and loops inside. Beyond R_S, the field becomes more organized and only the twist caused by the rotation of the Sun influences the field lines. Eugene Parker described this effect, and thus the field in region 3 of Fig. 4.5 is known as the Parker spiral [118].

In Fig. 4.6, a magnetogram is projected on the sphere of the Sun. The mag-

netic field lines indicate how the magnetic structure forms using the example of the Carrington rotation CR 2060 [119]. While the field diverges and opens to the heliosphere around the polar regions, most of the field lines above active regions closed within the source surface region.

The PFSS models after Schatten et al. [115] and Altschuler and Newkirk [116] apply a current-free corona. By neglecting also the electric field contribution, the magnetic field is rotation-free [115]

$$\nabla \times \vec{B} = \mu_0 \vec{j} + \mu_0 \epsilon_0 \frac{\partial \vec{E}}{\partial t} = \vec{0}. \tag{4.4.1}$$

Consequently, a scalar potential can represent the magnetic field

$$\vec{B} = -\nabla \psi, \tag{4.4.2}$$

with ψ the wave function. The requirement of a zero divergence ($\nabla \cdot \vec{B} = 0$) leads to the Laplace equation

$$\nabla \cdot (\nabla \psi) = 0, \tag{4.4.3}$$

which must be fulfilled. From the surface of the Sun magnetic field lines can stretch out to even farther distances than the so-called source surface at approximately $R_S = 2R_\odot$. Only in this domain, the current is equal to zero. In the rather small boundary region, where the plasma energy density becomes higher than the transverse magnetic field [115], magnetic field lines are more or less oriented radially. Thus, this region serves as a 'source' for the interplanetary magnetic field.

Altschuler et al. [120] suggested a solution for the potential field by using a spherical harmonics expansion, which will be presented in the following.

The base functions φ_{nm} are obtained by convoluting the spherical harmonic functions Y_{nm} with a linear combination of the radial functions r^n and $r^{-(n+1)}$. The boundary condition $\varphi_{nm}(R_S, \theta, \phi) = 0$ must be satisfied; therefore [121]

$$\varphi_{nm}(r,\theta,\phi) = \left(r^n - R_S^{2n+1} r^{-(n+1)}\right) Y_{nm}(\theta,\phi). \tag{4.4.4}$$

The indices in the above equation $n \geq 0$ and m, with $|m| \leq 0$, are the order of the harmonic function, respectively. The solutions of the Laplace equation (4.4.3) represent the φ_{nm} functions. Their base is orthogonal in θ, ϕ coordinates. A linear combination of the base functions approximates the magnetic potential solution [121]

$$\Phi(r,\theta,\phi) = \sum_{n=1}^{N} \sum_{m=-n}^{n} f_{nm} \varphi_{nm}(r,\theta,\phi), \tag{4.4.5}$$

with the highest order N in the expansion. The base function φ_{00} corresponds to the monopole term and is thus omitted. The derivative of Eq. (4.4.5) determines the coefficients f_{nm} by evaluating the magnetogram radial field at $r = 1$ [121]

$$M(\theta,\phi) = \sum_{n=1}^{N} \sum_{m=-n}^{n} f_{nm} \frac{\partial \varphi_{nm}(r,\theta,\phi)}{\partial r}\bigg|_{r=1} \tag{4.4.6}$$

$$= \sum_{n=1}^{N} \left[n + (n+1) R_S^{2n+1}\right] \sum_{m=-n}^{n} f_{nm} Y_{nm}(\theta,\phi). \tag{4.4.7}$$

Since the base functions are orthogonal, the coefficients are obtained through [121]

$$f_{nm} = \frac{1}{4\pi \left(n + (n+1) R_S^{2n+1}\right)} \int_0^{\pi} \mathrm{d}\theta \ \sin\theta \times \int_0^{2\pi} \mathrm{d}\phi \ M(\theta,\phi) Y_{nm}(\theta,\phi). \tag{4.4.8}$$

The authors of [121] point out that fitting the coefficients to Eq. (4.4.7) could be more efficient when the magnetogram does not cover the solar surface entirely, despite an expensive computational effort.

An analytical solution for obtaining the magnetic field is

$$\vec{B}(r,\theta,\phi) = \sum_{n=1}^{N} \sum_{m=-n}^{n} f_{nm} \nabla \varphi_{nm}(r,\theta,\phi), \tag{4.4.9}$$

with $1 \leq r \leq R_S$. Alternative approaches exist that obtain the magnetic field via numerical methods of finite differences.
The numerical recipe of iterative finite differences can be used in order to obtain a 3D magnetic field from a magnetogram. Tóth et al. have developed such a method in Fortran 90 and refer to it as FDIPS[1] [121]. It solves the Laplace equation on a $150 \times 180 \times 360$ spherical grid. For details about the implementation and the exact model, see [121].

4.4.3 Advantages & critics of the PFSS model

Riley et al. have reviewed the Pros and Cons of the PFSS model and compared its results to magnetohydrodynamic models (MHD), which are another possibility in order to compute the large scale and steady state magnetic field of the corona, see [122]. Both kinds of models make use of boundary conditions that are extracted from observations of the photosphere, e.g. magnetograms.

As advantages they point out the simple implementation and development of PFSS models. The required computational resources are rather low, especially with todays capacities. This, in turn, is also an advantage for MHD models. Furthermore, structures can be resolved to greater details than current MHD models can achieve.

Disadvantages affect the validity of such models in reality as their assumptions, such as the spherical-symmetric source surface, are so specific that they are unlikely to be found in nature. Modifications of the source surface incorporate, for example, a surface that deviates from the spherical symmetry especially in times of low solar activity [122], $R_S = 2.3\left(1 + 3\cos^2(\theta)\right)^{1/6} R_\odot$ with θ the magnetic colatitude. See [123, 124] for further details. Magnetic reconnection and other time dependent events cannot be resolved properly.

The authors of [122] anticipate an increase in the deviation of predictions provided

[1] Finite Difference Interative Potential field Solver (FDIPS)

by PFSS models and MHD models with the usage of vector magnetograms as provided by the SOLIS instrument [114].

It has been claimed that the current sheet source surface model (CSSS) [125] is more accurate than the PFSS model, see e.g. [126]. The authors of [126] report a factor of 1.6 higher accuracy of the CSSS model. This model is built on a more realistic coronal scenario, which includes horizontal and sheet currents, and can be used to extend the coronal magnetic field beyond the $2.5R_{\odot}$ solar radii of the PFSS model . A detailed description can be found in [127].

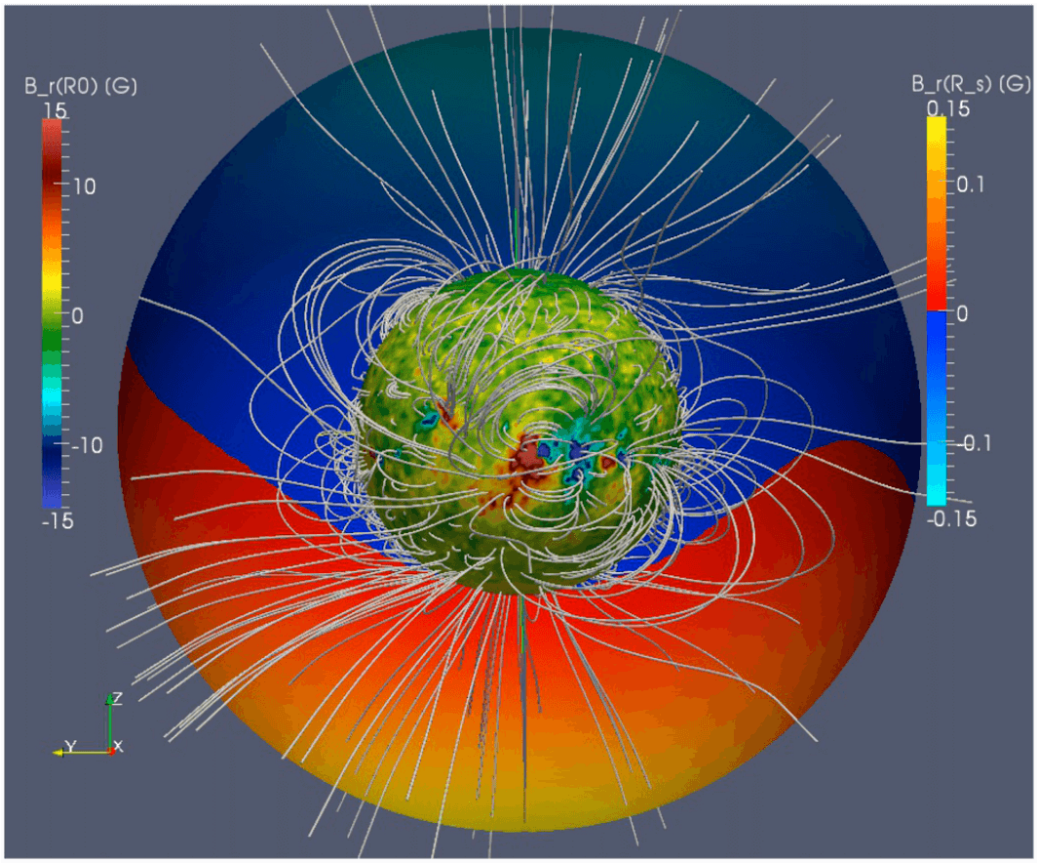

Figure 4.6: *Figure shows the PFSS model on the basis of the Carrington rotation CR 2060. The magnetogram is projected onto the inner sphere and shows the different regions of the magnetic field orientation along with its strength. The strength is limited to* ± 15 *G. The outer half-sphere visualizes the orientation of the field at the source surface. Magnetic field lines are also shown. Figure taken from [119].*

4.5 Sun shadow of cosmic rays

The flux of cosmic rays as measured on Earth is nearly isotropic. However, nearby sources may influence the isotropy and at a low level an isotropy is evident. This circumstance has been detected by IceCube [128], Tibet-III [129], and Milagro [130]. In this section, the basic idea is explained and current results of the Sun shadow analysis are given.

4.5.1 Basic concept and benefits of a Sun shadow analysis

Cosmic rays are fully absorbed by massive objects such as the Moon and the Sun and, therefore, create a deficit in the flux of cosmic rays when the detector points in that direction. In order to conduct a solid study of this effect, the IceCube experiment developed a specific Moon and Sun filter, which "follow" the Moon or Sun track in the Antarctic sky, see e.g. [131].
Fig. 4.7 shows a schematic view of how the Sun blocks cosmic rays.

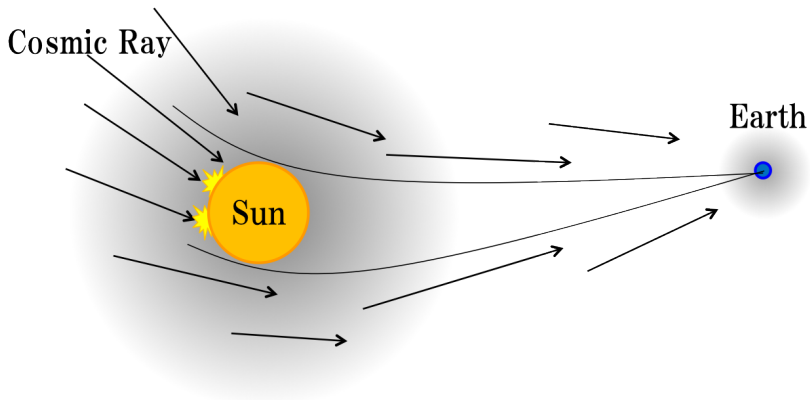

Figure 4.7: *The sketch shows a 2D simplification of the cosmic ray Sun shadow as it is measured on Earth and exaggerates the deflection of the particles through the magnetic field. Due to the deflection, the position of the Sun may be shifted and its size may also change. These effects depend strongly on the cosmic ray energy and the strength of the magnetic field. Figure taken from [132].*

In Fig. 4.7, it is indicated that the trajectories of cosmic ray particles are not straight as they are deflected. This schematic view illustrates the effect of the magnetic field on the charged cosmic rays that pass by. The deflection of cosmic rays depends on the strength and geometry of the field. As a result of the time variation of the field, it is thus expected that a temporal effect is also visible in the obtained data.

The Moon, on the contrary, does not have a magnetic field and therefore its shadow is expected to be constant in time. Although both objects have nearly the same opening angle from the viewpoint of the Earth, the presence of a magnetic field distinguishes the Sun from the Moon. The Moon can be used for the calibration of a detector, because a constant deficit in the data combined with the known position of this object allows an accurate study of the angular resolution of the detector [133, 134].

The study of the Sun shadow is a possibility to find a measure for analyzing its magnetic field. Cosmic rays would serve as indicators of the Sun's activities.

4.5.2 Results of Sun shadow analyses of IceCube and Tibet-III

This deficit in cosmic ray data caused by the Moon and the Sun has been quantified by MACRO [135], L3 [136], MINOS [137], ARGO-YBJ [138]. Even more recent studies of this effect have been published by the HAWC-experiment [139] and by the IceCube collaboration [131].

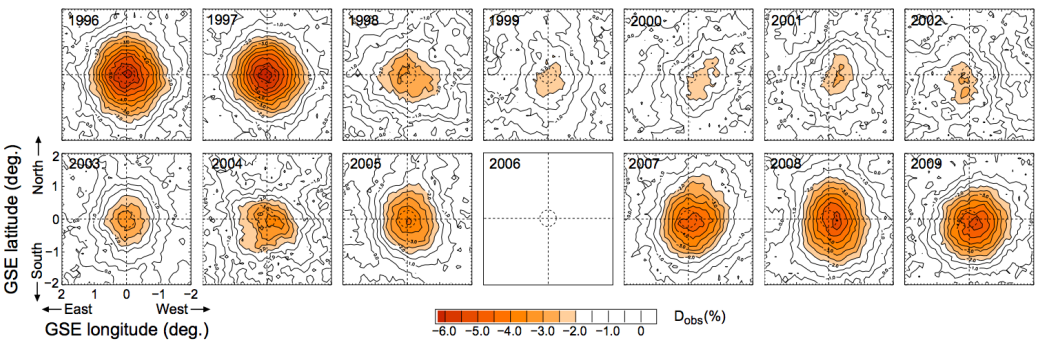

Figure 4.8: *Temporal variations of the Sun shadow detected by Tibet-III. In the year 2006, the detector was shut down and no data could be taken. The mean cosmic ray energy is* $E_{\mathrm{CR}} = 10$ *TeV. Figure taken from [140].*

The Tibet-III experiment has studied the Sun shadow from 1996 – 2009 [140], and their result for the Sun is shown in Fig. 4.8. While the Moon shadow did not change over time, a significant change in the Sun shadow is obvious [140].

Measurements with the IceCube experiment confirm this behavior at higher energies with a median energy of $E_{\mathrm{CR}} = 40$ TeV, although the analysis covers a different time frame. The depth of the Sun shadow decreases in times of high solar activity, and when the Sun spot number is low, the shadow is deeper. The study of the Moon shadow reports a constant depth, see Fig. 4.9 and figure 6.4 in [131].

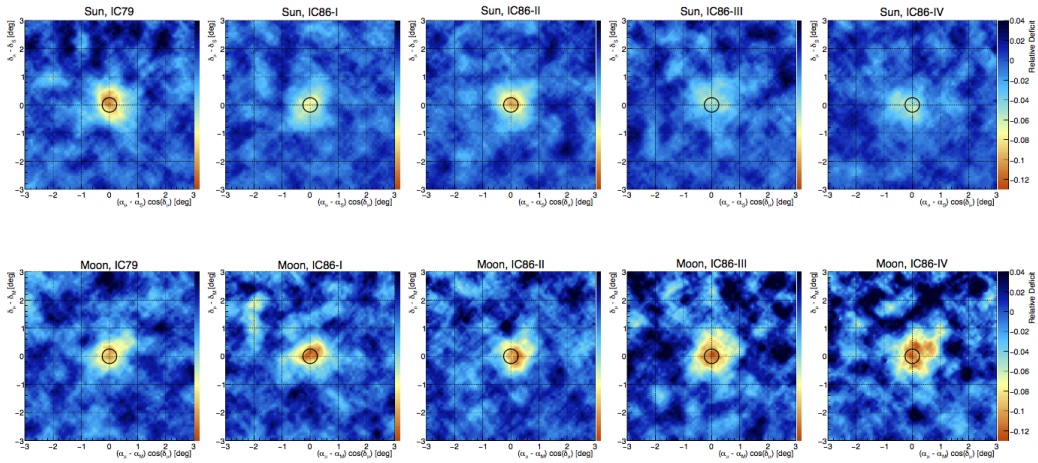

Figure 4.9: *Figure shows IceCube's 2D analysis of the Sun shadow (top row) and the Moon shadow (bottom row). The title of each Figure references the year. IC79 refers to the construction status of IceCube with 79 strings in the year 2010 and IC86-I is the currently completed construction of 86 strings of 2011. The denominations IC86-II, IC86-III, and IC86-IV refer to data samples obtained in the years from 2012 through 2014, respectively. Please note that the Sun is visible for IceCube only during the months of November through February. The Moon is present the whole year, for about eight days each month. Individual figures taken from [131].*

Moon and Sun cover an angular size of 0.5 degrees in the sky. The deficeit in this region is expected to be 100%, due to the interaction of cosmic rays with Moon or Sun. Experiments, such as IceCube, see a shadowing effect of approximately 12%. The angular uncertainty of these detectors smear the deficit. Thus events from the background are reconstructed in front of the position of Moon and Sun.

In [131], a correlation between the solar activity, and the shadowing effect of the Sun is calculated with 96% confidence. With higher solar activity, the shadowing effect of the Sun increases.

CHAPTER 5

Supernova remnants as cosmic ray sources

The first detection of cosmic rays by Victor Hess and others in the year 1912 [2] opened the possibility to an entire new field in astrophysics. Studies have shown that the differential flux follows a power-law in energy with two obvious features at 10^{15} eV and $10^{18.5}$ eV, the so-called *knee* and *ankle*, respectively, see e.g. [141, 142] and Chapter 2. It is believed that the flux originates from sources that can accelerate cosmic ray particles to these high energies. The flux, however, smears out due to magnetic fields that stretch out into the Galaxy. Therefore, detectors on Earth measure a highly isotropic flux, and sources cannot be reconstructed using only the information carried by those particles. In contrast to protons and heavier nuclei, gamma-rays and neutrinos are uncharged and propagate through space unaffected. Their signal comprises information about their origin and the primary cosmic ray energy can also be reconstructed from gamma-rays or neutrinos.

These three very different classes of particles provide clues to processes in the universe that are not yet fully understood. The main focus of this chapter is the propagation of charged cosmic rays and the possible source class of supernova remnants is investigated whether cosmic rays can be accelerated up to 1 PeV.

The cosmic ray spectrum as measured on Earth serves as a reference for the expected flux.

5.1 Propagation in GALPROP

The GALPROP code provides a tool to estimate the contribution of the observed cosmic ray flux by gamma-ray emitting supernova remnants. This analysis focuses mainly on the energy content with a fixed diffusion coefficient, keeping the number of free parameters to a minimum. The transport equation as implemented in GALPROP is solved through a Crank-Nicholson approach, see subsection 2.4.3 for details, and in its differential form is

$$\begin{aligned}\frac{\mathrm{d}\psi}{\mathrm{d}t}(\vec{r},t,E) = q(\vec{r},t,E) + \nabla\left(D_{xx}\nabla\psi - \vec{U}\psi\right) + \frac{\partial}{\partial p}\left[p^2 D_{pp}\frac{\partial}{\partial p}\frac{\psi}{p^2}\right] \\ - \frac{\partial}{\partial p}\left[\left(\frac{\mathrm{d}p}{\mathrm{d}t} - \frac{p}{3}\nabla\cdot\vec{U}\right)\cdot\psi\right] - \frac{\psi}{\tau_f} - \frac{\psi}{\tau_d},\end{aligned} \tag{5.1.1}$$

with p as the particle momentum and ψ the particle density per momentum for a specific point r in space. The cosmic ray spectrum at the source is denoted by the parameter q and represents either a discrete source spectrum or a continuous source distribution. A scalar diffusion and diffusive reacceleration is ensured by the constant coefficient parameters D_{xx} and D_{pp}, respectively. In the case of convection, $\vec{U}$ is the drift velocity of the particles, and the parameters τ_f and τ_d denote the time scales in which fragmentation and radioactive decay occur. Hadrons and leptons, along with their secondaries, are considered, and parameters described above are defined by species.

The GALPROP code provides the user with hadronic and leptonic spectra. Also included in the output is the gamma-ray emission at every predefined grid point, which is a result of bremsstrahlung, inverse Compton scattering and hadronic interactions.

5.1.1 Gamma-ray measurements and corresponding cosmic ray spectra

Of approximately 200 active supernova remnants in our Milky Way [143], only 10% indicate a hadronic component in their spectrum as derived in [40], making them valuable candidates for this simulation. These candidates are seen as a sample set within a supernova population, and hence their spectra serves as an input parameter in the GALPROP code. The source spectrum in units of $[j_p] = 1/\mathrm{MeV}$ is [59]

$$j_p(T) = a_p \left(\sqrt{\frac{T^2 + 2\,T\,mc^2}{T_0^2 + 2\,T_0\,mc^2}} \right)^{-\alpha_p} \frac{T + mc^2}{\sqrt{T^2 + 2\,T\,mc^2}} \times \tanh\left(\frac{T}{T_{\mathrm{min}}}\right) \exp\left(-\frac{T}{T_{\mathrm{max}}}\right), \tag{5.1.2}$$

with a_p as the normalization, T as the kinetic energy, m as the proton mass, and c the speed of light. In this equation, the hyperbolic tangent function mathematically implies a smooth cutoff at energies below $T_{\mathrm{min}} = 10$ MeV. In the simulation, however, the focus lies on cosmic ray energies in the range of 1 GeV $\leq E_{\mathrm{CR}} \leq 10^3$ GeV, and the low energy cutoff is therefore negligible. High energies are cut off by an exponential function at an energy T_{max} that depends on the individual supernova remnant, see Table 5.1. In order to simplify Eq. (5.1.2) without losing any validity, the reference energy is chosen as $T_0 = 10^3$ GeV.

SNR	d [kpc]	t_{age} [kyr]	α_p	a_p [10^{39}/MeV]	$T_{\max}$ [GeV]	$E_{\text{CR,tot}}$ 10^{47} erg
3C391	7.2	4.0	2.6	44964.2	10^6	3081.2
W41	4.2	100.0	2.4	52175.2	10^6	4438.1
W33	4.0	1.2	2.1	29694.1	10^6	966.0
W30	4.0	25.0	2.9	19853.4	$1.4 \cdot 10^4$	681.9
W28	1.9	33.0	2.8	9952.4	10^6	1874.6
W28C	1.9	n/a	2.5	2331.8	10^6	29.3
G349.7+0.2	18.3	10.0	2.4	332128.6	10^6	3155.2
CTB 37B	13.2	1.8	2.1	29721.8	10^6	3745.9
CTB 37A	7.9	16.0	2.6	92854	10^6	1241.3
SN 1006	2.2	1.0	2.3	2676.1	10^6	1227.6
Puppis A	2.0	4.6	2.5	4719.8	10^6	231.2
Vela Jr	1.3	4.8	1.8	16348.6	$4.4 \cdot 10^4$	1389.6
MSH 11-62	6.2	1.3	1.7	2869.8	46.0	4.2
W44	3.0	10.0	2.6	258.4	58.7	1.1
G40.5-0.5	3.4	30.0	2.0	22697.4	10^6	71.2
W49B	10.0	1.0	2.9	76237.4	10^6	1323.3
W51C	6.0	26.0	2.4	118406.8	10^6	7872.5
IC443	1.5	3.0	2.7	6046.8	10^6	85.2
Cygnus Loop	0.6	15.0	2.9	93.2	10^6	251.9
Cas A	3.5	0.3	2.3	19276.6	$3.7 \cdot 10^4$	2317.8
Tycho	3.5	0.4	2.3	2678.0	10^6	1813.6

Table 5.1: *This table shows the 21 remnants used in the simulation: The parameter d is the distance to the SNR, t_{age} stands the SNR's age, and α_p is the spectral index at the source. Further, a_p is the normalization constant at the reference kinetic energy $T_0 = 1$ TeV. The maximum energy of the spectrum, $T_{\max}$, is chosen as 1 PeV when no clear cutoff could be identified in the data. The total energy budget goes into cosmic rays and is denoted by $E_{\text{CR,tot}} = \eta \cdot E_{\text{SNR}}$. All parameters are taken from the work of [40].*

The proton spectrum at the source is shown in Fig. 5.1, and it is apparent that the individual spectra differ strongly from one another. In particular, the original energy budget ranges from 10^{47} erg to greater than 10^{51} erg. These sources that

do not reveal a cutoff up to the highest detected gamma-ray energies of around $E_{\gamma,\mathrm{max}} = 10$ TeV are assumed to contribute to energies up to the *knee*. It cannot be excluded that a few sources have an even lower maximum energy. However, the current status of research in this field does not allow a certain identification of which source is actually affected. Future data by new experiments such as HAWC and CTA will be an asset to higher precision analysis.

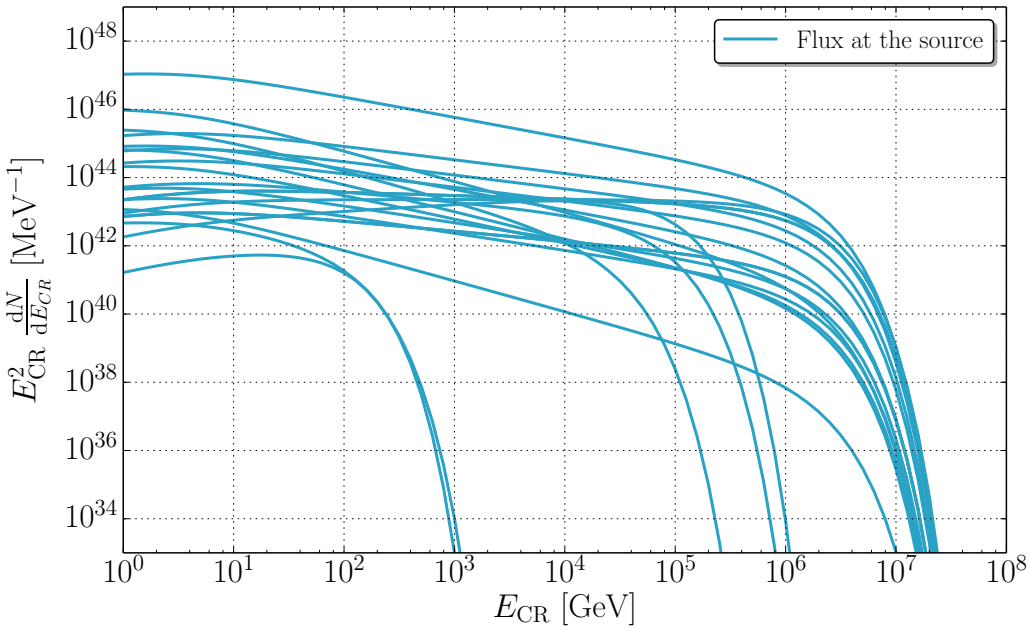

Figure 5.1: *This figure shows the proton spectra at the source, see Table 5.1. Each spectrum is to be propagated by the GALPROP code.*

5.1.2 Propagation of SNR spectra toward Earth

The measured cosmic ray spectrum on Earth is the average cosmic ray flux over a time frame of $\tau_{\mathrm{esc}} \approx 10^7$ years [31]. One population of active SNRs can be estimated to approximately $n_{\mathrm{SNR}} = 100$ [59]. The emitted cosmic rays diffuse through the Galaxy, and magnetic and electric fields deflect charged particles, so that they do not carry any directional information about their origin. Supernova remnants are believed to accelerate cosmic rays for $\tau_{\mathrm{SNR}} \approx 10{,}000$ years or more and their distribution follows the one of the massive stars in the Galaxy [59].

This section describes how the aforementioned set of SNR (Table 5.1) is used to simulate the diffuse cosmic ray flux that also contains cosmic rays from earlier SNRs.

Firstly, the set of $N_{\gamma-\mathrm{SNR}} = 21$ spectra that has been derived in [40] is assumed to be an exemplary configuration of different SNRs that exist in one population.

A) In this scenario, it is assumed that the spectrum represents the dominant cosmic ray spectrum over the average lifetime of a supernova remnant. A quasi-static emission scenario with an individual spectrum for all SNR is thereby achieved. One source injects a constant proton spectrum, as it has been derived from the gamma-ray spectrum. It remains constant for its entire lifetime. This method does not include a temporal evolution of the remnants.

B) In the second scenario, the injected spectra are intrinsically the same but with two differences: (i) the observation takes place at different times with respect to the initial explosion, and (ii) they have different total energies. This way, one time-averaged SNR spectrum is derived from the sample and each individual spectrum is weighted with the same total SNR energy. Then, all remnants are summed up, and this total spectrum is normalized by the average total energy in the SNR sample, that is $\langle E_{\mathrm{tot}} \rangle = 1.7 \cdot 10^{51}$ erg. This method allows the use of one quasi time-averaged spectrum for each source in the simulation, assuming it to be a representative cosmic ray emitting source in one population.

Due to the fact that at present gamma-ray detectors are limited to detecting cosmic rays from at most $d_{\mathrm{SNR}} \approx 10$ kpc [59], whereas the Milky Way stretches over a diameter of approximately $d_{\mathrm{G}} = 30$ kpc [144], it is clear that only a fraction of SNRs can actually be seen. The core collapse supernova, i.e. type Ib/c and type II, is estimated to occur $\nu_{\mathrm{SNR,cc}} = 1.9 \pm 1.1$ times per century [145]. Following the further assumption that a SNR emits cosmic rays in the Sedov-Taylor phase, which is the phase of adiabatic expansion and lasts $t_{\mathrm{ST}} = 10^4$ years, see e.g. [146] and [147], this leads to a total number of $N_{\mathrm{SNR}} \approx 100 - 200$ actively emitting high energetic cosmic rays. This number coincides with the number of shell-type SNRs that are detected at radio energies and listed in the Green catalog [143]. Although the SNR number in the catalog is close to 300, it is important to point out that radio emission can appear even after the Taylor-Sedov phase. Time scales

of radio emission can extend to $\tau_{\text{radio,em.}} > 10^5$ years [148]. Merely stronger SNR sources contribute to the cosmic ray emission, and thus the catalog's number and the number estimated here are in accordance.
The exemplary set of supernova remnants used in the simulation is only a fraction

$$1/\alpha = \frac{N_{\gamma-\text{SNR}}}{N_{\text{SNR}}} \approx 1/8 \tag{5.1.3}$$

of all active SNRs. One goal of the propagation simulation is to estimate the parameter α in Eq. (5.1.3), as it serves as the weighting parameter. The resulting normalization from the simulation of the 21 SNRs must be weighted by the factor α in order to represent the total energy provided by the sum of all SNRs existing at the moment.

Secondly, in the simulation only parameters describing spectral characteristics of one individual SNR are fixed, unlike its position. This ensures that the observed cosmic ray flux on Earth effectively contains cosmic rays from the past 10^7 years. It is unclear where early supernova explosions took place because the remnants have cooled down already and became inactive. The emitted cosmic rays, however, are still traveling through space, and some reach Earth and are registered by our detectors. This factor of uncertainty is incorporated by a random selection of positions for every SNR in the sample following the mass distribution in the Galaxy. The implemented distribution function is already included in the GALPROP code and can be found in [149]. This function determines the probability of one SNR to be found at a certain position. GALPROP then internally finds the nearest node in the grid that has been initialized beforehand and allocates the SNR's position to that grid point.
This strategy can be improved with a finer resolution of the grid, however, discrepancies will always remain. An accurate representation of the locations of early and still active SNR's is not available at this time [150]. The authors of [59] therefore refer to this circumstance as a first order approximation. Further work facing this uncertainty is still required [150]. Due to the large distances between the grid points defined in GALPROP, $\Delta x, \Delta y \gg 10$ pc, the supernova remnants are considered to be point-like sources.

Thirdly, in this simulation, statistical reasons in this simulation play a significant role. A high number of supernova remnants, $m = 20{,}000$, become active at the same time and remain so for 10,000 years. Each remnant out of the sample of 21 SNRs provides one simulated SNR with a randomly chosen spectrum. The simulation result must be re-weighted by the number of the assumed active SNR in our Galaxy in a specific time frame. In [59], the total number of $N_{\mathrm{SNR}} = 100$ is used. As shown above, this assumption is reasonable, because the total number of SNRs detected on Earth also reflects young supernova remnants, which are not yet capable of accelerating particles to energies as high as the *knee*. The uncertainty of the total number of relevant supernova remnants is estimated to be $\Delta N_{\mathrm{SNR}} = 50$. The obtained normalization must be adjusted properly [59]

$$\Phi_{\mathrm{res}} = \frac{N_{\mathrm{SNR}}}{m} \times \Phi_m = \frac{100}{10{,}000} \times \Phi_m. \tag{5.1.4}$$

The method described can be adopted as a reasonable approach due to justified assumptions. Limitations are as follows: The set of 21 SNRs represents around one tenth or one fifth of all active supernova remnants. It is unclear whether this sample indeed represents one population well enough. The Fermi satellite provides these gamma-ray observations in the GeV range, while other experiments such as H.E.S.S., MAGIC and VERITAS, see e.g. [151–154] even extend the range to TeV. Energies range from a few GeV to about 100 TeV, hence, energies up to the *knee* are not included.

Sources with a flat spectrum may contribute to the total cosmic ray spectrum, however, they do not show a distinct pattern below TeV gamma-rays. In statistical terms the sample set of SNRs may not be significant. New experiments such as HAWC [155] and CTA [156] will be helpful for increasing statistical significance. It is expected that these experiments can explore an energy of up to 300 TeV [156].

Based upon the aforementioned criticism on the method presented here, it must be said that this is only the beginning of an analysis that includes measured spectra. With the help of next generation experiments, statistical demands can be better fulfilled.

5.1.3 Individual SNR normalization

Cosmic ray normalization in standard GALPROP calculations is usually performed through a global scaling of the calculated cosmic ray flux. This flux will then coincide with the observed flux on Earth. In this work, it is the aim to investigate whether the cosmic ray energy budget can be met. The flux is therefore not renormalized but compared to the cosmic ray data. The source spectrum $j_p(T)$ needs to be adjusted accordingly.
In this approach, the luminosity L calculated by GALPROP to its integral expression in terms of $j_p(T)$ [59]

$$L = \xi c R_{\mathrm{SNR}}^2 \int_{10\ \mathrm{MeV}}^{10^9\ \mathrm{MeV}} \mathrm{d}T\ \frac{\beta\ T\ j_p(T)}{V_{\mathrm{SNR}}}. \tag{5.1.5}$$

In this equation, R_{SNR} denotes the radius of the supernova remnant and $V_{\mathrm{SNR}} = \frac{4}{3}\pi R_{\mathrm{SNR}}^3$. The parameter ξ defines whether cosmic rays exit radially, $\xi = 1$, or whether they move in random directions inside the SNR, $\xi = 1/2$. The latter implies an averaging over all angles.
The comparison between the calculated luminosity and the integrated value requires a reformulation of the initial source function $q_1(p(T))$ as it appears in GALPROP. The spectrum parametrization $j_p(T)$ becomes [59]

$$q_1\left(p(T)\right) = \alpha\ \frac{c^2 R_{\mathrm{SNR}}^2 \beta^2}{4\pi\ V_{\mathrm{grid}}} j_p(T). \tag{5.1.6}$$

Another approach to find the correct normalization factor is to derive the luminosity from the total energy E_{tot} of the protons in the SNR. This way, the luminosity is determined by $L = E_{\mathrm{tot}}/\tau$, where τ is a time scale that represents the distribution of the total energy over the SNR's entire lifetime [59]

$$L = \frac{1}{\tau} \int_{10\ \mathrm{MeV}}^{10^9\ \mathrm{MeV}} \mathrm{d}T\ T\ j_p(T). \tag{5.1.7}$$

Then, the spectrum parametrization changes to [59]

$$q_1'\left(p(T)\right) = \beta c\,\frac{R_{\mathrm{SNR}}^3}{3V_{\mathrm{grid}}\,\tau} j_p(T). \tag{5.1.8}$$

With E_{tot} as the amount of energy that all ejected protons carry and τ the time frame in which the SNR is active, i.e. its lifetime, the quantity $L = E_{\mathrm{tot}}/\tau$ can be seen as the averaged cosmic ray luminosity.

Other than the time-dependent energy spectrum, a more precise calculation would include a reduced maximum energy with advancing time and cooling effects, see e.g. [157]. These characteristics would fail an assumption of a constant rate converting into hadronic cosmic rays. Especially for old SNRs, the average cosmic ray luminosity would be underestimated. Energy spectra steeper than E^{-2} are dominated by a lower threshold, which means that temporal changes should be rather small. It is not known whether the fraction of cosmic rays resulting from the energy budget is constant or depends upon the actual total energy budget.
By keeping in mind these uncertainties, this calculation can serve as a first order approximation, and in this respect the energy budget can be derived from a reasonable assumption.

This analysis applies the normalization scheme as described above. Individual SNRs will be normalized with respect to their total energy and also with each other. This way, the result realistically represents the spectral energy behavior and the normalization of the spectrum.

5.1.4 Cosmic ray nuclei

The propagation routine GALPROP provides an option for simulations to be performed not only for protons but also for heavier nuclei, see e.g. [158]. With mass number A, momentum p_A, the initial source function $q_A(p_A)$ relates to $q_1(p_1)$ via the relative abundance [59]

$$X = \frac{A \cdot q_A(p_A)}{q_1(p_1)}. \tag{5.1.9}$$

In general, the quantity X depends upon energy and is important due to the

cutoff at a very high energy in Eq. (5.1.2). One technical side effect pertains to including heavier nuclei in the simulation. By adding them, the total energy of hadrons increases artificially, however, a downscaling of the proton normalization in Eq. (5.1.2) counteracts this feature sufficiently. The proton spectra derived in [40] are adequately adjusted.

Here, the simulations include all nuclei, but only the proton energy spectra are presented in their results. Future work on this simulation should include spectra of nuclei with higher mass numbers. This would give a more detailed view of cosmic ray composition and their origin and transport to Earth. Other effects, such as photohadronic interactions and spallation, are usually negligible for the considered length scales and the electromagnetic galactic fields.

5.1.5 GALPROP settings

GALPROP can be used for a variety of applications regarding cosmic ray propagation. The user is given a long list of parameters that can be changed according to the needs. In this section all changes to the original code are mentioned, see also [59].

1. **The normalization scheme**
   The GALPROP code has been adjusted in such a way that supernova remnants can be injected with their individual parameters, see Tab. 5.1. As cosmic ray emitters, the SNRs contain information about their position in relation to Earth and their extension. Then, a random selection of the spectral index, corresponding spectrum normalization, and maximum energy as derived in [40] is assigned to the source. In a last step, the position of the source in the GALPROP grid is chosen randomly but following the distribution function, see [149]. The calculated position will then be allocated to the closest grid point. At these points, GALPROP evaluates the spectrum.

2. **The size of the Galaxy**
   This simulation treats the Galaxy as a three-dimensional object, which is sliced into a grid. All grid points are arranged in a cartesian system with a distance to every grid point of $d_{\text{grid}} = 1$ kpc. The extension of a remnant is thus negligible, and they can be considered to be point-like sources. The results in [59] are presented for two different configurations in the size of

the Galaxy, a large and a small Galaxy. The large Galaxy extends in the $x - y$ plane from -20 kpc $< (x, y) < 20$ kpc, while the small Galaxy reaches only half as far in each direction as the large one. The small Galaxy is only used for testing the propagation, because such a simulation is significantly faster. The tests have shown that the results are comparable, and in results presented later, only the large Galaxy is shown.
In both configurations, the vertical component ranges from -4 kpc $\leq z \leq 4$ kpc with the same distance to the next grid point as in the $x - y$ plane.

3. **The diffusion coefficient**
   In this analysis, the diffusion coefficient is under investigation as well. Using a Kolmogorov-type diffusion, i.e. $D_{xx} = E^{\delta}$, two different diffusions are examined; a standard diffusion of $\delta = 0.33$ and a steeper diffusion of $\delta = 0.50$.

4. **SNRs as input parameters**
   Lastly, two different sets of supernova remnants are used as input sources to the GALPROP code. The first set is rather theoretical and serves only as a rough estimate of whether a sample SNR can provide a more or less expected flux. In this case, the total energy is fixed at $E_{\mathrm{CR,tot}} = 10^{50}$ erg, and the spectral index remains unchanged, but the flux caused by three spectral indices – namely $\alpha_p = 2.0$, 2.3, 2.5 – is examined. The purpose of this cross check is to examine the rough estimation described above. This is often an argument used to suggest SNRs as sources that can accelerate cosmic rays up to the *knee*.

   The second set of SNRs includes the individual spectra and further parameters as derived in [40]. This analysis aspires to the same goal as the study using an example remnant, however, with the individual parameters, it is expected to obtain a more sophisticated and reliable result. The spectral index accounts for an uncertainty of 1σ. The final plots show a band of this uncertainty in order to visualize the effect.

A GALPROP simulation uses a text file where parameters regarding the simulation setup are defined. This text file is named GALDEF and must be changed for non-standard simulations. In Tab. 5.2, the changes of a basic standard file are listed.

Parameter	Unit	Original Galdef	Our Modifications
Grid options and spectra			
r_min	kpc	0.0	0.0
r_max	kpc	30.0	25.0
x_min	kpc	0.0	-20.0
x_max	kpc	+20.0	+20.0
dx	kpc	0.2	1.0
y_min	kpc	0.0	-20.0
y_max	kpc	+20.0	+20.0
dy	kpc	0.2	1.0
z_min	kpc	-4.0	-4.0
z_max	kpc	+4.0	+4.0
dz	kpc	0.1	0.2
p_min	MV	1000.0	1000.0
p_max	MV	4000.0	4000.0
p_factor		1.2	1.3
Ekin_min	MeV	1.0e1	1.0e1
Ekin_max	MeV	1.0e7	1.0e9
Ekin_Factor		1.2	1.3
E_gamma_min	MeV	0.1	100.0
E_gamma_max	MeV	1.0e6	1.0e6
E_gamma_factor		10.0	1.5
long_min	deg	0.5	0.0
long_max	deg	359.5	360.0
lat_min	deg	-89.5	-90.0
lat_max	deg	+89.5	+90.0
d_long	deg	10.0	1.0
d_lat	deg	10.0	1.0
healpix_order		7.0	6.0
Cosmic Ray propagation parameters			
nuc_rigid_br	MV	1.0e4	1.0e2
nuc_g_1		2.23	2.43
nuc_g_2		2.43	2.43
inj_spectrum_type		rigidity	powerlaw

Table continues on the next page

Parameter	Unit	Original Galdef	Our Modifications
electron_g_0		2.1	2.5
electron_rigid_br0	MV	1.0e3	1.0e3
electron_g_1		2.3	2.50
electron_rigid_br	MV	1.0e4	1.0e3
electron_g_2		2.50	2.50
Parameters controlling interstellar medium			
He_H_ratio		0.11	0.11
n_X_CO		10.0	9.0
X_CO		1.9e20	1.9e20
max_Z		28.0	1.0
Parameters controlling propagation calculation			
start_timestep	years	1.0e7	1.0e9
end_timestep	years	1.0e1	1.0e2
timestep_factor		0.5	0.5
timestep_repeat		20.0	20.0
network_iterations		1.0	2.0
network_iter_compl		1.0	2.0

Table 5.2: *This table compares original GALDEF parameters, see Ref. [51], to the changes that have been made in the presented analysis.*

5.2 Results and conclusions

In this section, the results of the aforementioned simulation are presented. The focus lies on the high-energy region, in particular energies above $E_{\mathrm{CR}} \geq 10$ GeV. The instrumentation in gamma-ray experiments has a high precision in the range 1 GeV $< E_\gamma <$ 10 TeV, which corresponds to cosmic ray energies 10 GeV $<$ $E_{\mathrm{CR}} <$ 100 TeV. Spectra of supernova remnants, which have no evident cutoff at $E_{\mathrm{CR,th}} = 100$ TeV, receive an artificial cutoff at the *knee* energy.

5.2.1 Validation of the method

It is useful to test the validity of the simulation approach, for which two testing routines are applied. The statistical convergence of the flux is demonstrated in

Fig. 5.2. It is shown how the spectrum converges to a certain value for a given energy by using a different numbers of SNRs. While the spectrum for $N_{1,\mathrm{SNR}} = 5{,}000$ still shows a large deviation, the spectra $N_{2,\mathrm{SNR}} = 20{,}000$ and $N_{3,\mathrm{SNR}} = 30{,}000$ differ only slightly, as can be seen in the ratio plot of Fig. 5.2. The ratio refers to the flux with the highest number of SNRs, i.e. $N_{3,\mathrm{SNR}}$, and in all cases the flux is normalized according to Eq. (5.1.4). The convergence is non-monotonous, which indicates that a simulation of too few SNRs would lead to a systematical error.

Ideally, all simulated spectra should give a similar result, and simulations with a greater number of sources should give a more precise result. Fig. 5.2 shows that the deviation of 20,000 simulated SNRs is $\Delta N_{2,\mathrm{SNR}} \leq 1\%$. In order to save computation time but to still receive results to an acceptable precision, $N_{2,\mathrm{SNR}}$ has been chosen as a useful number of injected sources for the further calculations.

In a second test simulation, the example supernova remnant is investigated. In this case, the maximum energy, the luminosity, and the spectral index are fixed to a constant value, respectively. The normalization satisfies a luminosity of $L = 2 \cdot 10^{41}$ erg/s, see Eq. (2.3.1). The spectral behavior follows a power-law

$$j_{\mathrm{std}} = A \cdot \left(\frac{E}{E_0}\right)^{-\gamma} \cdot \exp\left(-\frac{E}{E_{\mathrm{max}}}\right) , \tag{5.2.1}$$

with A the normalization and $E_{\mathrm{max}} = 10^{15}$ eV. This simulation is expected to provide a reference for the total energy budget, and the spectral index is varied and adopts three different values, i.e. $\gamma = 2.0,\ 2.3,\ 2.5$. The diffusion follows a Kolmogorov type diffusion, and thus the diffusion coefficient is $\delta = 1/3$. It is also possible to assume a steeper spectrum, such as $\delta \approx 2/3$, however, a steeper spectrum in either the diffusion or the primary cosmic ray spectrum has the same effect. Therefore, the test presented in [59] leaves the diffusion coefficient unchanged while spectral investigations only apply to the primary spectrum. The obtained spectrum is shown in Fig. 5.3. The ratio plot in this figure makes it obvious that the deviations of all spectra, compared to the simulation with the highest number of SNRs, are $\Delta N_{\mathrm{SNR}} \leq 1\%$.

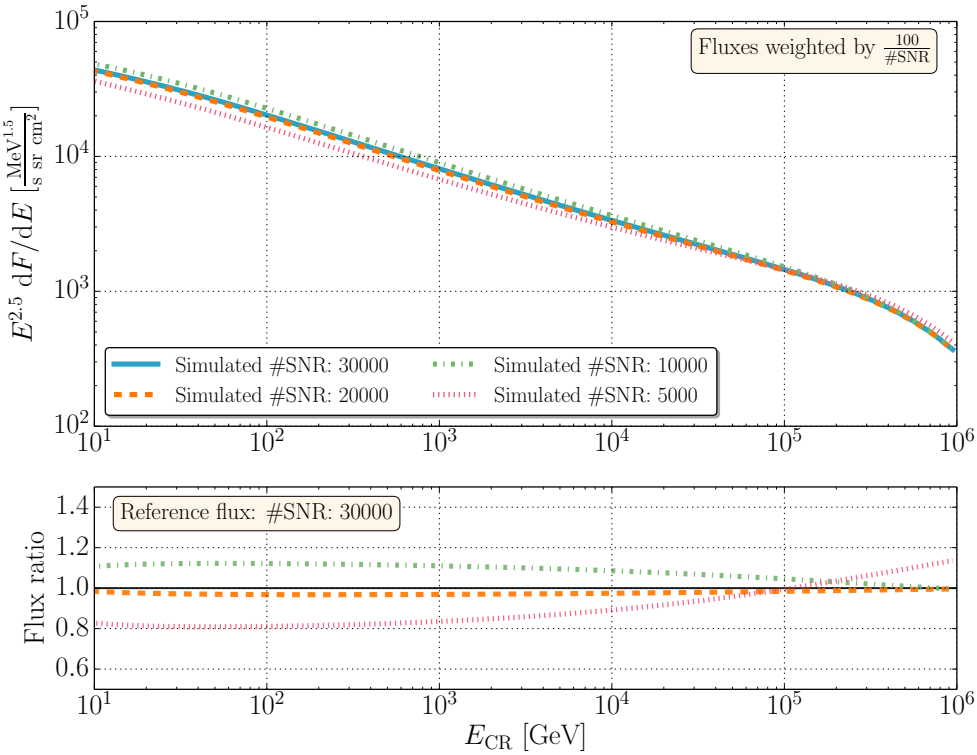

Figure 5.2: *This figure shows the simulated flux for a different number of SNRs with individual spectra, see Eq. (5.1.2). The convergence of the spectrum in the presented method is shown here. It appears that* $N_{\mathrm{SNR}} = 20{,}000$ *is a sufficient number.*

Figure 5.4 shows the different behavior of a variable spectral index, while all other parameters are fixed and uniform for every source. Here, the total number of simulated SNRs is $N_{\mathrm{SNR}} = 10{,}000$, because the simulated spectra of more or fewer SNRs show a negligible difference, see lower panel of Fig. 5.3. Also shown is the difference of the spectrum by using the small or the large Galaxy configuration. Compared to the uncertainties of other parameters, this difference can be ignored. However, since the large Galaxy is considered to represent a more realistic result, due to its more realistic assumption of the Galaxy size, the following plots will show only these results of the simulation.

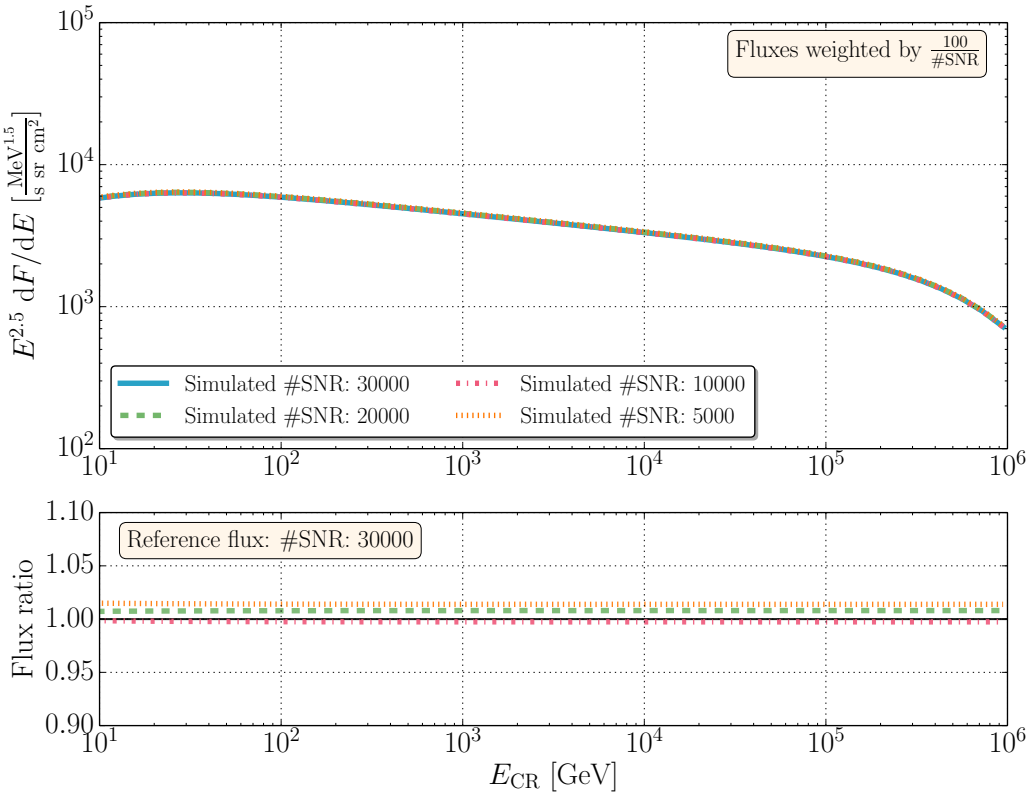

Figure 5.3: *This figure shows the simulated flux for a different number of SNRs with unique parameters. The convergence of the spectrum in the presented method is shown best in the case of 30,000 SNRs. It appears that* $N_{\mathrm{SNR}} = 20{,}000$ *is a sufficient number.*

Another feature of Fig. 5.4 is the underestimation of the flux data points by the simulation of a factor of $\Phi_{\mathrm{data}}/\Phi_{\mathrm{sim.}} \leq 5$. It is only the flattest spectrum, i.e. E^{-2} combined with a Kolmogorov-type diffusion, that overestimates the measured data at high energies and underestimates them by far at low energies. In general, such a flat spectrum is possible, but in this simulation not a realistic scenario. However, steeper spectra result in a range that is acceptable within the margin of error of this calculation. Although parameters such as the supernova explosion rate and the remnants' average energy budget are very uncertain, this result is still considered to be compatible with respect to the energy budget.

The measured spectrum can only be described by a broken power-law. In the low-energy regime below a few TeV, the spectrum follows approximately an $E^{-2.5}$ behavior, see dashed lines in Fig. 5.4. For higher energies, a softer spectrum is applicable, shown as solid lines in the same figure. As for a stronger diffusion, i.e. $E^{0.6}$, the primary spectra is required to be softer. A full description of the spectrum in the given energy range can be achieved by either a broken power law at the source, see e.g. [159–161], or in the energy behavior of the diffusion coefficient.

Already with the simplifying assumptions of the numerical approach the general statement that SNRs are capable of reproducing the energy budget of the cosmic ray spectrum up to the *knee* although the spectral behavior is disputable. In the next step, all individual SNR spectra are used to test whether these hold against the question whether they are a valid representing set of the class of dominating sources or not.

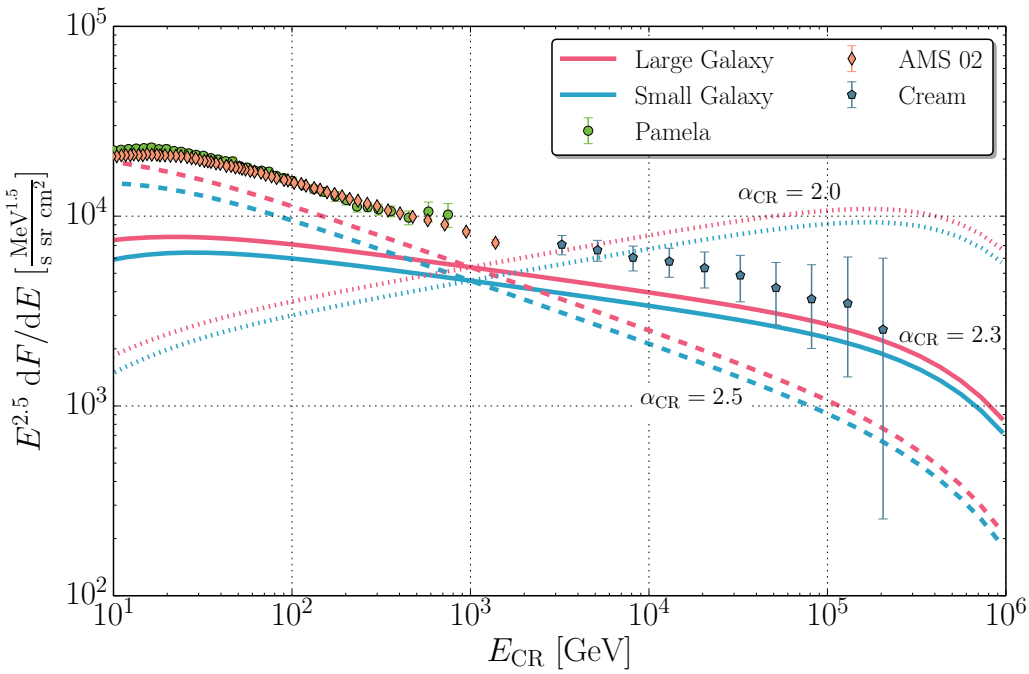

Figure 5.4: *This figure shows the simulation of 10,000 SNRs, all of which have the same parameters, i.e. the same maximum energy and luminosity. Three generic spectral indices have been tested for the large (red) and small (blue) Galaxy configuration. Figure taken from [59]*

5.2.2 Results for the individual SNRs

This section shows the results of the propagation simulation using the 21 SNRs with the obtained gamma-ray spectra by the analysis of Ref. [40]. Both scenarios, the quasi static emission scenario (A) and the quasi time-averaged spectrum (B), are presented, see subsection 5.1.2.

In Fig. 5.5 the spectrum is shown for the large Galaxy using a Kolmogorov-type diffusion, i.e. $D \propto E^{0.33}$. The error band shows the 1σ uncertainty on the spectral index of both higher and lower than reported in [40]. The data of cosmic rays as obtained by the experiments CREAM, PAMELA and AMS-02, to be found in [162–164], lie within the error band and can be explained by the individual supernova remnants used. The spectrum itself is a little steeper compared to the measurements. Naturally, the calculated flux allows a large uncertainty but future experiments with a higher precision may confirm the result.
Figure 5.6 shows the same configuration of the Galaxy and SNRs but with $D \propto E^{(}0.5)$. While the low energy regime, i.e. $E_{\mathrm{CR}} < 10$ TeV, is explained very well, this statement does not hold for the high energy tail. The energy budget is heavily underestimated in this regime.
The comparison of both simulations is presented in Fig. 5.7. A combination of both simulations, for example as a broken power law, indicates the validity of this method and obtained spectrum in correspondence to the measurement data. The Kolmogorov-like diffusion coefficient fits very well as an explanation the cosmic ray flux. A stronger diffusion tends to a deficit in the energy.

Figure 5.8 shows the results of scenario B with the two chosen diffusion coefficients. The solid line represents the simulation for $E^{0.33}$ and the dashed line for $E^{0.5}$. Obviously, the latter is in better agreement with the data. The following two plots compare the results to scenario A. In Figure 5.9, the results are shown for a diffusion coefficient of $E^{0.33}$. Here, a better correspondence to the data is shown by scenario A. In the case of the quasi time-averaged spectrum, the simulation predicts a too high energy budget. The results for the diffusion coefficient of $E^{0.5}$ are shown in Figure 5.10. Here, the scenario B simulation is in very good agreement with the measurement, while the scenario A underestimates the data, especially in the high energy regime.

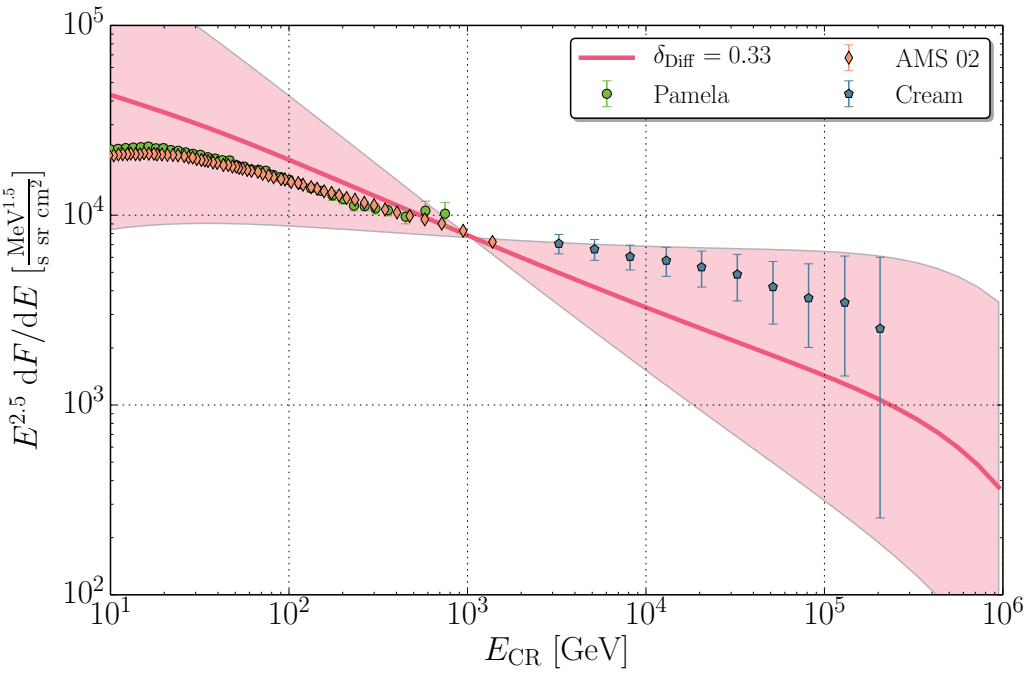

Figure 5.5: *This figure shows the flux of cosmic rays in the large Galaxy for 20,000 simulated SNRs. The spectrum of each remnant is randomly assigned by one of the available 21 SNRs in the set, see Tab. 5.1. In this simulation the diffusion coefficient is $D \propto E^{0.33}$. CREAM data taken from [162], PAMELA data taken from [163], AMS-02 data taken from [164]. Figure can be found in [59].*

5.2.3 Discussion of uncertainties

The uncertainties of this simulation play a major role and require a detailed discussion. This section, therefore, summarizes the most significant uncertainties.
With respect to the normalization, a crucial factor is the number of active supernova remnants that contribute to the spectrum with their ejection of particles. In this case, the number is assumed to be $N_{\mathrm{SNR}} = 100$. Of course, this number could be larger. As far as what is known, the number of radio emitting SNRs could be 300. For different populations, the average number can also vary. The assumption of using a rather low number finds reason for as only the brightest radio SNRs can accelerate particles to the highest energies.

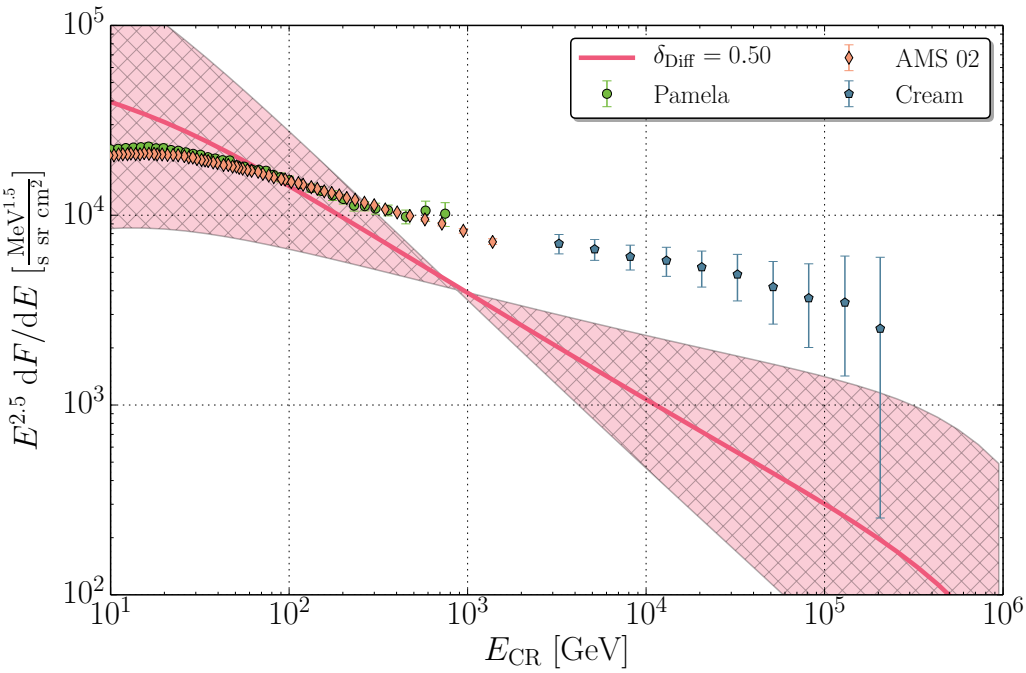

Figure 5.6: *This figure shows the flux of cosmic rays in the large Galaxy for 20,000 simulated SNRs. The spectrum of each remnant is randomly assigned by one of the available 21 SNRs in the set, see Tab. 5.1. In this simulation the diffusion coefficient is $D \propto E^{0.5}$. CREAM data taken from [162], PAMELA data taken from [163], AMS-02 data taken from [164]. Figure can be found in [59].*

Further, the criterion of a SNR with evidence of having a hadronic component in its spectrum has been used in this calculation. The authors of Ref. [40] extracted 21 SNR candidates out of 24 that can be fitted hadronically, however, there is the possibility that not every one of them is actually dominated by a π^0 decay.

Thirdly, the gamma-ray energy is between $\mathcal{O}(\mathrm{GeV}) \leq E_\gamma \leq \mathcal{O}(10\ \mathrm{TeV})$, corresponding to hadronic energies of $\mathcal{O}(10\ \mathrm{GeV}) \leq E_{\mathrm{CR}} \leq \mathcal{O}(100\ \mathrm{TeV})$. The low cosmic ray energy regime cannot be described with good precision and is also not the subject of this investigation. Since the *knee* energy is $E_{\mathrm{CR,knee}} \sim 1$ PeV, spectra with a lacking cutoff up to $E_{\mathrm{CR}} = 100$ TeV must be extrapolated.

Another important aspect concerns the statistical validity of the presented approaches. It is the result of this simulation to predict the average CR observable,

e.g. $\langle \mathrm{d}F/\mathrm{d}T \rangle$, but not the corresponding variance, e.g. Var($\langle \mathrm{d}F/\mathrm{d}T \rangle$). This measure, or an alternative statistical value describing the deviation, is required to derive a meaningful result with significant statistics. Due to the fact that the 21 SNRs used do not represent the full set of SNRs contributing to the high-energy spectrum, the variance would merely give an upper limit rather than the true variance. Future analyses following the same goals should update the method and thereby remove this uncertainty.

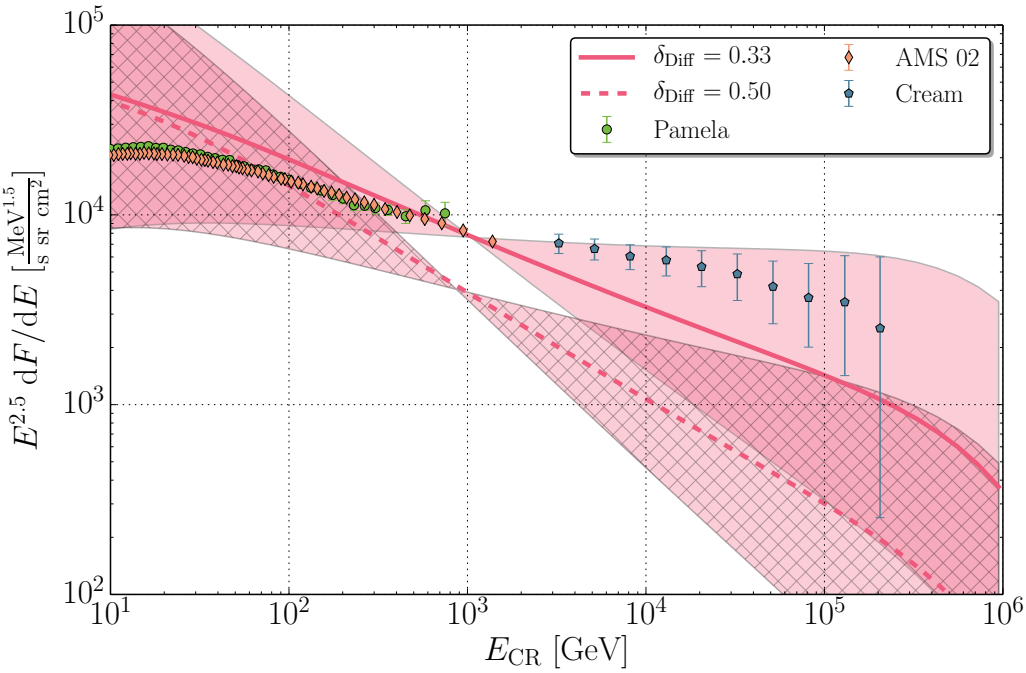

Figure 5.7: *This figure shows the flux of cosmic rays in the large Galaxy for 20,000 simulated SNRs. The spectrum of each remnant is randomly assigned by one of the available 21 SNRs in the set, see Tab. 5.1. In this simulation the diffusion coefficient is $D \propto E^{0.5}$. CREAM data taken from [162], PAMELA data taken from [163], AMS-02 data taken from [164]. Figure can be found in [59].*

Lastly, it must be said that it is not possible to derive the temporal evolution of one supernova remnant by the given snapshot in time. In this analysis, two approaches have been applied. Scenario A referred to SNRs in their phase where cosmic rays are dominantly ejected. Temporal effects must be neglected. On the contrary, in scenario B, a quasi time-averaged spectrum from the sample of individual remnants

has been produced. This implies that each source behaves equally.

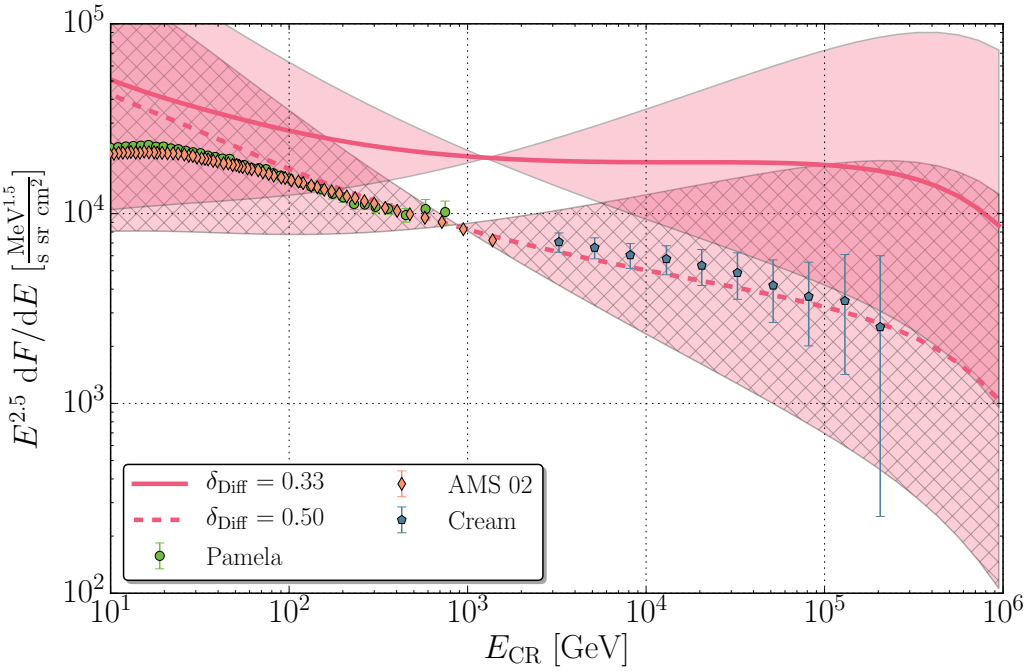

Figure 5.8: *This figure shows the flux of cosmic rays in the large Galaxy and in scenario (B). The solid line represents a diffusion of $D \propto E^{0.33}$ and the dashed line shows $D \propto E^{0.5}$. CREAM data taken from [162], PAMELA data taken from [163], AMS-02 data taken from [164]. Figure can be found in [59].*

Future experiments such as HAWC and CTA are expected to provide data allowing stronger conclusions with a particular focus on energies close to the *knee*. The current status of this analysis can only give an upper limit. The physical frame of uncertainties of the variables has been extended towards obtaining the most optimistic result. Most notably, all SNRs that can be fitted to a hadronic component have been assigned an energy cutoff at the *knee*, i.e. $E_{\mathrm{cutoff}} = 1$ PeV. For this reason, the results obtained can only be seen as an upper limit rather than a solid flux estimation.

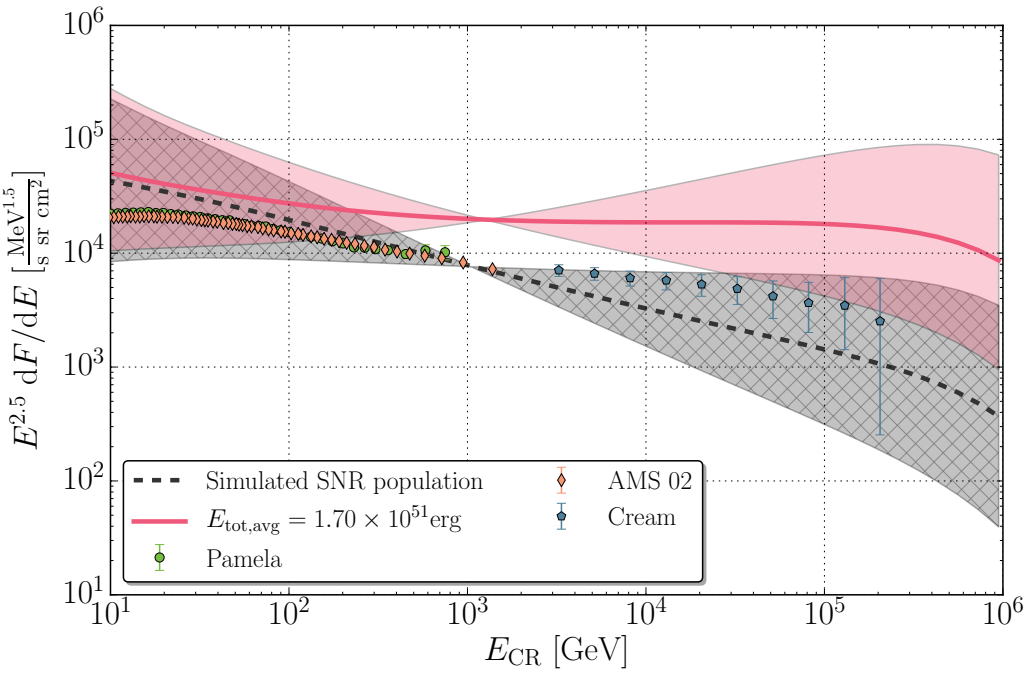

Figure 5.9: *This figure shows the flux of cosmic rays in the large Galaxy. The simulated flux follows a $D \propto E^{0.33}$ diffusion and shown are scenario (A) through the dashed and (B) through the solid line. CREAM data taken from [162], PAMELA data taken from [163], AMS-02 data taken from [164]. Figure can be found in [59].*

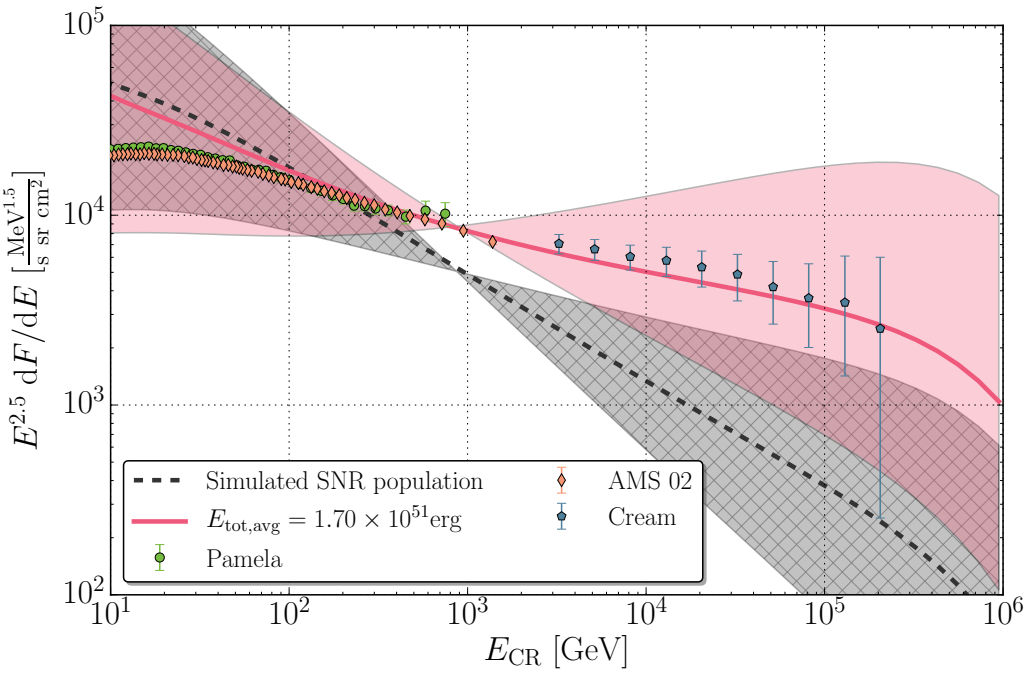

Figure 5.10: *This figure shows the flux of cosmic rays in the large Galaxy . The solid line shows a diffusion coefficient of $D \propto E^{0.33}$ and the dashed line a steeper diffusion of $D \propto E^{0.5}$. CREAM data taken from [162], PAMELA data taken from [163], AMS-02 data taken from [164]. Figure can be found in [59].*

5.3 Discussion & outlook

In this section, the results with respect to their validity are discussed, and an outlook is given for future analyses and the impact of upcoming data from new generation experiments.

5.3.1 Discussion

The goal of this simulation is to propagate cosmic rays originating from the source class of supernova remnants through the Galaxy towards Earth. A total number of $N_{\mathrm{SNR}} = 24$ have been analyzed on the basis of gamma-ray data, and their characteristic parameters have been published in Ref. [40]. It is required that a source may be fitted hadronically, and out of the 24 SNRs, 21 have been identified as such. Here, these remnants are used to investigate whether the cosmic ray energy budget

below the *knee* as measured on Earth can indeed be explained by the flux of SNRs. Given the high number of uncertainties and their non-negligible impact on the result, a detailed comparison of the measured spectrum to the presented simulation is not possible. However, the results show that SNRs may actually play a key role in explaining the spectrum up to $E_{\mathrm{CR}} \sim 1$ PeV.

The Kolmogorov-type diffusion describes the spectrum well within standard errors in scenario A, where a constant emission is simulated. Due to the fact that only a small fraction of sources detected in gamma-rays have a hadronic component, the entire spectrum cannot be solely explained by SNRs. If some SNRs, of which a cutoff is not apparent in their spectrum, actually do have an early cutoff, an explanation of the higher energy part in the spectrum is not justified.

A stronger diffusion, i.e. $\delta = 0.5$ as presented in this simulation, results in a very steep total spectrum and thus the high-energy component cannot be explained. That means that even by applying the most optimistic scenario, SNRs as the only candidates to explain the measured spectrum becomes a risky claim and must probably be extended by another source class.

As for the weak diffusion explaining the cosmic ray spectrum on Earth another feature contradicts this claim. The convection of cosmic rays out of the galactic disc carries an amount of energy that will not be evident in the spectrum detected on Earth and has been neglected thus far in the simulations. If these effects had been included, the resulting spectrum would have reported an even lower normalization, which means the required energy budget could not have been achieved. It is hereby indicated that in scenario A, convection is not significant in the transport of cosmic rays.

Scenario B achieves a higher energy budget and therefore, in the case of a Kolmogorov-type diffusion, convection of cosmic rays out of the Galaxy would help to reduce the energy budget and better match the measurement data. The diffusion coefficient of $E^{0.5}$ already agrees with the data very well. The consideration of convection would underestimate the data points, leaving room for sources contributing to the spectrum other than SNRs.

5.3.2 Outlook

In order to obtain an improved result, it is necessary to focus on a better understanding and quantification of the variance of the method. The quantification of the agreement between the predicted cosmic ray observables can be achieved by the measure of the variance. It could have been presented here along with the mean value, however, in the current simulation approach, it has a limited statistical interpretation. It only measures the spread of the simulated cosmic ray observable, which is induced by a random position selection in the Galaxy of the 21 SNRs, meaning the variance would actually decrease with an increasing number of sources. It can be stated that the variance of the 21 remnants gives an upper limit for the true one. New gamma-ray data available gives reason to hope for a more precise description of the cosmic ray spectrum at the source and therefore a better understanding of the variance. The true variance for this simulation accounts for temporal aspects of the SNRs, for example the production rate and lifetime. This could be achieved through a more sophisticated allocation of the SNRs' position to the closest grid point. An inhomogeneous grid would further enhance the quality of the simulation. In the GALPROP manual, a similar issue has already been addressed, see [51, 158].
In the long run, it would be desirable to use a Monte-Carlo (MC) simulation for the propagation of cosmic ray particles through the Galaxy, because it has significant advantages over the solution of the transport equation. There is already the MC-framework CRPropa [165] available to the public, but it is designed for extragalactic calculations. The version 3.0 of this code gives a promising perspective for extending the propagation for the Galaxy, e.g. [166], and CRPropa 3.1 extends the code to low energies. Also, the transport equation is solved by using stochastic differential equations [46]. Today's computer technologies allow for a MC simulation for galactic cosmic rays already for $E_{\mathrm{CR}} = 10$ TeV. Due to the time-consuming run times, it should be switched to a diffusive approximation for lower energies. There are two outstanding advantages compared to solving the transport equation:

- The trajectory of a single particle can be followed.
- All galactic field models can be implemented and tested. It is not necessary to assume a diffusion scalar, and the particles can be therefore transported through a realistic magnetic field. The comparison of different field models allows for a detailed study of the magnetic environments and the way they

affect the particle's path. It would also be possible to derive the diffusion tensor from this study.

Other effects concerning propagation could not be included in the current simulation. For example, local transport as the authors of [167–171] point out. The escape of cosmic rays from young remnants has been modelled time-dependently for different distances of the SNR in e.g. [171]. Apparently, the power-law approximation for escaping cosmic ray spectra applies only to old remnants. It has also been shown that the position of the molecular cloud influences the shape of the spectrum and that this does not exclusively represent the escaping cosmic ray spectrum. These local transport effects are interesting for further investigations, as they may become relevant when observing the average cosmic ray spectrum. However, in this simulation, it is expected to play a minor role due to the consideration of a randomized statistical sample.
The sample of 21 SNRs is still very small and this may be incomplete, which is naturally reflected in the obtained results. Due to the increased sensitivity of new experiments, such as CTA, a better spatial resolution of the source's position and an enlargement of the sample can be expected. This also helps to identify the the differential gamma-ray spectra, which provides information about the evolution of cosmic ray spectra with distance. With such a study, a comparison to one including local propagation effects can be made and conclusions about the influence on the average cosmic ray spectrum can be drawn.

CHAPTER 6

Simulating the Sun Shadow

This chapter presents the simulation of the cosmic ray Sun shadow. Cosmic ray particles with an energy distribution following the cosmic ray spectrum travel through space, and electromagnetic fields, dust clouds, and gas clouds influence their trajectory. The magnetic field of the Sun is of special interest due to its proximity to Earth. A variety of experiments measure the magnetic field directly or indirectly, see Chapter 4 for details. For example, the IceCube experiment uses the Moon shadow analysis in order to calibrate the detector in terms of reconstructing a particle's direction. An observer from Earth sees the Sun and the Moon as almost identical in size, thus, their shadows should be comparable. The Sun's magnetic field, however, deflects the cosmic rays such that detectors receive different images. Over an eleven-year cycle, the periodic change in the strength of the magnetic field can be observed.

The goal of this analysis is to use accessible magnetic field data, provided within the Potential Field Solar Surface model (PFSS), and to confirm the observed results with a simulation of cosmic ray particles of different energies.

6.1 Setup of the simulation

An easy way to calculate a physical system while using differential equations is to integrate the system numerically and to make all physical parameters dimensionless. This way, no confusions in units affect the results, and equation (2.4.1) can thus be rewritten in order to represent a dimensionless system[1] [47]

$$\frac{\mathrm{d}\hat{p}}{\mathrm{d}s} = \hat{E} + \frac{\hat{p} \times \hat{B}}{\gamma} \tag{6.1.1}$$

$$\frac{\mathrm{d}\hat{x}}{\mathrm{d}s} = \frac{\hat{p}}{\gamma}. \tag{6.1.2}$$

In the above equations, the parameter B_0 is a fiducial magnetic field strength and in the following is fixed to $B_0 = 1$ G, representing the magnitude of the mean solar magnetic field. The introduction of such a parameter allows for an entirely dimensionless system, and for protons, $q = e$ and $m = m_p$, the parameters are

$\hat{B} \equiv \frac{\vec{B}}{B_0}$	$\hat{E} \equiv \frac{\vec{E}}{B_0}$	$\omega_0 \equiv \frac{eB_0}{m_p c}$
$s \equiv \omega_0 t$	$r_0 \equiv \frac{c}{\omega_0}$	$\hat{x} \equiv \frac{\vec{x}}{r_0}$
$\hat{p} \equiv \frac{\vec{p}}{mc}$	$\gamma \equiv \frac{1}{\sqrt{1+\hat{p}^2}}$	$\hat{u} \equiv \frac{\hat{p}}{\gamma}$

Table 6.1: *All normalized parameters are denoted with hats. The parameter ω_0 is the fiducial proton gyrofrequency, and the time t is replaced by s. The fiducial gyroradius is r_0 and thus, the lengths $\hat{x}$ can be expressed in units of r_0. The particle's velocity $\hat{u}$ is also expressed by normalized parameters. The gyrofrequency $\hat{\omega}_g = 1/\gamma$ is dimensionless, as well. The parameters are adopted from [47].*

The relativistic equation of motion, Eq. (6.1.1), is solved by an adaptive Runge-Kutta algorithm, see Subsection 2.4.4 for details about the calculation. Tests that probe the stability, convergence, and accuracy of this method can be found in [47]. The accumulation of numerical errors are avoided by applying a random pitch angle scattering.

[1] Please note that the charge is included in the differential ds, see Table 6.1.

6.2 Test of simulations

Before performing the final simulation, a few cross-check tests have been performed to validate the propagation code. After the introduction into the theoretical basics of the propagation code, this section will present preliminary tests to the reader.

6.2.1 Homogeneous field

The test of the homogeneous field is valuable due to the rather easy theoretical calculation. A relativistic proton enters a homogeneous field, and its gyroradius can be determined through

$$E = \gamma m_p c^2, \tag{6.2.1}$$

with $\gamma = (1 - u^2/c^2)^{-1/2}$, m_p the rest mass of the proton and c the speed of light. The gyroradius is

$$r_G(E) = \frac{E}{eBc}, \tag{6.2.2}$$

with e as the electric charge of the proton and B the magnetic field strength. Figure 6.1 shows the result for three different energies, $E_{p,1} = 5$ TeV, $E_{p,2} = 10$ TeV, and $E_{p,3} = 15$ TeV. The magnetic field is $\vec{B} = 1\vec{e}_y$ G. The Sun has been included for visual purposes. Table 6.2 lists all gryroradii and the deviation from the theoretically calculated value.

	$E_{p,1} = 5$ TeV	$E_{p,2} = 10$ TeV	$E_{p,3} = 15$ TeV
$r_G(E)$ [m]	$1.6 \cdot 10^8$	$3.1 \cdot 10^8$	$4.7 \cdot 10^8$
$1 - \frac{r_G(E)}{r_{G,\mathrm{sim}}(E)}$	$2.6 \cdot 10^{-5}$	$1.8 \cdot 10^{-5}$	$1.5 \cdot 10^{-5}$

Table 6.2: *The gyroradii are listed for three different energies in a $\vec{B} = 1\vec{e}_y$ G magnetic field. The deviation from the theoretical value is also given.*

In order to test the stability of the simulation, the different particle positions are tested in addition to different energies. The small error for the gyroradii of each trajectory as presented in Table 6.2, shows the high accuracy of the simulation.

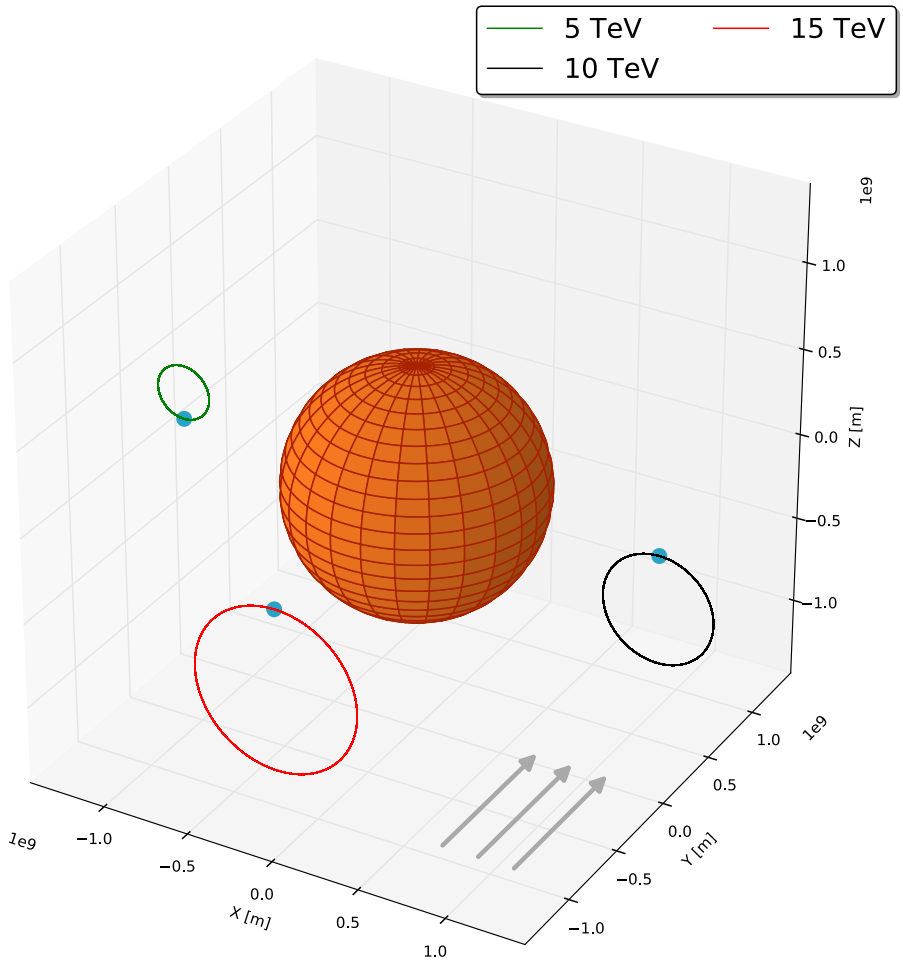

Figure 6.1: *Test particles injected with the energies $E_{p,1} = 5$ TeV, $E_{p,2} = 10$ TeV, and $E_{p,3} = 15$ TeV with momentum in the negative x-direction with a magnetic field in y-direction. The blue dots indicate the starting points.*

6.2.2 The ideal dipole field

After the test of a homogeneous magnetic field, a axisymmetric field will be investigated. For this purpose, an ideal dipole is used for the simulation.

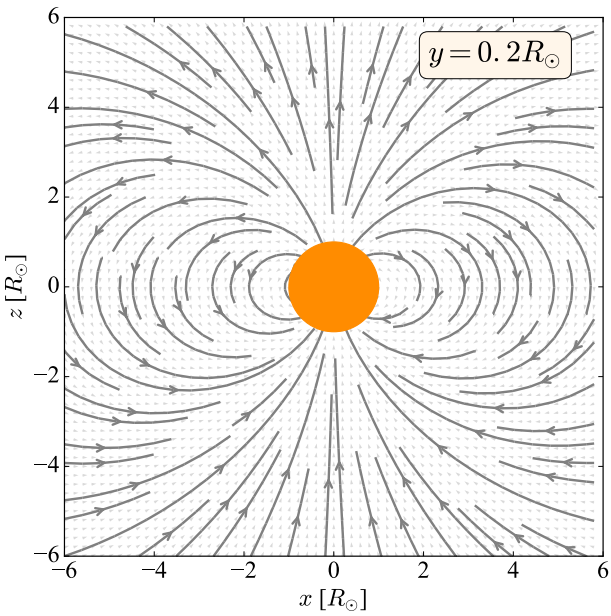

Figure 6.2: *Figure shows magnetic field lines of an ideal dipole magnetic field.*

About every 11 years, the photospheric dipole of the Sun reverses its magnetic orientation. The dipole depends on the solar activity, see e.g. [172]. In the following, the effect of an ideal magnetic dipole field is tested. Figure 6.2 shows the magnetic field lines of a dipole; the decreasing strength of the magnetic field with distance is not shown. The symmetry axis is the z-axis.

The dipole can be defined in a spherical coordinate system. Further, it is defined with $r > r_0$, where r is the distance from the origin of the coordinate system. Using B_0 as the magnetic field strength at the pole, one representation of a magnetic dipole field is described by the following equation

$$\vec{B}(r, \vartheta, \varphi) = B_0 \frac{r_0^3}{r^3} \left[\cos(\vartheta)\vec{e}_r + \frac{1}{2}\sin(\vartheta)\vec{e}_\phi \right]. \tag{6.2.3}$$

In Fig. 6.3, particles propagate through a magnetic dipole field with strength $B_0 = 2$ G, see Eq. (6.2.3). The particles are injected in the equatorial plane of the dipole and pass by the solar surface at a low distance. The higher-energetic ones pass by the Sun, however, they experience a deflection. Low-energy particles suffer a stronger deflection and hit the solar surface.

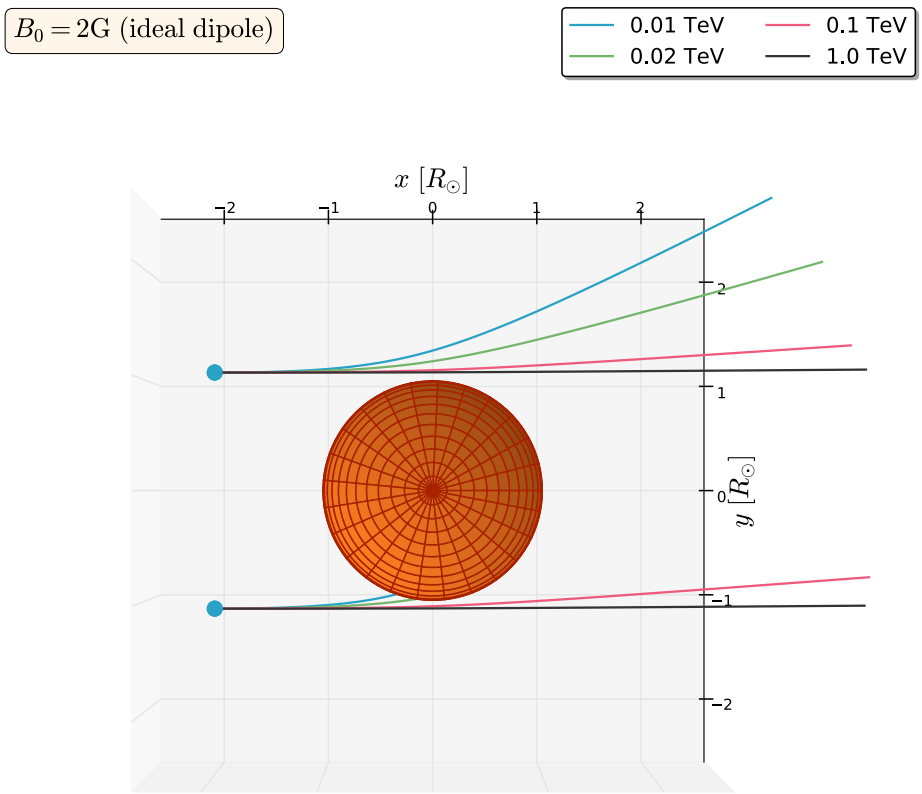

Figure 6.3: *Figure shows the Sun and particles that propagate through a dipole field in the equatorial plane at $z = 0R_\odot$. The blue points indicate the starting positions and the trajectories of particles are shown with solid lines. Those hitting the solar surface are not propagated further.*

In Fig. 6.4, particles are propagated close to the pole of the dipole. In a qualitative comparison to Fig. 6.3, the particles are exposed to a stronger magnetic field and are thus stronger deflected. Also, the orientation of the magnetic field is the opposite, and the particles are deflected accordingly.

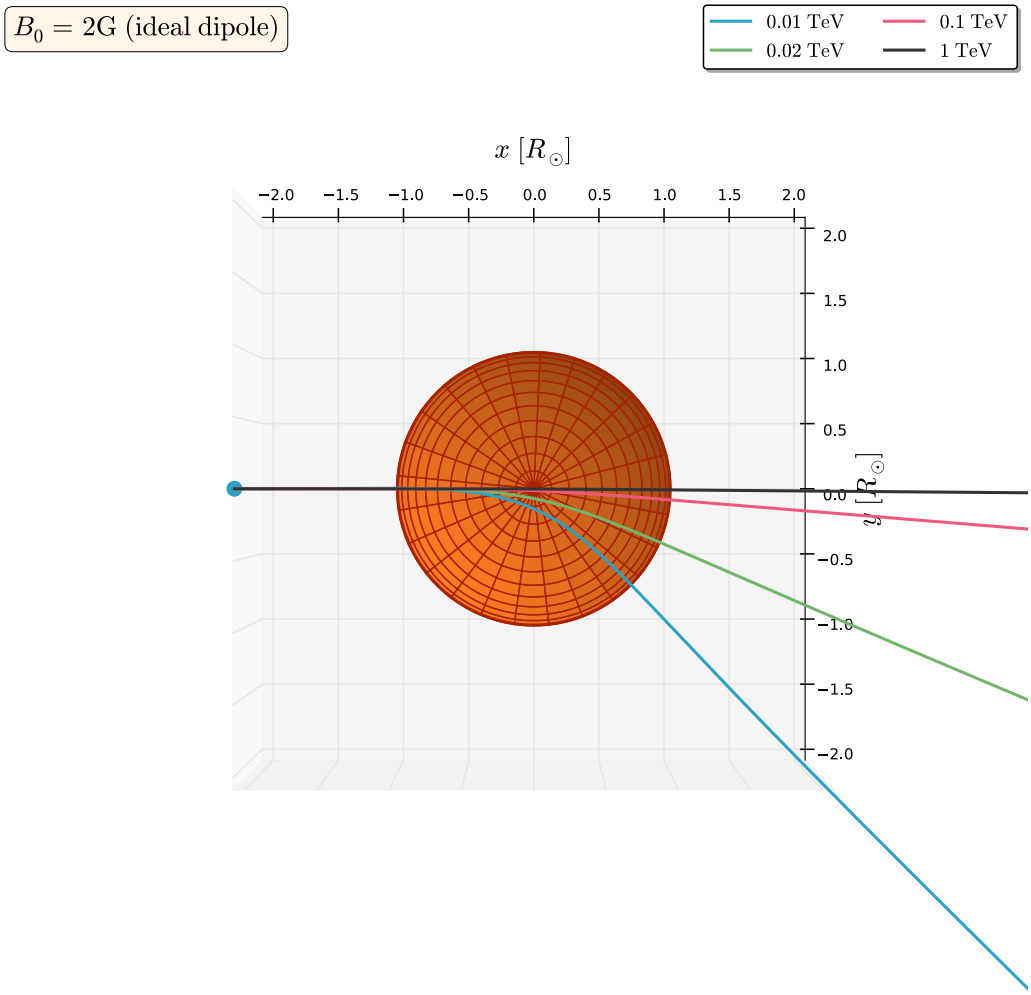

Figure 6.4: *Figure shows the Sun and particles that propagate through a dipole field close to the pole area. The blue point indicates the starting point, and the trajectories of particles are shown with solid lines.*

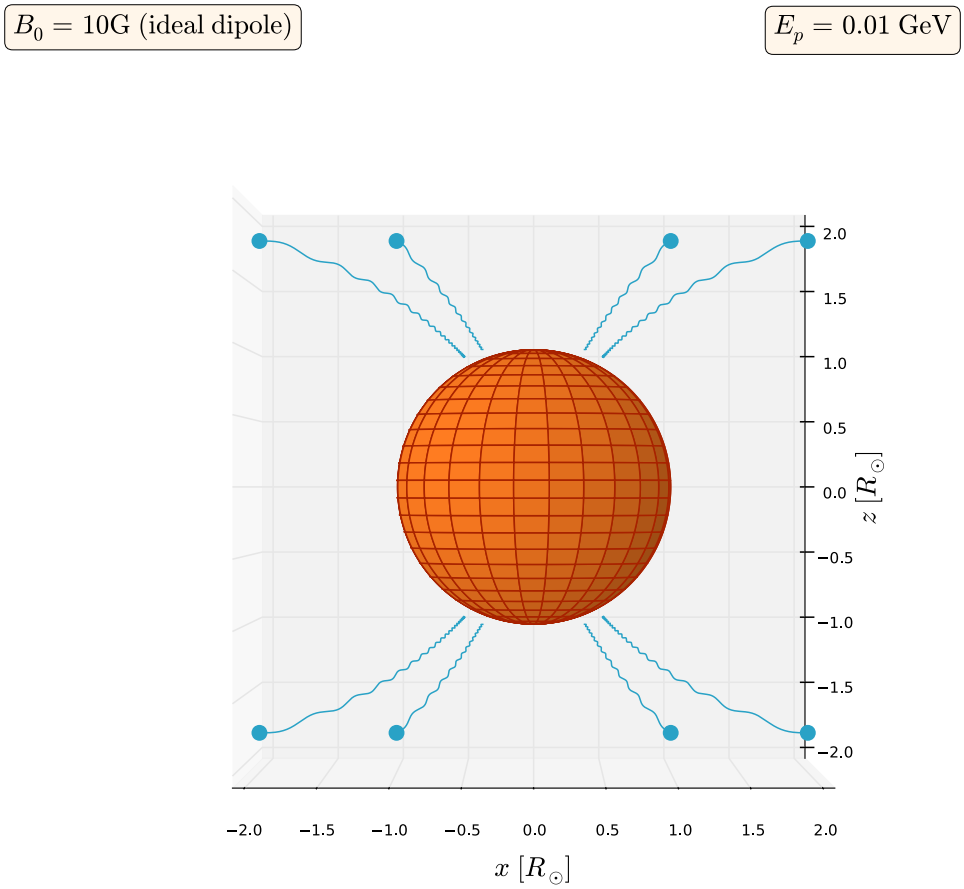

Figure 6.5: *Test particles of $E = 0.01$ GeV are injected into a strong magnetic dipole field in order to investigate their behavior in such. It can be seen that they follow the magnetic field lines, and their gyroradius, i.e. amplitude of the trajectory respective to the field line, decreases as they approach the surface of the Sun, although the effect is rather small.*

In a third test of the ideal magnetic dipole field, it is investigated whether low energy particles follow the magnetic field lines. Figure 6.5 shows different starting points of test particles following the magnetic field lines quite accurately. Also, the decrease of the gyroradius while approaching the solar surface is evident, although not quantified here.

6.3 Description of the method

After the tests, as presented in the previous section, a whole set of particles can be simulated. The method used to simulate the Sun shadow will be presented in this section.

All particles of one simulation have the same energy and direction of initial momentum. They only differ in their starting position. Technically, the protons are simulated backwards in time. The advantage of this method is that all momentum vectors are parallel oriented and toward the observer such that all simulated particles can be used. Figure 6.6 demonstrates the arrangement of simulated particles and shows their trajectories color coded with time. The starting points are arranged in a plane, which will be referred to as the *injection plane* in the following.

Particles that have hit the solar surface will be marked and not be considered in further calculations. The missing starting points in the injection plane in Fig. 6.6 indicate those particles.

6.3.1 Advantages and disadvantages

The magnetic field data cannot reproduce what is behind the Sun from the viewpoint of Earth. The data, however, is averaged over a whole month, which is approximately the time of one Carrington rotation[2]. By assuming that the magnetic field has not changed dramatically over this time, the rotation of the injection plane of the simulated particles allows to obtain information about the magnetic field in the respective month. Therefore, by rotating the injection plane around the z-axis of the Sun 36 times by ten degrees, an averaged picture of the Sun shadow can be obtained.

One disadvantage is that no statistical uncertainties can be presented. Each trajectory is calculated individually and interactions among the particles are neglected.

[2]One Carrington rotation is 27.2753 days, see e.g. [109]

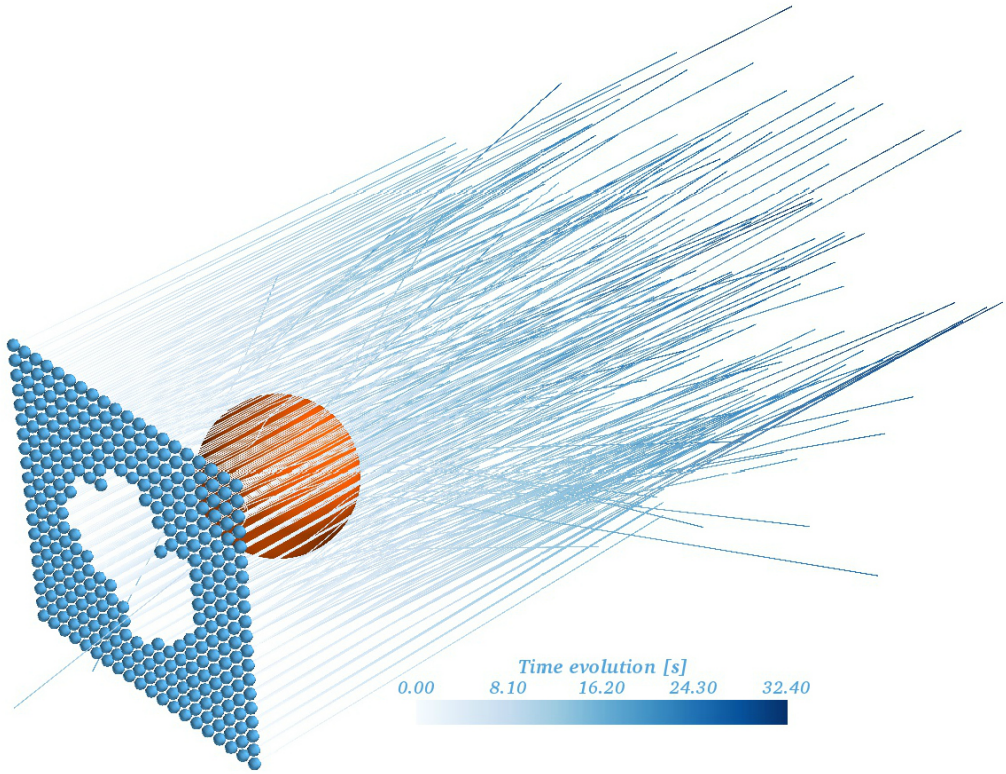

Figure 6.6: *Figure illustrates the basic approach to how the Sun shadow is simulated. The particles are injected with starting points arranged on a plane. This plane will rotate around the Sun's z-axis 36 times, so that an image is created every ten degrees simulating the daily rotation of the Sun, assuming that the field configuration is steady over the period of one month. The particles in this Figure have an energy of* $E = 40$ *TeV, and the magnetic field was chosen to be from December 2015.*

6.4 Study of the solar magnetic field

In this section, characteristics of the Sun's magnetic field are shown for the time period in which the cosmic ray shadow is simulated. Firstly, an overview of the Sun spot number is given for the ten years analyzed, 2007 through 2017, which is related to the magnetic flux, see Fig. 4.1. Further it is described, how the field is obtained and included in the simulation. Lastly, the field is investigated for December 2015, for which the field strength and the field's orientation is shown at several distances from the solar surface.

6.4.1 Solar activity

The Sun spot number for the time period of ten years is shown in Fig. 6.7. The amplitude of the Sun spot number is rather small compared to the previous cycle. It has been noted earlier that this number underlies a temporal modulation, see Chapter 4 for further details.
Figure 6.7 further shows the months November, December, January, and February of each year highlighted in order to visualize the data that is used for the simulation.

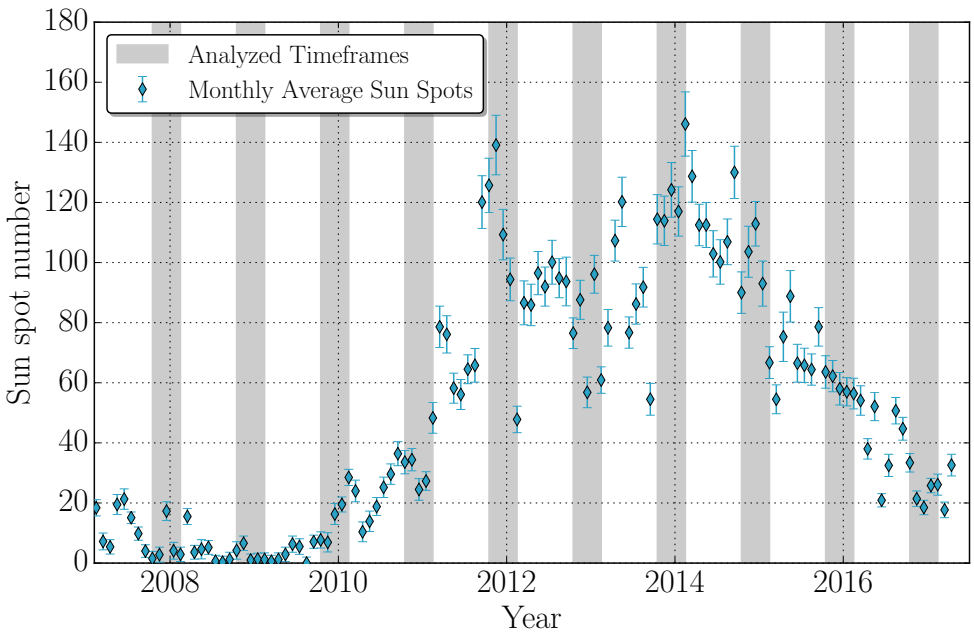

Figure 6.7: *Figure shows the Sun spot number for the timeframe under investigation. The grey regions indicate the months November through February. Data taken from [173].*

The years 2008 through 2010 show a minimum of the Sun spot number, and consequently the magnetic field strength is expected to be low as well. In subsequent years an increased solar activity is apparent.

In the following, the two-dimensional simulation results, as shown in Figs. 6.10 - 6.12, are quantified with respect to the relative deficit and the averaged total absorption.

6.4.2 Including the magnetic field in the simulation

In this study, the magnetic field is obtained from integral synoptic magnetograms provided by the Global Oscillation Network Group (GONG) [112]. The publicly accessible code FDIPS [121] interprets these magnetograms within the Potential Field Source Surface model (PFSS). The Laplace equation (4.4.3) is solved with an iterative finite difference approach.

The result of the FDIPS routine is an ASCII table with field parameters filled in columns. The individual columns are *radius, longitude, co-latitude*, B_R, B_φ, and B_ϑ.

By using this code, numerical artefacts, such as the ringing effect, which is similar to Gibb's phenomenon, are avoided [121]. The accuracy at which the magnetic field should be read out can be defined by the user. The configuration as presented in the following sections uses the following limits:

- **Radius** r: $1R_\odot \leq r \leq 2.5R_\odot$, number of steps: $N_r = 150$
- **Longitude** φ : $0 \leq \varphi \leq 2\pi$, number of steps: $N_\varphi = 360$
- **Co-Latidude** ϑ : $-\pi/2 \leq \vartheta \leq \pi/2$, number of steps: $N_\vartheta = 180$.

The choice of step sizes of the parameters reflects the resolution of magnetograms [174]. FDIPS evaluates the magnetogram and returns a representation of the field on a spherical grid. In the simulation presented, the nearest neighbor is determined on this regular grid and eventually the field is translated to a cartesian grid. This way, Eqs. (6.1.1) and (6.1.2) are applicable.

6.4.3 The magnetic field of December 2015

The magnetic field from December 2015 can be seen in Fig. 6.8 along with simulated trajectories. The plot shows the magnetic field strength of two radii on a linear scale. This way, it also contains information about the orientation of the field.

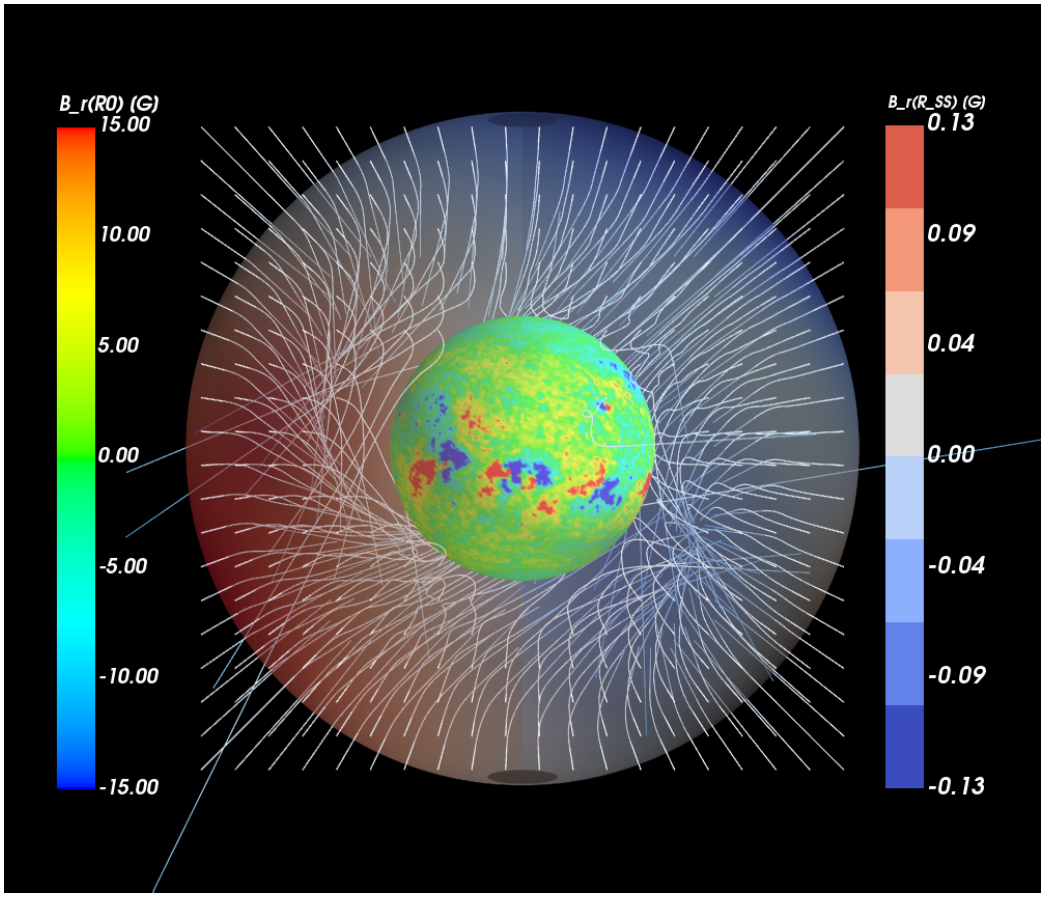

Figure 6.8: *Figure shows the magnetic field strength of the B_r-component color coded for two different radii, namely right at the solar surface, $B_r(R_0 = R_\odot)$, and at the source surface $B_r(R_{SS} = 2.5R_\odot)$. Also shown are the trajectories simulated.*

It can be seen that close to the solar surface at $r = R_\odot$ the field is highly structured and magnetic reconnections can be identified in the region of the equator. It must be said that due to the high magnetic field strengths the color scale must be limited to a strength of $B = |15|$ G in order to highlight weaker regions. Thus, higher field strengths exist especially in red and blue spots.

Farther outside, at $r = 2.5R_\odot$, the field strength has decreased drastically and is only of a fraction of the very close field. Also the structure of the field has altered and the field is less turbulent and shows rather a dipole-like structure.

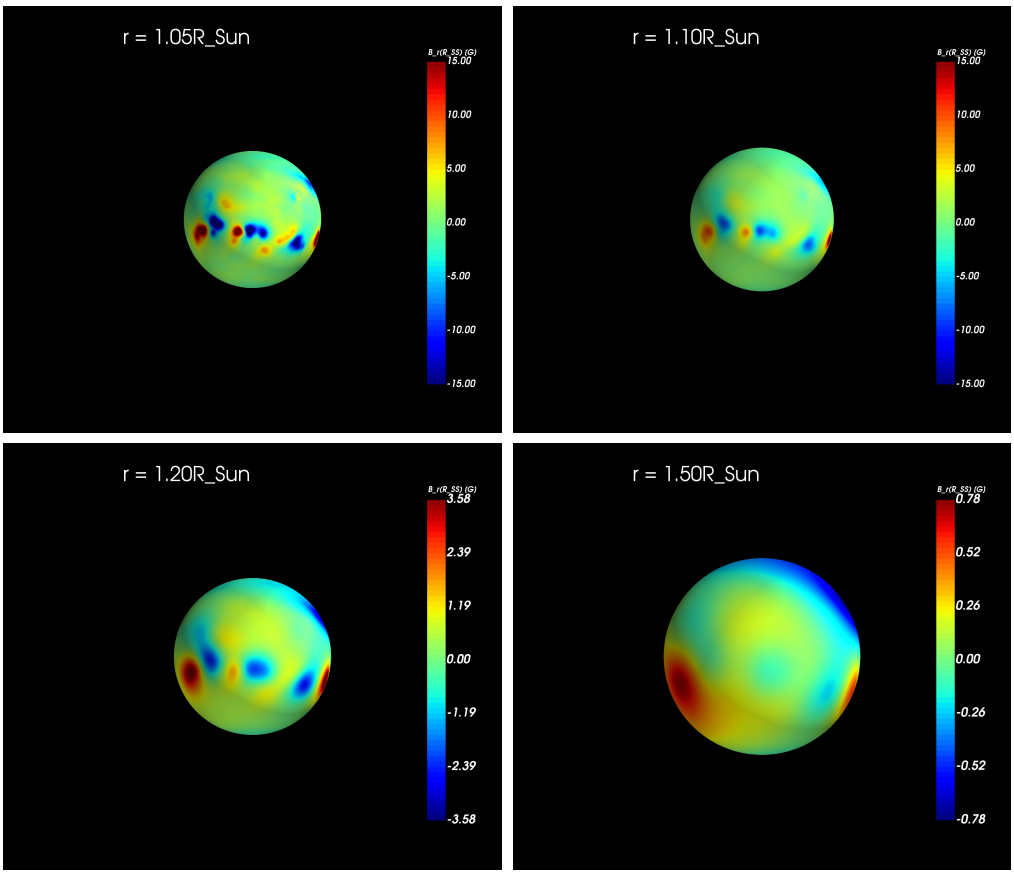

Figure 6.9: *Figure shows the development of the magnetic field structure at different distances from the solar surface. The color scale of the magnetic field strength is limited to* $|15|$ *Gauss when greater strengths are present.*

A more detailed picture of the magnetic field structure can be seen in Fig. 6.9 where the B_r-component is shown for different radii. It can be seen that with increasing distance the strength decreases and local strong fields vanish. A large-scale structure develops toward a dipole structure with $B_r(r \gtrsim 1.5R_\odot) < 1$ G on the entire shell.

6.5 Simulation of the solar cosmic ray shadow

In this section the cosmic ray shadow caused by the Sun is presented. The result for the magnetic field averaged over a month and its effect on trajectories of cosmic rays with different energies is shown. For the obtained images, the average relative

deficit and averaged total absorption are calculated, which both are a measure for the absorption of cosmic rays by the Sun.

6.5.1 The cosmic ray Sun shadow

The result of the cosmic ray Sun shadow at cosmic ray energies $E_{CR} = 10$ TeV, $E_{CR} = 40$ TeV, and $E_{CR} = 100$ TeV, can be seen in Figures 6.10 through 6.12, respectively. In each Figure, the results for the magnetic fields from December from the years 2007 through 2016 are presented at different energies. The months November from 2007 through 2017, as well as January and February, both from 2008 through 2017, are attached in the Appendix 7.2.

The maps in Figures 6.10 through 6.12 show the heads-on view from the direction of the injection plane, in a window of $-2\ R_\odot \leq (y, z) \leq +2\ R_\odot$, with a rotating solar magnetic field. The limits of y and z are chosen such that strongest deflections of the trajectories are still visible. The geometrical size and position of the Sun is indicated with a black circle. The color code shows the averaged probability of a particle to pass through, P_{pass}, and not be absorbed by the Sun, and can be defined as

$$P_{\text{pass}} := 1 - P_{\text{hit}}, \tag{6.5.1}$$

with P_{hit} as the fraction of the $n_a = 36$ rotation angles in each bin. The lowest energy, $E_{CR} = 10$ TeV, shows the most drastic deviation from the size of the Sun. Here, the features of the magnetic field have the greatest effect on the particles. The variation of the magnetic field over time is clearly visible and is quantified in the following sections.

Qualitatively, it can be said that in times of a solar minimum, see Fig. 6.10, i.e. in the years 2007 through 2009, the cosmic ray shadow does not change significantly, in contrast to a higher solar activity, for example in the year 2011.
These effects are less strong for $E_{\text{CR}} = 40$ TeV, however, the large scale features that are seen at $E_{\text{CR}} = 10$ TeV are still present. In the case of the highest simulated energy, $E_{\text{CR}} = 100$ TeV, the magnetic field has only a tiny effect on a cosmic ray trajectory.

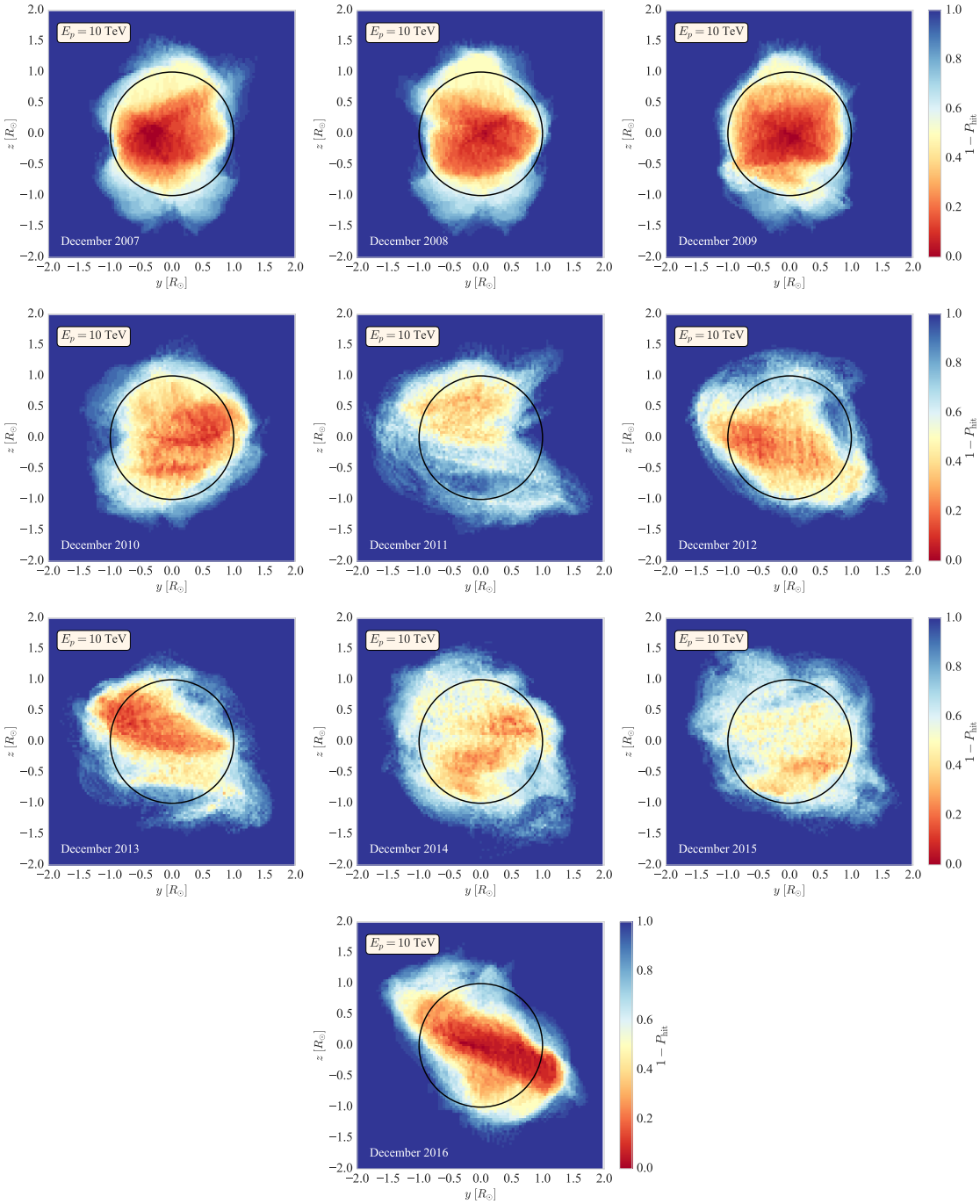

Figure 6.10: *Figure shows the variation of the cosmic ray Sun shadow over time at $E_{CR} = 10$ TeV from 2007 through 2016 in December.*

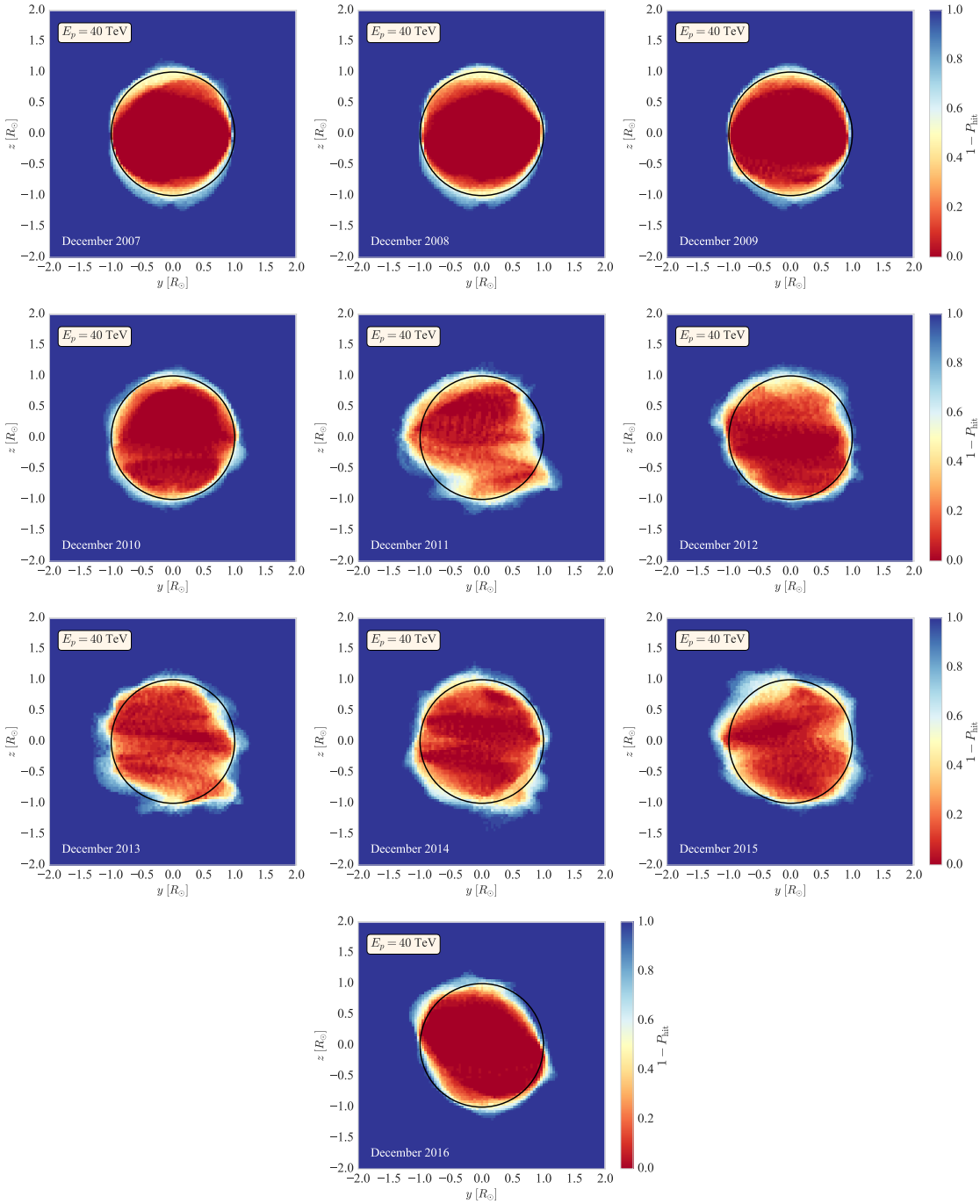

Figure 6.11: *Figure shows the variation of the cosmic ray Sun shadow over time at $E_{CR} = 40$ TeV from 2007 through 2016 in December.*

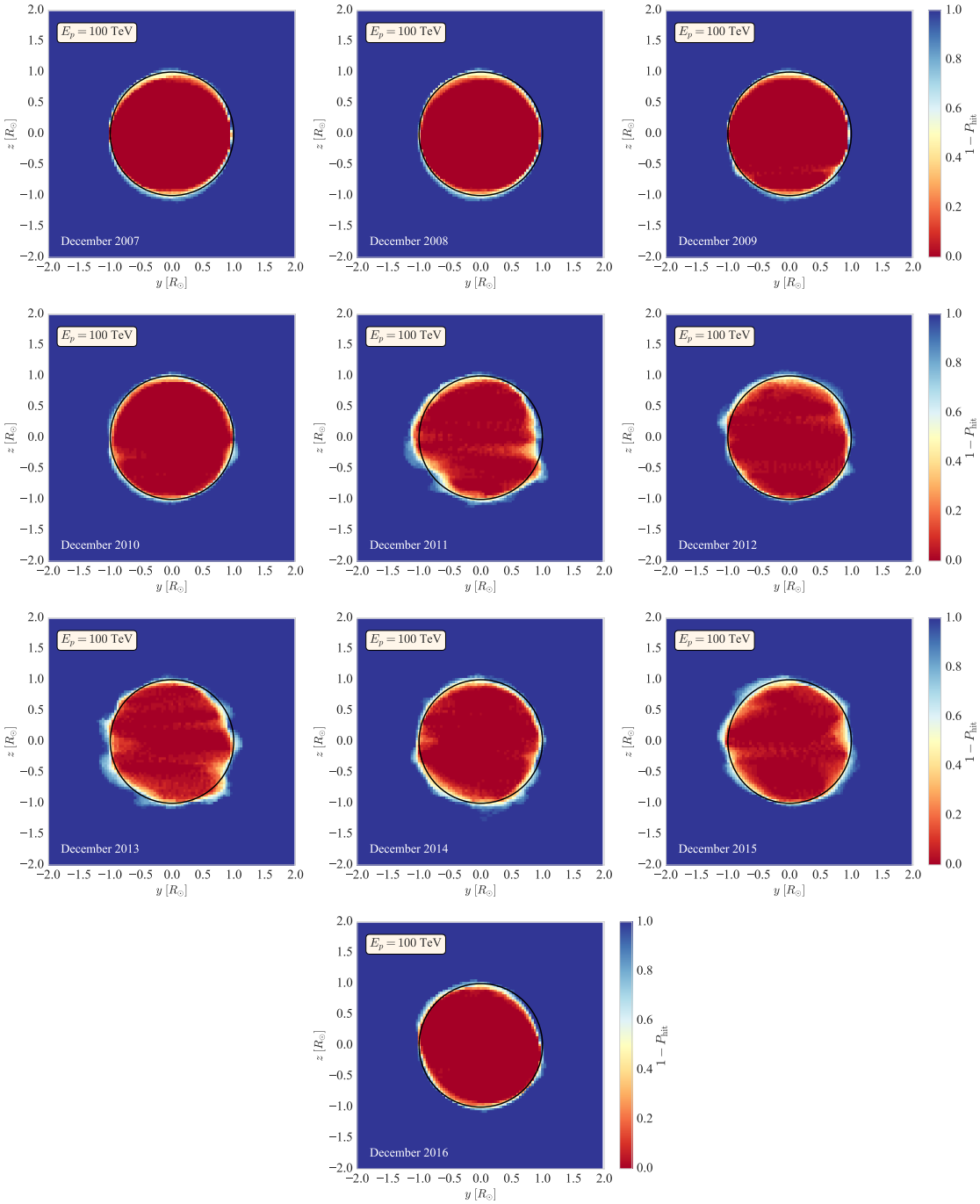

Figure 6.12: *Figure shows the variation of the cosmic ray Sun shadow over time at $E_{CR} = 100$ TeV from 2007 through 2016 in December.*

6.5.2 Averaged relative deficit

The averaged relative deficit, $\bar{\eta}^{2\mathrm{D}}$, from November through February can be seen in Fig. 6.13. In order to quantify the deficit in each map, a few parameters must be introduced. First, the bin width of the map in units of the radius of the Sun is $d = R_\odot/25$, where 25 bins cover the size of the radius of the Sun. Therefore, the area covered by one bin is

$$A_\square = \left(\frac{R_\odot}{25}\right)^2 = d^2, \tag{6.5.2}$$

in the unit $[A_\square] = [R_\odot^2]$. The area of the disk of the Sun in units of $A_\square$ is therefore

$$A'_\odot = \frac{A_\odot}{A_\square} = \frac{\pi R_\odot^2}{d^2}. \tag{6.5.3}$$

All hits are counted that have been injected inside the projected area of the disk of the Sun on the injection plane. The distance of the bin center from the center of the Sun can be defined by

$$r_{ij} = d \cdot \sqrt{i^2 + j^2}, \tag{6.5.4}$$

with $i, j \in [-50, 50]$. Far away from a source, the probability for particles to pass is $P^0_{\mathrm{pass}} \equiv 1$. The relative deficit can be determined and is for each month

$$\eta^{2\mathrm{D}} = \frac{1}{A'_\odot} \sum_{k=1}^{n_t} \frac{P_{k,\mathrm{pass}} - P^0_{\mathrm{pass}}}{P^0_{\mathrm{pass}}} = \frac{-1}{A'_\odot} \sum_{k=1}^{n_t} P_{k,\mathrm{hit}}, \quad \text{for } r_{ij} < R_\odot, \tag{6.5.5}$$

with the hit probability $P_{k,\mathrm{hit}} = n_{k,\mathrm{hit}}/n_a$ and n_a the number of angles, i.e. number of rotations of the injection plane around the Sun, $n_{k,\mathrm{hit}}$ the number of hits, and n_t the total number of trajectories simulated. The averaged relative deficit is the sum of $\eta^{2\mathrm{D}}$ and normalized by the number of months, thus

$$\bar{\eta}^{2\mathrm{D}} = \frac{\sum_{k=1}^{4} \eta_k^{2\mathrm{D}}}{4}. \tag{6.5.6}$$

The result is independent from the actual size of the injection plane because it is normalized to the area of the disk of the Sun.

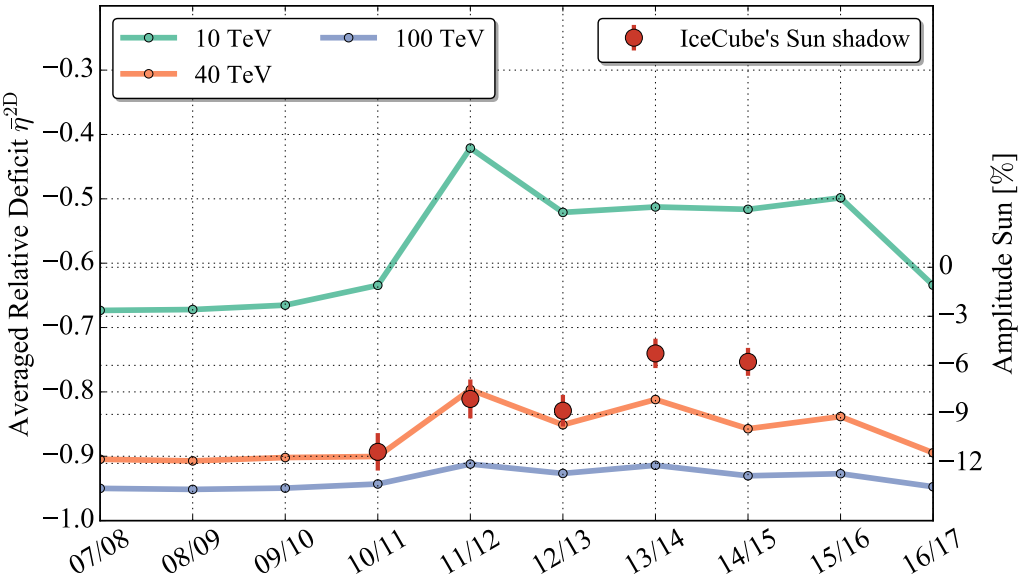

Figure 6.13: *Figure shows the averaged relative deficit in the season from November through February over ten years. The data points show the amplitude of the fitted Gaussian in IceCube's one dimensional Sun shadow analysis, however the different scales on the y-axes are not comparable. Data taken from [131].*

The result can be related to (a) the Sun spot number and (b) to the Sun shadow analysis that has been performed using data from IceCube. With regards to (a) it can be said, that the averaged relative deficit does not change significantly in the years 2008 through 2010, where the Sun has reached a minimum of activity. All simulated energies, from the lowest, $E_{\mathrm{CR}} = 10$ TeV, to the highest, $E_{\mathrm{CR}} = 100$ TeV, show an almost unchanged behavior in the averaged relative deficit. As the magnetic field strength increases, the averaged relative deficit increases, as well, which means that fewer particles with end points within the geometrical extensions of the Sun exist. Therefore, a stronger magnetic field deflects particles, and the cosmic ray Sun shadow is smeared out and more shallow.
For (b), the simulation of the Sun shadow using magnetic field data is good agreement with the Sun shadow that is measured with the IceCube detector. Although at this stage, a numeric comparison is not applicable, both analyses show a similar slope. This can be seen as a first indicator that data and simulation complement

each other. Further investigation are needed, and the simulation result must include detector specific parameters, such as the point-spread function in order draw further conclusions.
The discrepancy between the simulation results and the data can have several reasons. The IceCube detector does not detect cosmic rays mono-energetic, whereas the simulation does only include particles of the same energy. Another reason may be the composition of cosmic rays. Particles with a higher atomic number experience a different deflection caused by the magnetic field. A variating magnetic field leads therefore to a change in composition of particles detected from the direction of the Sun. Additionally, effects of the Earth's atmosphere and inside the detector are not included in the simulation.

6.5.3 Averaged total absorption

The fraction of absorbed and passed-through particles averaged over the months from November through February can be seen in Fig. 6.14. with i representing the months, and β_i the monthly total absorption. The individual results are attached in the Appendix, see Fig. 10. The monthly total absorption is

$$\beta_i = \frac{1}{n_t} \sum_{i=1}^{n_t} P_{i,\mathrm{hit}}, \tag{6.5.7}$$

with $P_{i,\mathrm{hit}} = n_{i,\mathrm{hit}}/n_a$ as the hit probability of each bin, $n_{i,\mathrm{hit}}$ as the number of hits and n_t as the number of simulated trajectories. This observable is thus anti-proportional to the actual size of the injection plane. Therefore, it is specified to the presented simulation results. The value of each data point in Fig. 6.14 is somewhat arbitrary. The shape, however, would not change with a varied range of the two-dimensional image. The seasonal averaged total absorption is determined by

$$\bar{\beta} = \frac{\sum_{i=1}^{4} \beta_i}{4}. \tag{6.5.8}$$

Like the averaged relative deficit, the first three simulated years, 2008 through 2010, show a constant value. With an increased magnetic field strength, the total

absorption decreases, and therefore fewer particles actually hit the Sun. Therefore, this quantity can also be used for a measure of the strength of the magnetic field.

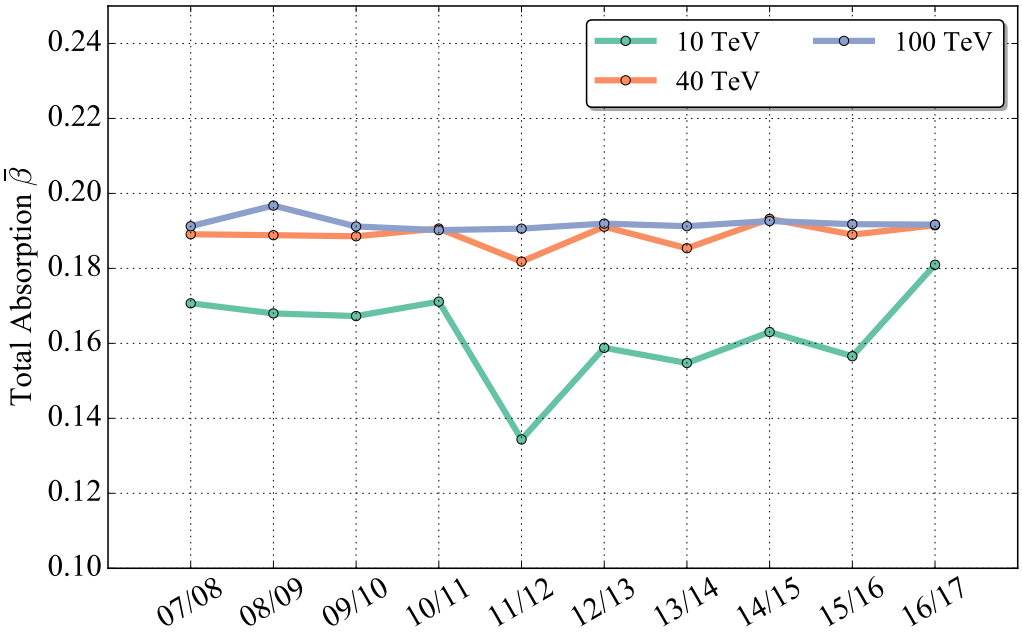

Figure 6.14: *Figure shows the averaged total absorption in the season from November through February over ten years, normalized by the total number of simulated particles.*

6.6 One-dimensional analysis of the shadow

The one-dimensional analysis of the cosmic ray Sun shadow gives a measure of the shadow depth of the Sun. In Fig. 6.15, the one-dimensional results are averaged over each season from November through February. A more detailed view on the monthly shadow depth is attached in the Appendix, see Figs. 12 - 15.

In this analysis, all simulated hits are counted for each bin. A bin, $j \in \mathbb{N}$, is defined concentric around the center of the Sun. The maximum radius is $r_{\max} = 2R_{\odot}$ and the constant bin width, r_0 is defined by the number of bins n_{bins}, such that $r_0 = r_{\max}/n_{\text{bins}}$. The number of bins cannot be chosen infinitely large due to the finite number of simulated cosmic rays. In the following the bin number is $n_{\text{bins}} = 12$. In analogy to the two-dimensional analysis, the area covered by a bin, A_j, is

$$A_j = \pi \left[(j \cdot r_0)^2 - ((j-1) \cdot r_0)^2 \right], \text{for } j > 0, \tag{6.6.1}$$

and can be expressed in units of $A_\square$,

$$A'_j = \frac{A_j}{A_\square}. \tag{6.6.2}$$

Using $n_{j,\text{pass}}$ as the number of passed through particles, the relative deficit in the one-dimensional analysis is then obtained by

$$\eta_j^{1\text{D}} = \frac{n_{j\text{pass}}}{A'_j \cdot n_a}, \tag{6.6.3}$$

with n_a as the number of angles. Figure 6.15 compares the three different energies simulated for the relative deficit averaged over four months,

$$\bar{\eta}^{1\text{D}} = \frac{\sum_{i=1}^{4} \eta_i^{1\text{D}}}{4}. \tag{6.6.4}$$

The relative deficit for each month is presented in the Appendix. In the case of $E_{\text{CR}} = 10$ TeV, the largest deviation from the theoretical value, which is indicated by the red line in the shape of a step function, is apparent. In every bin, the highest energy has the shortest distance to the theoretical value. As a measure for this claim, the integral has been determined for the area of the Sun and is presented in the following subsection.

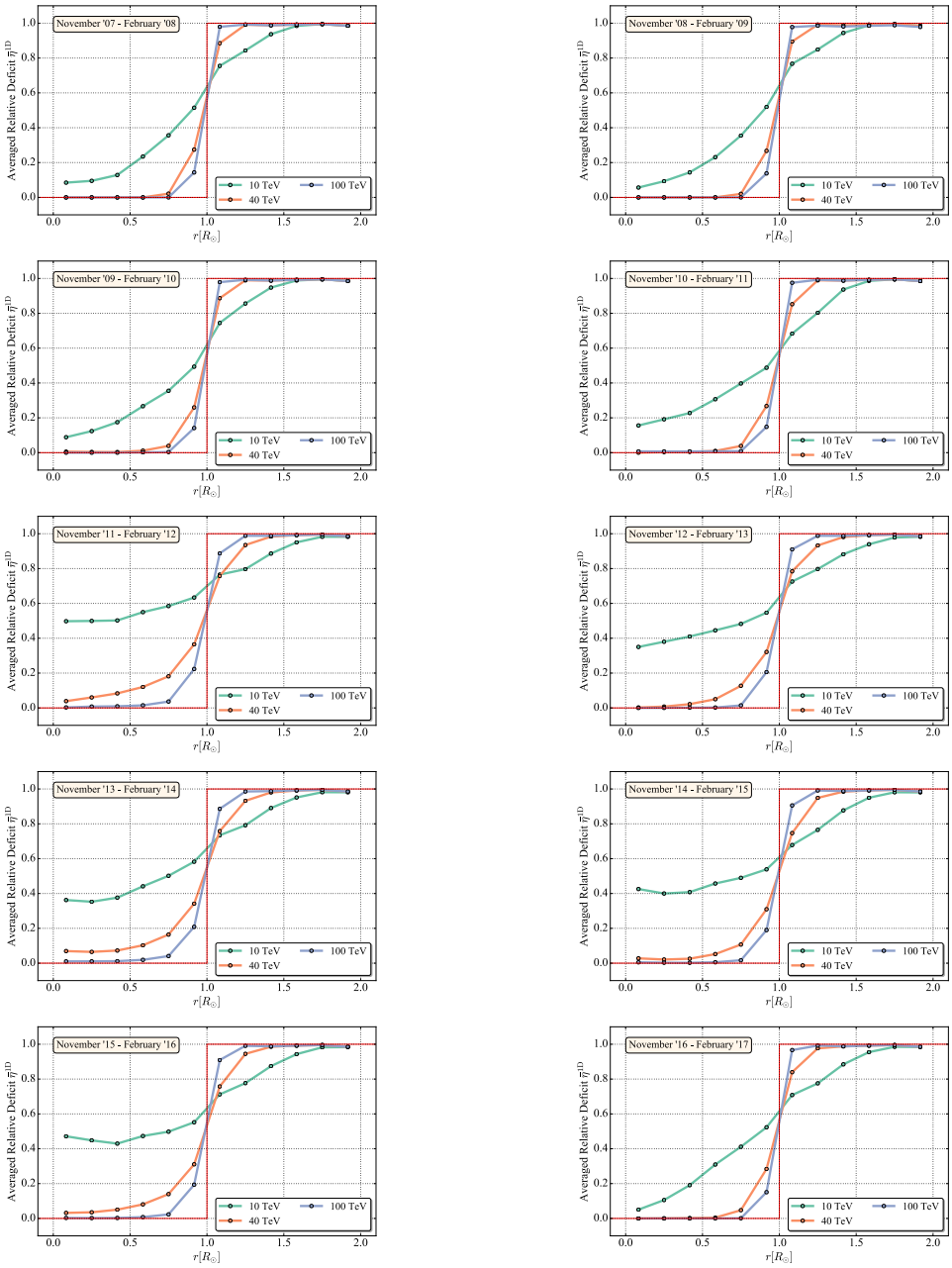

Figure 6.15: *Figure shows the averaged one-dimensional analysis. The bins are arranged concentric around the center of the Sun.*

6.6.1 Temporal behavior of the shadow depth

The integral of the averaged relative deficit, Γ_{ARD}, in one dimension reflects the shadow depth and can be determined for the entire time period of the simulation. It is defined within the constraints of the area of the Sun. It is obtained through

$$\Gamma_{\mathrm{ARD}} = \int_0^{R_\odot} \mathrm{d}r \; \bar{\eta}^{1\mathrm{D}}(r), \tag{6.6.5}$$

with the averaged relative deficit $\eta^{1\mathrm{D}}$. Figure 6.16 shows the results of the integration. For all years, the integral of the highest energy is the lowest compared to the other two energies. For $E_{\mathrm{CR}} = 10$ TeV, the temporal variations in the magnetic field strength are most obvious.

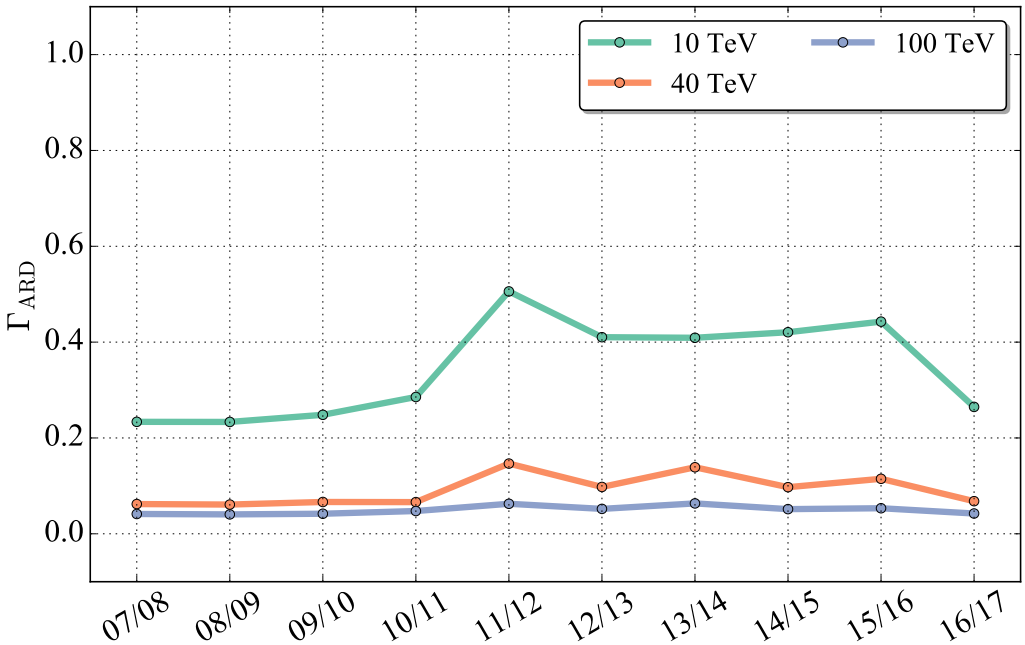

Figure 6.16: *Figure shows the integral of the averaged relative deficit in the season from November through February over ten years.*

6.7 Correlation of start and end positions

The simulation allows for tracing the exact path of the cosmic rays. When a particle hits the solar surface it will not be propagated any further, just like particles that pass a somewhat arbitrarily chosen boundary around the Sun. The end point of all particles can be extracted and consequently, a correlation can be observed between the initial position of the particle, y_{init} and z_{init}, and its final position, y_{final} and z_{final}. The result is shown in Fig. 6.17 for the month December in 2014 and for the three different energies $E_{\text{CR}} = 10$ TeV, $E_{\text{CR}} = 40$ TeV, and $E_{\text{CR}} = 100$ TeV.

With no magnetic field present, it is expected that the correlation describes exactly a line through the origin. In an analysis of the correlations, the linear regression shows a deviation from a situation where a magnetic field is absent. The results are presented in the following equations

$$y_{\text{final}}^{10\text{TeV}} = (0.8618 \pm 0.0035) \cdot y_{\text{init}} - 0.1893 \pm 0.0041 \tag{6.7.1}$$
$$z_{\text{final}}^{10\text{TeV}} = (1.2501 \pm 0.0033) \cdot z_{\text{init}} - 0.0521 \pm 0.0039 \tag{6.7.2}$$

$$y_{\text{final}}^{40\text{TeV}} = (0.9733 \pm 0.0017) \cdot y_{\text{init}} - 0.1834 \pm 0.0019 \tag{6.7.3}$$
$$z_{\text{final}}^{40\text{TeV}} = (1.0398 \pm 0.0014) \cdot z_{\text{init}} + 0.1320 \pm 0.0016 \tag{6.7.4}$$

$$y_{\text{final}}^{100\text{TeV}} = (0.9941 \pm 0.0008) \cdot y_{\text{init}} - 0.0799 \pm 0.0009 \tag{6.7.5}$$
$$z_{\text{final}}^{100\text{TeV}} = (1.0101 \pm 0.0006) \cdot z_{\text{init}} + 0.0122 \pm 0.0007. \tag{6.7.6}$$

The largest deviation occurs in the case of low energy particles, while higher-energetic particles do not seem to be affected much by the magnetic field as can be seen in the slope of the fitted function. This is a confirmation of results obtained in Sections 6.5 and 6.6.

The correlation plot can also serve as an indicator for the deflection angle. As shown in Fig. 6.17, low-energy particles are being deflected more dramatically compared to higher energies. Also, it is obvious that particles traversing very close to the solar surface, the deflection angle reaches a maximum. Particles that have been simulated farther away, show a behavior as if no magnetic field is present.

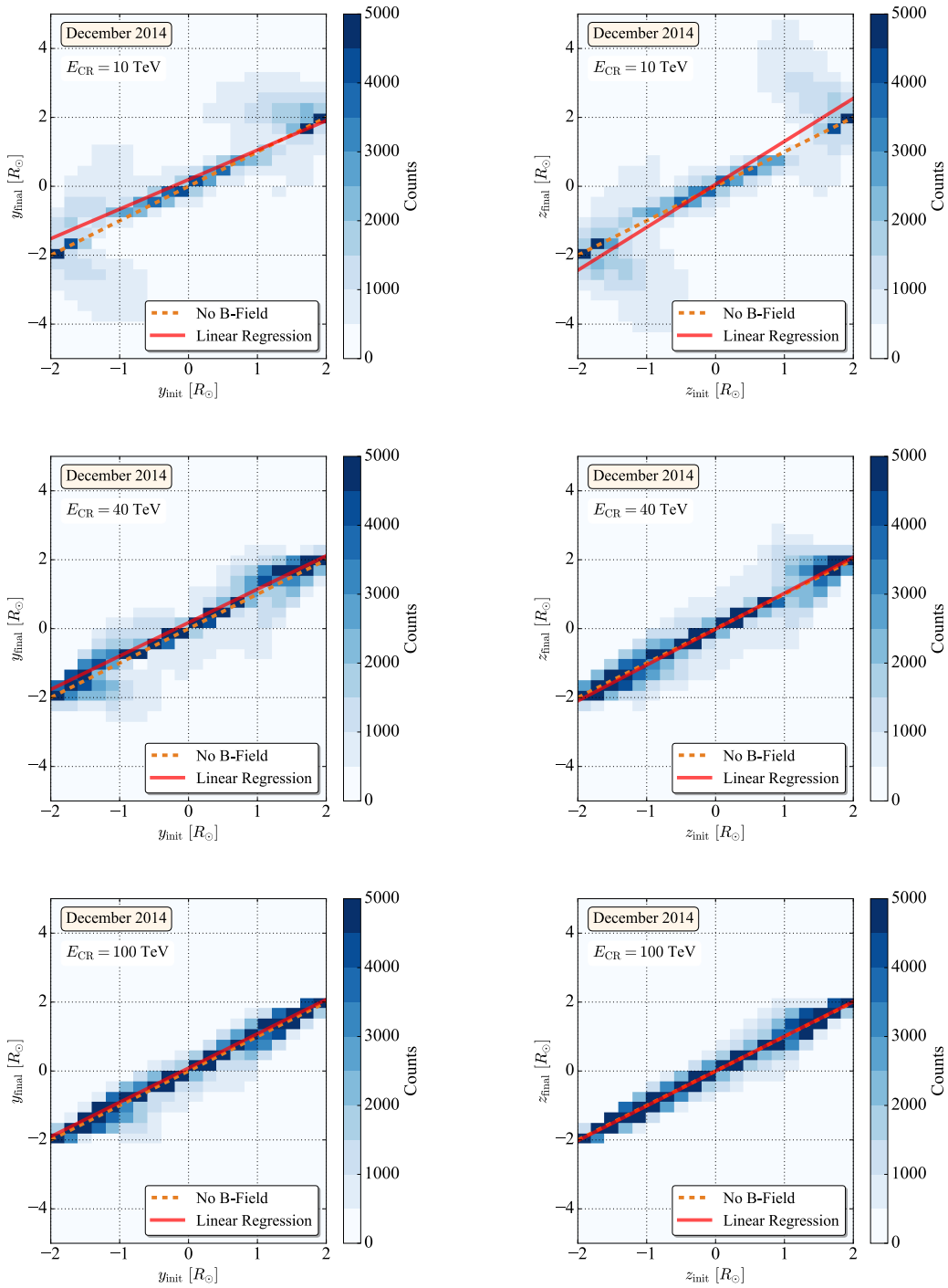

Figure 6.17: *Figure shows the correlation between start and end position of the simulated particles. A linear regression is fitted to the bin content.*

For the presented correlation plots, the respective Pearson correlation coefficients can be determined. Two variables, that have an ideal linear dependence would have a coefficient of one, while uncorrelated quantities have a correlation coefficient of zero. Here, the coefficients are as follows

$$r_y^{10\text{TeV}} = 0.52 \tag{6.7.7}$$
$$r_z^{10\text{TeV}} = 0.53 \tag{6.7.8}$$

$$r_y^{40\text{TeV}} = 0.69 \tag{6.7.9}$$
$$r_z^{40\text{TeV}} = 0.77 \tag{6.7.10}$$

$$r_y^{100\text{TeV}} = 0.89 \tag{6.7.11}$$
$$r_z^{100\text{TeV}} = 0.93. \tag{6.7.12}$$

For higher energies the coefficients approach one. In general, the z-component of starting and final positions shows a higher correlation.

6.8 Summary & Outlook

In this section, the obtained results are discussed and future perspectives are given. The analysis of cosmic rays propagating through the magnetic field of the Sun toward Earth covers the months from November through February of a ten-year period. The time frame has been chosen in order to be able to apply the study of the Sun shadow to IceCube data, which detects cosmic rays from the direction of the Sun from about November through February each year. Following this purpose, the presented analyses have been averaged over these four months, while the results for each month are attached in the Appendix.

The rotation of the magnetic field of the Sun throughout a month is thus included and each shadow image can be seen as the averaged imaged in this time period. Three cosmic ray energies are simulated, $E_{\text{CR}} = 10$ TeV, $E_{\text{CR}} = 40$ TeV, and $E_{\text{CR}} = 100$ TeV. The IceCube detector registers indirectly cosmic rays with a median energy of $E_{\text{CR}} = 40$ TeV from the direction of the Sun and recently a Sun shadow study has been published. The simulation of $E_{\text{CR}} = 10$ TeV particles is based upon the earlier Sun shadow analysis that uses data of the Tibet-III array

and has a median energy of $E_{\mathrm{CR}} = 10$ TeV. The highest energy of the simulation is motivated by the curiosity of how such energetic particles behave in the magnetic field.

The simulation results are evaluated in one- and two dimensions. The 2D analysis consists of a two dimensional histogram showing the cosmic ray shadow from different angles stacked on top of each other. Further, the averaged relative deficit is calculated for each season. It is a histogram that gives information about how many simulated particles, whose starting position is inside the projected area of the Sun, have actually hit the Sun. The result can be related to the solar activity. In years with a low Sun-spot number, the averaged relative deficit has a larger value than in times of higher activities. The actual value depends on the particles' energies. In general, lower energies have a smaller deficit, and magnetic field changes are specifically pronounced in the shadow.
Unlike the averaged relative deficit, the absolute value of the total absorption rate is strongly dependent on the number of simulated particles, its shape, however, is not. All simulated particles that have hit the Sun during the propagation contribute here. Thus, the total absorption rate can also give a measure of the development of the magnetic field strength of the Sun. Again, in times of low solar activity, the value of the total absorption rate is higher than the value when the magnetic field is stronger.

The one dimensional analysis uses concentric bins and counts the hits inside those bins. In radial coordinates, the integral is determined in the range $0 \leq r \leq R_{\odot}$. This value can quantify the number of hits differently to the two-dimensional analysis, and a temporal evolution throughout the seasons is observed. The result is the averaged relative deficit and corresponds well with its two-dimensional equivalent.

Moreover, a correlation is formed between the starting position and its final position of a particle. The result plots show where the particles are deflected the most, namely close to the equator region and for low energies. This effect has been quantified by (a) a linear regression of the data, and (b) by determining the Pearson correlation coefficient. Both parameters have shown a large deflection of low energy particles in contrast to high energy particles, which are not as much affected by the magnetic field. Particles with high energies align well with their

initial position and the regression is close to the path when no magnetic field is present.

Outlook

The study can be continued using the point-spread function of a cosmic ray detector. The simulation of the cosmic ray Sun shadow can thus be specialized for a detector, such that the result becomes directly comparable to the obtained data. Both, simulation results and data analyses can thus be cross checked with each other. Moreover, different models of the magnetic field of the Sun can be implemented, in order to get an idea, which model fits better in specific situations, such as strong magnetic fields. Further, if magnetic field data can be obtained at greater accuracy in time, the effect of coronal mass ejections can be studied.
Further, the simulation of particles with higher atomic numbers can improve the result. The different behavior of these particles in the magnetic field, causes an altered signal detected by an observer on Earth. A composition study would increase the validity of the simulation.

CHAPTER 7

Conclusion & Outlook

The goal of this thesis is to simulate the propagation of cosmic ray particles. Two major physics questions are investigated. First, the flux of cosmic rays induced by supernova remnants is analyzed. This analysis focuses on their contribution to the flux measured on Earth. Second, the shadow of cosmic rays cast by the Sun is analyzed over a ten-year span from 2007 through 2017 in order to capture the influence of the magnetic field.

7.1 Conclusion

Chapter 2 gives an overview of cosmic rays, including their energy spectrum and acceleration processes. Moreover, the evolution of stars is shortly reviewed, and the event of a supernova is described using the remnant Puppis A as an example. The different objectives of neutrino, cosmic ray, and gamma-ray analyses are also discussed.
Particle detectors and their operating principles are presented in Chapter 3. The Sun is described in detail in Chapter 4 which investigates its magnetic field, in particular.

Chapter 5 presents an analysis of cosmic ray propagation. Supernova remnants are powerful galactic sources, and cosmic rays are expected to be accelerated to high

energies. In this analysis, their total contribution to the cosmic ray spectrum is investigated as to whether they are capable of providing the flux up to 10^{15} eV here on Earth. Of 24 respective remnants, 21 have qualified for this analysis, because they have a hadronic component in their spectrum.

The selected sources are distributed in the Galaxy following the mass distribution of massive stars. The analysis covers a calculation of a quasi-static ejection of cosmic rays by the sources over an average lifetime of 10,000 years, neglecting a time-variable source spectrum. Time dependence has been included in a second scenario by using the source's respective total energy, and the time of observation varies with respect to the time at which the explosion occurred.
Both strategies investigate two diffusion coefficients $D \propto E^{\delta}$, namely a Kolmogorov-type diffusion of $\delta_1 = 0.33$ and a stronger diffusion of $\delta_2 = 0.50$. In the first approach, using the simulation of the time-independent ejected spectrum, the δ_1-diffusion correlates well to the data, while the stronger diffusion underestimates the data at higher energies and has a too steep spectrum overall.
The second approach shows that the lower diffusion is too high to match the data points, while the δ_2-diffusion correlates rather well to the data.
Both scenarios, however, neglect the contribution of convection by galactic winds. This would suppress the spectrum, and, especially in the time-dependent scenario with a δ_2-diffusion, allows for an interpretation of other source classes contributing to the cosmic ray flux up to the *knee*.

Chapter 6 presents the simulation of single cosmic ray particles. The purpose of this simulation is the investigation of the deficit in the cosmic ray flux measured by an observer when pointing an instrument in the direction of the Sun. The Sun blocks cosmic rays just like every other celestial body, however, due to its temporally varying magnetic field strength, the shadow is not equal each year in both shape and depth. The experiments of IceCube and the Tibet-III array have observed and analyzed this characteristic using relevant detector data.
In this study, a generic simulation of cosmic rays traversing through the magnetic field of the Sun is presented for different energies, namely $E_{\mathrm{CR}} = 10$ TeV, $E_{\mathrm{CR}} = 40$ TeV, and $E_{\mathrm{CR}} = 100$ TeV. The results of these simulations comprise analyses in 2D and 1D.
The 2D analysis shows the shape and depth of the shadow in a two-dimensional

histogram, and the development of the averaged relative deficit and the total absorption rate over a ten-year cycle. The 1D analysis quantifies the 2D results further. In detail, it includes the averaged relative deficit in 1D, using concentric bins of the heat map.
All presented results compare the three different energies investigated, $E_{\mathrm{CR}} = 10$ TeV, $E_{\mathrm{CR}} = 40$ TeV, and $E_{\mathrm{CR}} = 100$ TeV. The results show a significant alteration of the shadow in years with a stronger magnetic field, for example in December 2011. When the solar activity is low, for example in December 2007, the shadow is less smeared out and the average relative deficit in 2D and 1D is at a minimum for each energy. A comparable result shows the total absorption rate.
In a more technical study of the simulation validating this result, a correlation between the starting point of a simulated cosmic ray trajectory and its end point is formed. Here, it can be seen which trajectories are deflected the most. The result shows a major deflection of particles that propagate close to the geometrical boundaries of the Sun.
In all studies, the lowest energetic particles show the greatest deviations evoked by the magnetic field.

In summary, the key finding of this thesis is that supernova remnants can indeed serve as potential sources for providing the cosmic ray spectrum up to the *knee*. New gamma-ray data were used for a simulation of this claim. The uncertainties, however, cannot be neglected, and it must be said that remnants may not be the only class of accelerators in the Galaxy that contribute to the flux up to this energy. The propagation of cosmic rays around the Sun provides a basis for further analyses when investigating the Sun shadow. It was shown that the temporal variation of the solar magnetic field can be seen in cosmic rays. In general, low-energy particle tracks experience a stronger deflection.

7.2 Outlook

The analyses presented in this thesis can be optimized and expanded. The simulation of galactic cosmic rays uses a small sample of sources. Of the estimated number of currently active accelerators, they make up only 10% - 20%. In the future, new experiments with higher sensitivities such as CTA, can resolve sources with a better spatial accuracy, and consequently a more detailed view of the differential spectrum of sources is possible. A set containing a greater number of relevant sources will certainly improve the validity of the result.
In terms of simulation techniques, several aspects can be improved. First, the grid at which the transport equation is evaluated can be refined such that distances between the grid points can be narrowed. Also, an irregular grid optimized to the source distribution would improve the result of the simulated spectrum. The source's emitted spectrum can be optimized, as well. The approximation of a power-law shaped spectrum holds only for old remnants, whereas such a spectral description fails for young remnants. This characteristic is not included in the current simulation.

In the study of the propagation of cosmic rays through the solar magnetic field, more energies can be studied in the future in order to take into account the growing number of experiments that can measure the cosmic ray Sun shadow from GeV to PeV energies. IceCube measures cosmic rays at a median energy of $E_{\mathrm{CR}} = 40$ TeV, and the Tibet-III array measures at $E_{\mathrm{CR}} = 10$ TeV. Also, different months may be simulated. In order to obtain an improved result, a detector specific point-spread function can be applied, such that the simulation results would better correspond to the data obtained by the detector. For example, implementation in the IceCube simulation chain would allow for an event-based comparison. This would be an asset for the development of models describing the magnetic field of the Sun. The PFSS model can be compared to other models, such as the CSSS model. The planned upgrade of IceCube to IceCube-Gen2 is assumed to support the cosmic ray program by an extension of detected energy range by a factor of ~ 3. The increased area would also improve the collection of coincident data by a factor of ~ 50. Altogether, the Sun shadow analysis would profit greatly from this upgrade and may in turn be beneficial for IceCube's cosmic ray studies, in particular for its calibration.

The KM3NeT detector measures neutrinos in a similar energy regime as IceCube. The ORCA detector is a low-energy extension of KM3NeT and is supposed to detect neutrinos produced by cosmic rays interacting with the Earth's atmosphere. Located in the Mediterranean, the Northern Hemisphere can be studied and results can be compared to IceCube's analyses. This way, it has great potential for completing the picture of the cosmic ray Sun shadow, as it allows for an uninterrupted data collection.
The HAWC Observatory measures cosmic ray energies of approximately 100 GeV through 100 TeV. In the simulation of the Sun shadow, lower energies than those presented in this thesis can be analyzed.
In the future, the simulation can be improved by including cosmic ray interactions (a) in the solar corona and (b) with the magnetic field of the Earth. With an optimized measurement of the magnetic field of the Sun, the effect of coronal mass ejections can also be studied.
Further, a multipole-analysis can be performed in order to study in detail the deviation from radial symmetry.

Bibliography

[1] C. Patrignani *et al.*. Review of Particle Physics. *Chin. Phys.*, vol. C40(10), p. 100001, 2016.

[2] V. F. Hess. Über Beobachtungen der durchdringenden Strahlung bei sieben Freiballonfahrten. *Phys. Z.*, vol. 13, p. 1084, 1912.

[3] N. M. A. 2014. Victor F. Hess - Biographical. `http://www.nobelprize.org/nobel_organizations/nobelfoundation/publications/lectures/index.html`, 2017. [Online; last time accessed: 28-February-2017].

[4] A. Haungs. Cosmic rays in the knee energy range. *Astrophysics and Space Sciences Transactions*, vol. 7, p. 295, 2011.

[5] P. Blasi. The origin of galactic cosmic rays. *Astron. & Astroph. Rev.*, vol. 21, 70, 2013.

[6] A. Wolfendale and A. Erlykin. *Astroparticle Physics*, vol. 53, p. 115, 2014.

[7] P. L. Biermann and G. Sigl. Introduction to Cosmic Rays. In Physics and Astrophysics of Ultra-High-Energy Cosmic Rays, vol. 576 of *Lecture Notes in Physics, Berlin Springer Verlag* (edited by M. Lemoine and G. Sigl), (p. 1), 2001.

[8] J. K. Becker. High-energy neutrinos in the context of multimessenger astrophysics. *Physics Reports*, vol. 458, pp. 173–246, 2008.

[9] W. D. Apel, J. C. Arteaga-Velázquez, K. Bekk, *et al.*. Kneelike Structure in the Spectrum of the Heavy Component of Cosmic Rays Observed with KASCADE-Grande. *Phys. Rev. Lett.*, vol. 107, p. 171104, 2011.

[10] V. S. Ptuskin, S. I. Rogovaya, V. N. Zirakashvili, *et al.*. Diffusion and drift of very high energy cosmic rays in galactic magnetic fields. *Astron. & Astrophys.*, vol. 268, pp. 726–735, 1993.

[11] D. J. Bird, S. C. Corbato, H. Y. Dai, *et al.*. The cosmic-ray energy spectrum observed by the Fly's Eye. *The Astrophysical Journal*, vol. 424, pp. 491–502, 1994.

[12] K. Greisen. End to the Cosmic-Ray Spectrum? *Phys. Rev. Lett.*, vol. 16, pp. 748–750, 1966.

[13] G. T. Zatsepin and V. A. Kuzmin. Upper limit of the spectrum of cosmic rays. *Sov. Phys. JETP Lett.*, vol. 4, pp. 78–80, 1966. [Pisma Zh. Eksp. Teor. Fiz.4,114(1966)].

[14] H. S. Ahn, P. Allison, M. G. Bagliesi, *et al.*. Discrepant Hardening Observed in Cosmic-ray Elemental Spectra. *Astroph. J. Lett.*, vol. 714, p. L89, 2010.

[15] P. L. Biermann, J. K. Becker, J. Dreyer, *et al.*. The Origin of Cosmic Rays: Explosions of Massive Stars with Magnetic Winds and Their Supernova Mechanism. *The Astrophysical Journal*, vol. 725, p. 184, 2010.

[16] S. Haino *et al.*. Precision measurement of the proton flux with AMS. International Cosmic Ray Conference, 2013.

[17] V. Choutko *et al.*. Precision measurement of the helium flux with AMS. International Cosmic Ray Conference, 2013.

[18] B. Khiali, S. Haino, and J. Feng. Anomalous Galactic Cosmic Rays in the Framework of AMS-02. *The Astrophysical Journal*, vol. 835, 229, 2017.

[19] W. D. Apel, J. C. Arteaga-Velàzquez, K. Bekk, *et al.*. KASCADE-Grande measurements of energy spectra for elemental groups of cosmic rays.

[20] W. D. Apel, J. C. Arteaga-Velàzquez, K. Bekk, *et al.*. The KASCADE-Grande energy spectrum of cosmic rays and the role of hadronic interaction models. *Advances in Space Research*, vol. 53, p. 1456, 2014.

[21] M. G. Aartsen, R. Abbasi, Y. Abdou, *et al.*. Measurement of the cosmic ray energy spectrum with IceTop-73. *Phys. Rev. D*, vol. 88(4), 042004, 2013.

[22] M. Fukushima. Recent results from telescope array. In European Physical Journal Web of Conferences, vol. 99 of *European Physical Journal Web of Conferences*, (p. 04004), 2015.

[23] K.-H. Kampert and M. Unger. Measurements of the Cosmic Ray Composition with Air Shower Experiments. *Astroparticle Physics*, vol. 35, pp. 660–678, 2012.

[24] D. García-Gámez *et al.*. Observations of the longitudinal development of extensive air showers with the surface detectors of the Pierre Auger Observatory. International Cosmic Ray Conference, 2013. ArXiv:1307.5059.

[25] A. Aab, P. Abreu, M. Aglietta, *et al.*. Evidence for a mixed mass composition at the 'ankle' in the cosmic-ray spectrum. *Physics Letters B*, vol. 762, pp. 288–295, 2016.

[26] A. M. Hillas. The Origin of Ultra-High-Energy Cosmic Rays. *Ann. Rev. Astron. Astrophys.*, vol. 22, pp. 425–444, 1984.

[27] K. V. Ptitsyna and S. V. Troitsky. PHYSICS OF OUR DAYS Physical conditions in potential accelerators of ultra-high-energy cosmic rays: updated Hillas plot and radiation-loss constraints. *Physics Uspekhi*, vol. 53, pp. 691–701, 2010.

[28] F. Fraschetti. On the acceleration of ultra-high-energy cosmic rays. *Philosophical Transactions of the Royal Society of London Series A*, vol. 366, pp. 4417–4428, 2008.

[29] E. Fermi. On the Origin of the Cosmic Radiation. *Phys. Rev.*, vol. 75, pp. 1169–1174, 1949.

[30] C. Grupen. Astroparticle Physics. *Springer*, 2005.

[31] T. K. Gaisser. Cosmic Rays and Particle Physics. *Cambridge University Press*, (p. 295), 1991.

[32] L. O. Drury and A. W. Strong. Cosmic-ray diffusive reacceleration: a critical look. *PoS*, vol. ICRC2015, p. 483, 2016.

[33] T. Stanev. High Energy Cosmic Rays. Springer-Verlag Berlin Heidelberg, 2010, 2010. ISBN 978-3-540-85147-9.

[34] A. Unsöld and B. Baschek. Der neue Kosmos: Einführung in die Astronomie und Astrophysik. Springer Berlin Heidelberg, 2004. ISBN 9783540421771.

[35] Chandra X-Ray Observatory: Pulsating Variable Stars and the Hertzsprung-Russell (H-R) Diagram. Website. Accessed: May 2017.
URL `http://chandra.harvard.edu/edu/formal/variable_stars/bg_info.html`

[36] P. F. Winkler and R. P. Kirshner. Discovery of fast-moving oxygen filaments in Puppis A. *The Astrophysical Journal*, vol. 299, pp. 981–986, 1985.

[37] W. Becker, T. Prinz, P. F. Winkler, *et al.*. The Proper Motion of the Central Compact Object RX J0822-4300 in the Supernova Remnant Puppis A. *The Astrophysical Journal*, vol. 755, 141, 2012.

[38] E. M. Reynoso, A. J. Green, S. Johnston, *et al.*. Observations of the neutral hydrogen surrounding the radio-quiet neutron star RX J0822-4300 in Puppis A. *MNRAS*, vol. 345, pp. 671–677, 2003.

[39] B. Woermann, M. J. Gaylard, and R. Otrupcek. Hydroxyl lines towards Puppis A. *MNRAS*, vol. 317, pp. 421–428, 2000.

[40] M. Mandelartz and J. Becker Tjus. Prediction of the diffuse neutrino flux from cosmic ray interactions near supernova remnants. *Astroparticle Physics*, vol. 65, pp. 80–100, 2015.

[41] M. Lemoine-Goumard, M.-H. Grondin, J. W. Hewitt, *et al.*. Fermi-LAT and WMAP observations of the Puppis A supernova remnant. In American Institute of Physics Conference Series, vol. 1505 of *American Institute of Physics Conference Series*, (pp. 225–228), 2012.

[42] L. O'C. Drury. Origin(s) of Cosmic Rays. *ArXiv e-prints*, 2014.

[43] M. Kroll, J. Becker Tjus, B. Eichmann, *et al.*. Gamma-ray emitting supernova remnants as the origin of Galactic cosmic rays. *ASTRA Proceedings*, vol. 2, pp. 57–62, 2015.

[44] G. Dubner, N. Loiseau, P. Rodríguez-Pascual, *et al.*. The most complete and detailed X-ray view of the SNR Puppis A. *Astronomy & Astrophysics*, vol. 555, A9, 2013.

[45] R. Alves Batista, A. Dundovic, M. Erdmann, *et al.*. CRPropa 3 - a public astrophysical simulation framework for propagating extraterrestrial ultra-high energy particles. *JCAP*, vol. 5, 038, 2016.

[46] L. Merten, J. Becker Tjus, H. Fichtner, *et al.*. CRPropa 3.1 – A low energy extension based on stochastic differential equations. *ArXiv e-prints*, 2017.

[47] P. Desiati and E. G. Zweibel. The Transport of Cosmic Rays Across Magnetic Fieldlines. *The Astrophysical Journal*, vol. 791(1), p. 51, 2014.

[48] B. Eichmann and J. Becker Tjus. The Radio-Gamma Correlation in Starburst Galaxies. *The Astrophysical Journal*, vol. 821, 87, 2016.

[49] T. M. Yoast-Hull, J. E. Everett, J. S. Gallagher, *et al.*. Winds, Clumps, and Interacting Cosmic Rays in M82. *The Astrophysical Journal*, vol. 768, p. 53, 2013.

[50] R. Schlickeiser and F. Jenko. Cosmic ray transport in non-uniform magnetic fields: consequences of gradient and curvature drifts. *Journal of Plasma Physics*, vol. 76(3-4), pp. 317–327, 2010.

[51] A. E. Vladimirov, S. W. Digel, G. Jóhannesson, *et al.*. GALPROP WebRun: An internet-based service for calculating galactic cosmic ray propagation and associated photon emissions. *Computer Physics Communications*, vol. 182, pp. 1156–1161, 2011.

[52] C. Evoli, D. Gaggero, D. Grasso, *et al.*. Cosmic ray nuclei, antiprotons and gamma rays in the galaxy: a new diffusion model. *JCAP*, vol. 10, 018, 2008.

[53] R. Kissmann. PICARD: A novel code for the Galactic Cosmic Ray propagation problem. *Astroparticle Physics*, vol. 55, pp. 37–50, 2014.

[54] A. Strong *et al.*. GALPROP Version v54: *Explanatory Supplement*, 2011. Accessed: April 2017.
URL `http://galprop.stanford.edu/code.php?option=manual`

[55] J. Crank and P. Nicolson. A practical method for numerical evaluation of solutions of partial differential equations of the heat-conduction type. *Advances in Computational Mathematics*, vol. 6(1), pp. 207–226, 1996. ISSN 1572-9044.

[56] M. Galassi, J. Davies, J. Theiler, *et al.*. GNU Scientific Library Reference Manual. ISBN 0954612078, url=http://www.gnu.org/software/gsl/.

[57] G. R. Blumenthal and R. J. Gould. *Reviews of Modern Physics*, vol. 42, p. 237, 1970.

[58] R. Schlickeiser. Cosmic Ray Astrophysics. *Springer*, 2002.

[59] J. Becker Tjus, B. Eichmann, M. Kroll, *et al.*. Gamma-ray emitting supernova remnants as the origin of Galactic cosmic rays? *Astroparticle Physics*, vol. 81, pp. 1–11, 2016.

[60] A. A. Abdo, M. Ackermann, M. Ajello, *et al.*. Gamma-Ray Emission from the Shell of Supernova Remnant W44 Revealed by the Fermi LAT. *Science*, vol. 327, p. 1103, 2010.

[61] A. A. Abdo, M. Ackermann, M. Ajello, *et al.*. Spectrum of the Isotropic Diffuse Gamma-Ray Emission Derived from First-Year Fermi Large Area Telescope Data. *Phys. Rev. Lett.*, vol. 104(10), p. 101101, 2010.

[62] T. Jogler and S. Funk. Revealing W51C as a Cosmic Ray Source Using Fermi-LAT Data. *The Astrophysical Journal*, vol. 816, 100, 2016.

[63] TeV Catalog. `http://tevcat.uchicago.edu/`, 2017.

[64] Tibet As-Gamma Array. `http://www.icrr.u-tokyo.ac.jp/em/index.html`, 2017. [Accessed: March 2017].

[65] M. Amenomori *et al.*. The All-particle spectrum of primary cosmic rays in the wide energy range from 10**14 eV to 10**17 eV observed with the Tibet-III air-shower array. *The Astrophysical Journal*, vol. 678, pp. 1165–1179, 2008.

[66] F. Halzen and S. R. Klein. *Review of Scientific Instruments*, vol. 81(8), p. 081101, 2010.

[67] M. G. Aartsen, R. Abbasi, Y. Abdou, *et al.*. Evidence for High-Energy Extraterrestrial Neutrinos at the IceCube Detector. *Science*, vol. 342, 1242856, 2013.

[68] M. G. Aartsen, R. Abbasi, Y. Abdou, *et al.*. Observation of High-Energy Astrophysical Neutrinos in Three Years of IceCube Data. *Phys. Rev. Lett.*, vol. 113(10), 101101, 2014.

[69] K. A. Olive *et al.*. Review of Particle Physics. *Chin. Phys.*, vol. C38, p. 090001, 2014.

[70] J. K. Becker. High-energy neutrinos in the context of multimessenger astrophysics. *Physics Reports*, vol. 458(4-5), pp. 173 – 246, 2008. ISSN 0370-1573.

[71] M. G. Aartsen, K. Abraham, M. Ackermann, *et al.*. Evidence for Astrophysical Muon Neutrinos from the Northern Sky with IceCube. *Phys. Rev. Lett.*, vol. 115, p. 081102, 2015.

[72] M. G. Aartsen, M. Ackermann, J. Adams, *et al.*. Measurement of the ν_μ energy spectrum with IceCube-79. *ArXiv e-prints*, 2017.

[73] A. Achterberg, M. Ackermann, J. Adams, *et al.*. First year performance of the IceCube neutrino telescope. *Astroparticle Physics*, vol. 26, pp. 155–173, 2006.

[74] M. G. Aartsen, K. Abraham, M. Ackermann, *et al.*. Characterization of the atmospheric muon flux in IceCube. *Astroparticle Physics*, vol. 78, pp. 1–27, 2016.

[75] F. Halzen and S. R. Klein. Invited Review Article: IceCube: An instrument for neutrino astronomy. *Review of Scientific Instruments*, vol. 81(8), pp. 081101–081101, 2010.

[76] M. G. Aartsen, R. Abbasi, Abdou, *et al.*. Evidence for High-Energy Extraterrestrial Neutrinos at the IceCube Detector. *Science*, vol. 342, p. 1242856, 2013.

[77] T. DeYoung, R. Abbasi, Y. Abdou, *et al.*. Particle physics in ice with IceCube DeepCore. *Nuclear Instruments and Methods in Physics Research A*, vol. 692, pp. 180–183, 2012.

[78] M. G. Aartsen, M. Ackermann, J. Adams, *et al.*. Determining neutrino oscillation parameters from atmospheric muon neutrino disappearance with three years of IceCube DeepCore data. *Phys. Rev. D*, vol. 91, p. 072004, 2015.

[79] R. Abbasi, Y. Abdou, M. Ackermann, *et al.*. IceTop: The surface component of IceCube. *Nuclear Instruments and Methods in Physics Research Section A: Accelerators, Spectrometers, Detectors and Associated Equipment*, vol. 700, pp. 188 – 220, 2013. ISSN 0168-9002.

[80] R. Abbasi, Y. Abdou, M. Ackermann, *et al.*. Cosmic ray composition and energy spectrum from 1-30 PeV using the 40-string configuration of IceTop and IceCube. *Astroparticle Physics*, vol. 42, pp. 15–32, 2013.

[81] S. Toscano. Observation of Anisotropy in the Arrival Directions of Galactic Cosmic Rays at Multiple Angular Scales with IceCube. *Nucl. Phys. Proc. Suppl.*, vol. 212-213, pp. 201–206, 2011.

[82] R. Abbasi, Y. Abdou, T. Abu-Zayyad, *et al.*. Observation of an Anisotropy in the Galactic Cosmic Ray arrival direction at 400 TeV with IceCube. *The Astrophysical Journal*, vol. 746, p. 33, 2012.

[83] M. Santander, R. Abbasi, Y. Abdou, *et al.*. Anisotropy of TeV and PeV cosmic rays with IceCube and IceTop. *ArXiv e-prints*, 2012.

[84] M. G. Aartsen, R. Abbasi, Y. Abdou, *et al.*. Observation of Cosmic-Ray Anisotropy with the IceTop Air Shower Array. *The Astrophysical Journal*, vol. 765, 55, 2013.

[85] IceCube Collaboration. IceCube Detector. `http://icecube.wisc.edu/gallery/press/view/1336`, 2017. [Online; last time accessed: 19-March-2017].

[86] J. Beringer, J. F. Arguin, R. M. Barnett, *et al.*. Review of Particle Physics Particle Data Group. (1). ISSN 1550-2368.

[87] M. G. Aartsen, K. Abraham, M. Ackermann, *et al.*. The IceCube Neutrino Observatory - Contributions to ICRC 2015 Part II: Atmospheric and Astrophysical Diffuse Neutrino Searches of All Flavors. *ArXiv e-prints*, 2015.

[88] M. G. Aartsen, K. Abraham, M. Ackermann, *et al.*. Observation and Characterization of a Cosmic Muon Neutrino Flux from the Northern Hemisphere Using Six Years of IceCube Data. *The Astrophysical Journal*, vol. 833, 3, 2016.

[89] M. Aguilar, J. Alcaraz, J. Allaby, *et al.*. First Result from the Alpha Magnetic Spectrometer on the International Space Station: Precision Measurement of the Positron Fraction in Primary Cosmic Rays of 0.5-350 GeV. *Phys. Rev. Lett.*, vol. 110, p. 141102, 2013.

[90] P. V. Doetinchem, S. Fopp, W. Karpinski, *et al.*. Performance of the AMS-02 transition radiation detector. *Nuclear Instruments and Methods in Physics Research A*, vol. 558, pp. 526–535, 2006.

[91] Y. Feng and S. Yang. AMS-02 ECAL Structural Qualification Testing Overview. In Environmental Testing for Space Programmes, vol. 558 of *ESA Special Publication* (edited by K. Fletcher), (pp. 91–94), 2004.

[92] D. Casadei, L. Baldini, V. Bindi, *et al.*. The AMS-02 Time of Flight System. *ArXiv Astrophysics e-prints*, 2002.

[93] P. von Doetinchem, T. Kirn, K. Luebelsmeyer, *et al.*. The Anticoincidence Counter System of AMS-02. *ArXiv e-prints*, 2009.

[94] J. Alcaraz *et al.*. The alpha magnetic spectrometer silicon tracker: Performance results with protons and helium nuclei. *Nucl. Instrum. Meth.*, vol. A593, pp. 376–398, 2008.

[95] F. Giovacchini. Performance in space of the AMS-02 RICH detector. *Nuclear Instruments and Methods in Physics Research A*, vol. 766, pp. 57–60, 2014.

[96] M. Littmann, F. Espenak, and K. Willcox. Totality: Eclipses of the Sun. OUP Oxford, 2008. ISBN 9780191579943.

[97] W. H. Wollaston. A Method of Examining Refractive and Dispersive Powers, by Prismatic Reflection. *Phil. Trans. R. Soc. Lond.*, (92), pp. 365–380, 1802.

[98] J. von Fraunhofer. Bestimmung des Brechungs- und des Farben-Zerstreuungs - Vermögens verschiedener Glasarten, in Bezug auf die Vervollkommnung achromatischer Fernröhre. *Denkschriften der Königlichen Akademie der Wissenschaften zu München*, vol. 5, pp. 193–226, 1814-1815.

[99] H. Schwabe. Sonnen - Beobachtungen im Jahre 1843. No. v. 21 in Astronomische Nachrichten. WILEY-VCH Verlag, 1844.

[100] R. Wolf. Astronomische Mitteilungen XLII. *Astronomische Mitteilungen der Eidgenössischen Sternwarte Zurich*, vol. 5, pp. 29–60, 1877.

[101] R. Schwenn and E. Marsch. Physics of the Inner Heliosphere I: Large-Scale Phenomena. Physics and Chemistry in Space. Springer Berlin Heidelberg, 2012. ISBN 9783642753619.

[102] S. K. Solanki, B. Inhester, and M. Schüssler. The solar magnetic field. *Reports on Progress in Physics*, vol. 69, pp. 563–668, 2006.

[103] G. E. Hale. On the Probable Existence of a Magnetic Field in Sun-Spots. *The Astrophysical Journal*, vol. 28, p. 315, 1908.

[104] D. V. Hoyt and K. H. Schatten. Group Sunspot Numbers: A New Solar Activity Reconstruction. *Solar Physics*, vol. 179, pp. 189–219, 1998.

[105] K. Tapping. Solar Activity Indices. *Encyclopedia of Astronomy and Astrophysics*, 2000.

[106] G. E. Hale and S. B. Nicholson. The Law of Sun-Spot Polarity. *The Astrophysical Journal*, vol. 62, p. 270, 1925.

[107] D. Hathaway. Graphic of the Sun spot number. webpage. NASA/ARC, Accessed: April, 2017.
URL `https://solarscience.msfc.nasa.gov/SunspotCycle.shtml`

[108] P. J. Mohr, D. B. Newell, and B. N. Taylor. CODATA recommended values of the fundamental physical constants: 2014. *Rev. Mod. Phys.*, vol. 88, p. 035009, 2016.

[109] M. Stix. The Sun: An Introduction. Astronomy and Astrophysics Library. Springer Berlin Heidelberg, 2004. ISBN 9783540207412.

[110] M. Alonso and E. Finn. Quantenphysik und statistische Physik. Oldenbourg, 2005. ISBN 9783486577624.

[111] E. Ilonidis. Helioseismic Detections of Sunspot Regions. Ph.D. thesis, Stanford University. Department of Physics, 2012.

[112] J. W. Harvey *et al.*. The Global Oscillation Network Group (GONG) Project. *Science*, vol. 272, pp. 1284–1286, 1996.

[113] Global Oscillation Network Group (GONG). webpage. NASA/GONG, Accessed: April, 2017.
URL `http://gong.nso.edu/`

[114] C. J. Henney, C. U. Keller, J. W. Harvey, *et al.*. SOLIS Vector Spectromagnetograph: Status and Science. In Solar Polarization 5: In Honor of Jan Stenflo, vol. 405 of *Astronomical Society of the Pacific Conference Series* (edited by S. V. Berdyugina, K. N. Nagendra, and R. Ramelli), (p. 47), 2009.

[115] K. H. Schatten, J. M. Wilcox, and N. F. Ness. A model of interplanetary and coronal magnetic fields. *Solar Physics*, vol. 6, pp. 442–455, 1969.

[116] M. D. Altschuler and G. Newkirk. Magnetic Fields and the Structure of the Solar Corona. I: Methods of Calculating Coronal Fields. *Solar Physics*, vol. 9, pp. 131–149, 1969.

[117] J. T. Hoeksema. Structure and evolution of the large scale solar and heliospheric magnetic fields. Ph.D. thesis, Stanford Univ., CA., 1984.

[118] E. N. Parker. Dynamics of the Interplanetary Gas and Magnetic Fields. *The Astrophysical Journal*, vol. 128, p. 664, 1958.

[119] T. Wiengarten, J. Kleimann, H. Fichtner, *et al.*. Cosmic Ray Transport in Heliospheric Magnetic Structures. I. Modeling Background Solar Wind Using the CRONOS Magnetohydrodynamic Code. *The Astrophysical Journal*, vol. 788, 80, 2014.

[120] M. D. Altschuler, R. H. Levine, M. Stix, *et al.*. High resolution mapping of the magnetic field of the solar corona. *Solar Physics*, vol. 51, pp. 345–375, 1977.

[121] G. Tóth, B. van der Holst, and Z. Huang. Obtaining Potential Field Solutions with Spherical Harmonics and Finite Differences. *The Astrophysical Journal*, vol. 732, 102, 2011.

[122] P. Riley, J. A. Linker, Z. Mikić, *et al.*. A Comparison between Global Solar Magnetohydrodynamic and Potential Field Source Surface Model Results. *The Astrophysical Journal*, vol. 653(2), p. 1510, 2006.

[123] M. Schulz, E. N. Frazier, and D. J. Boucher, Jr. Coronal magnetic-field model with non-spherical source surface. *Solar Physics*, vol. 60, pp. 83–104, 1978.

[124] M. Schulz. Non-spherical source-surface model of the heliosphere: a scalar formulation. *Annales Geophysicae*, vol. 15, pp. 1379–1387, 1997.

[125] T. J. Bogdan and B. C. Low. The three-dimensional structure of magnetostatic atmospheres. II - Modeling the large-scale corona. *The Astrophysical Journal*, vol. 306, pp. 271–283, 1986.

[126] B. Poduval and X. P. Zhao. Validating Solar Wind Prediction Using the Current Sheet Source Surface Model. *The Astrophysical Journal Letters*, vol. 782, L22, 2014.

[127] X. Zhao and J. T. Hoeksema. Prediction of the interplanetary magnetic field strength. *Journal of Geophysical Research*, vol. 100, pp. 19–33, 1995.

[128] R. Abbasi, Y. Abdou, T. Abu-Zayyad, *et al.*. Measurement of the Anisotropy of Cosmic-ray Arrival Directions with IceCube. *The Astrophysical Journal Letters*, vol. 718, pp. L194–L198, 2010.

[129] M. Amenomori, X. J. Bi, D. Chen, *et al.*. On Temporal Variations of the Multi-TeV Cosmic Ray Anisotropy Using the Tibet III Air Shower Array. *The Astrophysical Journal*, vol. 711, pp. 119–124, 2010.

[130] A. A. Abdo, B. T. Allen, T. Aune, *et al.*. The Large-Scale Cosmic-Ray Anisotropy as Observed with Milagro. *The Astrophysical Journal*, vol. 698, pp. 2121–2130, 2009.

[131] F. Bos. Studying moon and sun shadows by using atmospheric muons detected with IceCube. Ph.D. thesis, 2017.

[132] Sketch of the Sun shadow. Accessed: April, 2017.
URL `http://www.icrr.u-tokyo.ac.jp/testblog/2013/07/11140001.html`

[133] M. G. Aartsen, R. Abbasi, Y. Abdou, *et al.*. Observation of the cosmic-ray shadow of the Moon with IceCube. *ArXiv e-prints*, 2013.

[134] F. Bos, F. Tenholt, J. Becker Tjus, *et al.*. Observation of the Cosmic-Ray Shadow of the Moon and Sun with IceCube. *ASTRA Proceedings*, vol. 2, pp. 5–8, 2015.

[135] M. Ambrosio, R. Antolini, A. Baldini, *et al.*. Moon and Sun shadowing effect in the MACRO detector. *Astroparticle Physics*, vol. 20, pp. 145–156, 2003.

[136] P. Achard, O. Adriani, M. Aguilar-Benitez, *et al.*. Measurement of the shadowing of high-energy cosmic rays by the Moon: A search for TeV-energy antiprotons. *Astroparticle Physics*, vol. 23, pp. 411–434, 2005.

[137] P. Adamson, C. Andreopoulos, D. S. Ayres, *et al.*. Observation in the MINOS far detector of the shadowing of cosmic rays by the sun and moon. *Astroparticle Physics*, vol. 34, pp. 457–466, 2011.

[138] B. Bartoli, P. Bernardini, X. J. Bi, *et al.*. Observation of the cosmic ray moon shadowing effect with the ARGO-YBJ experiment. *Physical Review D*, vol. 84(2), 022003, 2011.

[139] A. U. Abeysekara, R. Alfaro, C. Alvarez, *et al.*. The HAWC Gamma-Ray Observatory: Observations of Cosmic Rays. *ArXiv e-prints*, 2013.

[140] M. Amenomori, X. J. Bi, D. Chen, *et al.*. Probe of the Solar Magnetic Field Using the "Cosmic-Ray Shadow" of the Sun. *Physical Review Letters*, vol. 111(1), 011101, 2013.

[141] T. K. Gaisser. Cosmic Rays and Particle Physics. *Cambridge University Press*, (p. 295), 1991.

[142] T. Stanev. High-energy cosmic rays. Springer Praxis Books/Astronomy and Planetary Sciences, 2nd edn., 2010.

[143] D. A. Green. A catalogue of 294 Galactic supernova remnants. *Bulletin of the Astronomical Society of India*, vol. 42, pp. 47–58, 2014.

[144] Y. Xu, H. J. Newberg, J. L. Carlin, *et al.*. Rings and Radial Waves in the Disk of the Milky Way. *The Astrophysical Journal*, vol. 801, 105, 2015.

[145] R. Diehl, H. Halloin, K. Kretschmer, *et al.*. Radioactive ^{26}Al from massive stars in the Galaxy. *Nature*, vol. 439, pp. 45–47, 2006.

[146] G. I. Taylor. The Air Wave Surrounding an Expanding Sphere. *Proceedings of the Royal Society of London Series A*, vol. 186, pp. 273–292, 1946.

[147] L. I. Sedov. Similarity and Dimensional Methods in Mechanics. Academic Press, 1959.

[148] T. A. Thompson, E. Quataert, and N. Murray. Radio emission from supernova remnants: implications for post-shock magnetic field amplification & the magnetic fields of galaxies. *MNRAS*, vol. 397, pp. 1410–1419, 2009.

[149] G. L. Case and D. Bhattacharya. A New Σ-D Relation and Its Application to the Galactic Supernova Remnant Distribution. *The Astrophysical Journal*, vol. 504, pp. 761–772, 1998.

[150] D. A. Green. A revised Galactic supernova remnant catalogue. *Bulletin of the Astronomical Society of India*, vol. 37, pp. 45–61, 2009.

[151] P. F. Michelson, W. B. Atwood, and S. Ritz. Fermi Gamma-ray Space Telescope: high-energy results from the first year. *Reports on Progress in Physics*, vol. 73(7), p. 074901, 2010.

[152] M. de Naurois. H.E.S.S.-II - Gamma ray astronomy from 20 GeV to hundreds of TeV's. In European Physical Journal Web of Conferences, vol. 136 of *European Physical Journal Web of Conferences*, (p. 03001), 2017.

[153] J. Aleksić, S. Ansoldi, L. A. Antonelli, *et al.*. The major upgrade of the MAGIC telescopes, Part II: A performance study using observations of the Crab Nebula. *Astroparticle Physics*, vol. 72, pp. 76–94, 2016.

[154] J. Holder. VERITAS: Status and Highlights. *International Cosmic Ray Conference*, vol. 12, p. 137, 2011.

[155] J. Pretz. Highlights from the High Altitude Water Cherenkov Observatory. *PoS*, vol. ICRC2015, p. 025, 2016.

[156] M. Persic. CTA: the future of ground-based γ-ray astrophysics. *Nuclear Physics B Proceedings Supplements*, vol. 239, pp. 210–215, 2013.

[157] D. P. Cox. Cooling and Evolution of a Supernova Remnant. *The Astrophysical Journal*, vol. 178, pp. 159–168, 1972.

[158] A. W. Strong. Galprop v54. `http://galprop.stanford.edu/`, 2017. [Online; last time accessed: 19-January-2017].

[159] P. L. Biermann, J. K. Becker, J. Dreyer, *et al.*. The Origin of Cosmic Rays: Explosions of Massive Stars with Magnetic Winds and Their Supernova Mechanism. *The Astrophysical Journal*, vol. 725, pp. 184–187, 2010.

[160] P. L. Biermann, J. K. Becker, A. Meli, *et al.*. Cosmic Ray Electrons and Positrons from Supernova Explosions of Massive Stars. *Phys. Rev. Lett.*, vol. 103, p. 061101, 2009.

[161] P. L. Biermann, J. K. Becker, G. Caceres, *et al.*. The WMAP Haze from the Galactic Center Region Due to Massive Star Explosions and a Reduced Cosmic Ray Scale Height. *The Astrophysical Journal*, vol. 710, pp. L53–L57, 2010.

[162] Y. S. Yoon, H. S. Ahn, P. S. Allison, *et al.*. Cosmic-ray Proton and Helium Spectra from the First CREAM Flight. *The Astrophysical Journal*, vol. 728, 122, 2011.

[163] O. Adriani, G. C. Barbarino, G. A. Bazilevskaya, *et al.*. PAMELA Measurements of Cosmic-Ray Proton and Helium Spectra. *Science*, vol. 332, p. 69, 2011.

[164] M. Aguilar, J. Alcaraz, J. Allaby, *et al.*. Relative Composition and Energy Spectra of Light Nuclei in Cosmic Rays. Results from AMS-01. *ArXiv e-prints*, 2010.

[165] K.-H. Kampert, J. Kulbartz, L. Maccione, *et al.*. CRPropa 2.0 - A public framework for propagating high energy nuclei, secondary gamma rays and neutrinos. *Astroparticle Physics*, vol. 42, pp. 41–51, 2013.

[166] R. Alves Batista, M. Erdmann, C. Evoli, *et al.*. CRPropa 3.0 - a Public Framework for Propagating UHE Cosmic Rays through Galactic and Extragalactic Space. *ArXiv e-prints*, 2013.

[167] D. Caprioli, E. Amato, and P. Blasi. The contribution of supernova remnants to the galactic cosmic ray spectrum. *Astroparticle Physics*, vol. 33, pp. 160–168, 2010.

[168] L. O. Drury. Escaping the accelerator: how, when and in what numbers do cosmic rays get out of supernova remnants? *Mon. Not. R. Astron. Soc.*, vol. 415, pp. 1807–1814, 2011.

[169] Y. Ohira, R. Yamazaki, N. Kawanaka, *et al.*. Escape of cosmic-ray electrons from supernova remnants. *Mon. Not. R. Astron. Soc.*, vol. 427, pp. 91–102, 2012.

[170] K. M. Schure and A. R. Bell. From cosmic ray source to the Galactic pool. *Mon. Not. R. Astron. Soc.*, vol. 437, pp. 2802–2805, 2014.

[171] C. Yang, L. Zhang, and J. Wang. On the escape and propagation of high-energy protons near young supernova remnants. *Mon. Not. R. Astron. Soc.*, vol. 448, pp. 3423–3428, 2015.

[172] V. V. Pipin and A. G. Kosovichev. The Mean-field Solar Dynamo with a Double Cell Meridional Circulation Pattern. *The Astrophysical Journal*, vol. 776, 36, 2013.

[173] S. D. Center. The international sunspot number. webpage. International Sunspot Number Monthly Bulletin and online catalogue, Accessed: May, 2017.
URL `http://sidc.be/silso/datafiles`

[174] T. Wiengarten. Numerical modeling of plasma structures and turbulence transport in the solar wind. Ph.D. thesis, 2016.

Appendix

Cosmic ray shadow in November 2007 - 2016

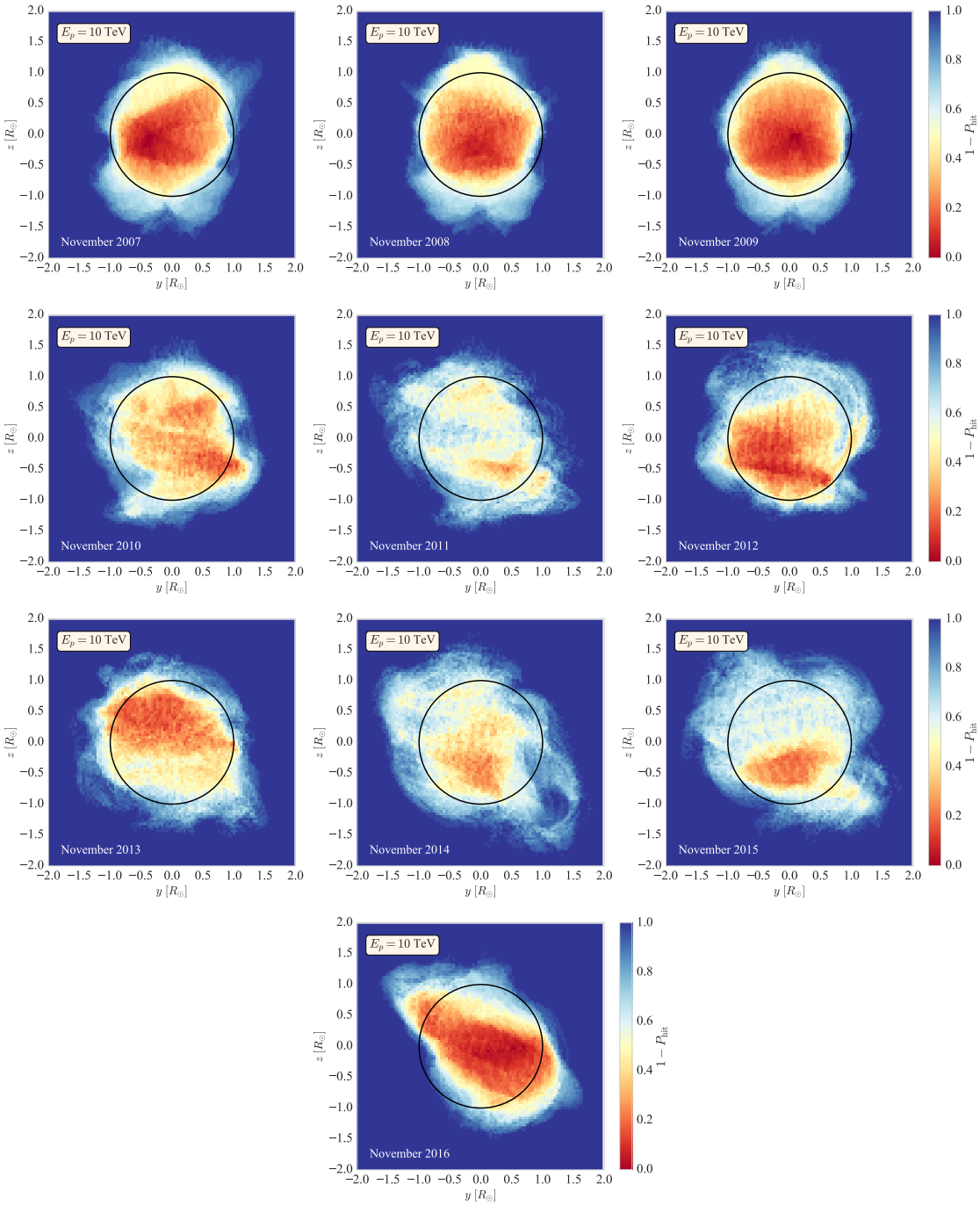

Figure 1: *Figure shows the variation of the cosmic ray Sun shadow at $E_{CR} = 10$ TeV from 2007 through 2016 in November.*

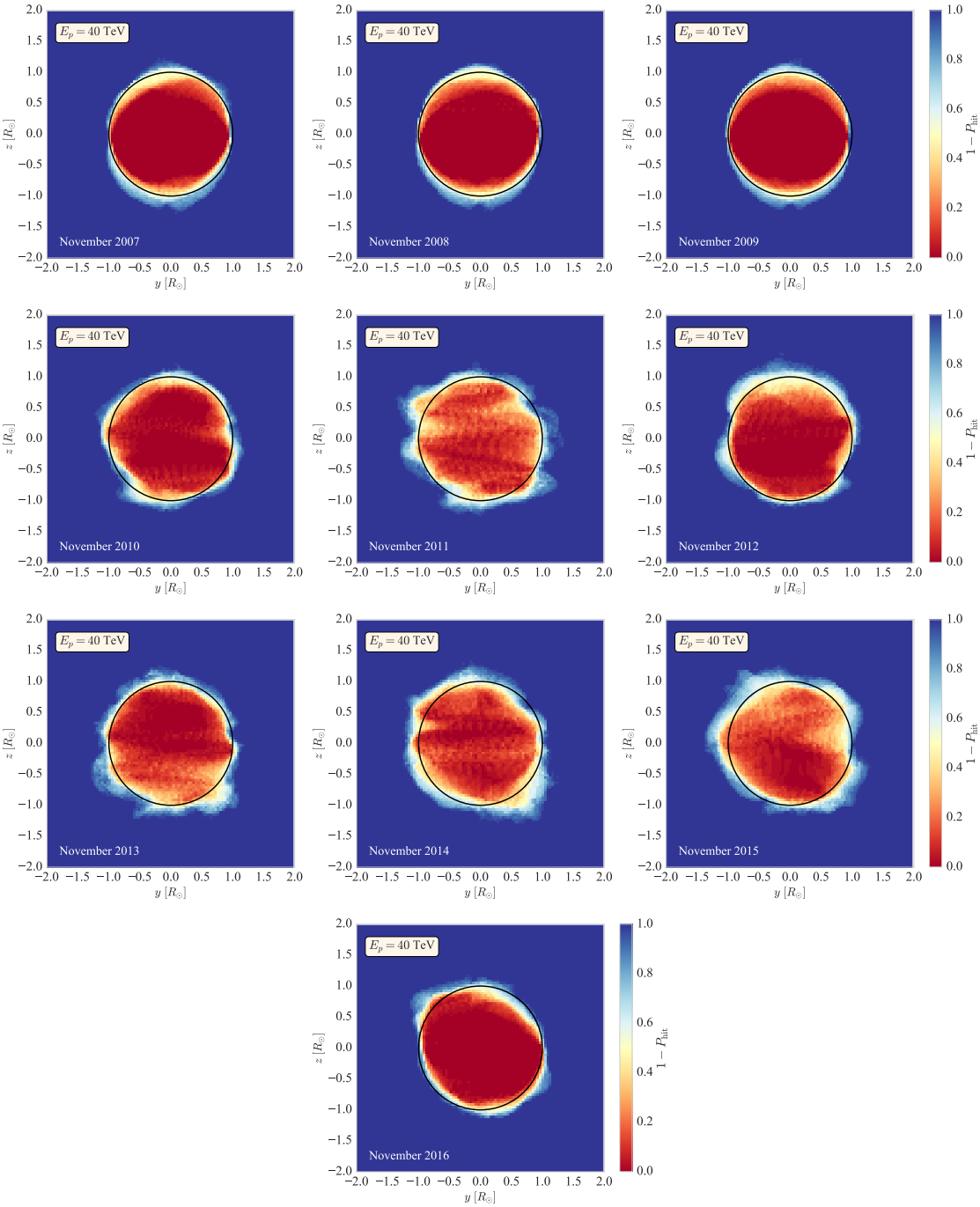

Figure 2: *Figure shows the variation of the cosmic ray Sun shadow at $E_{CR} = 40$ TeV from 2007 through 2016 in November.*

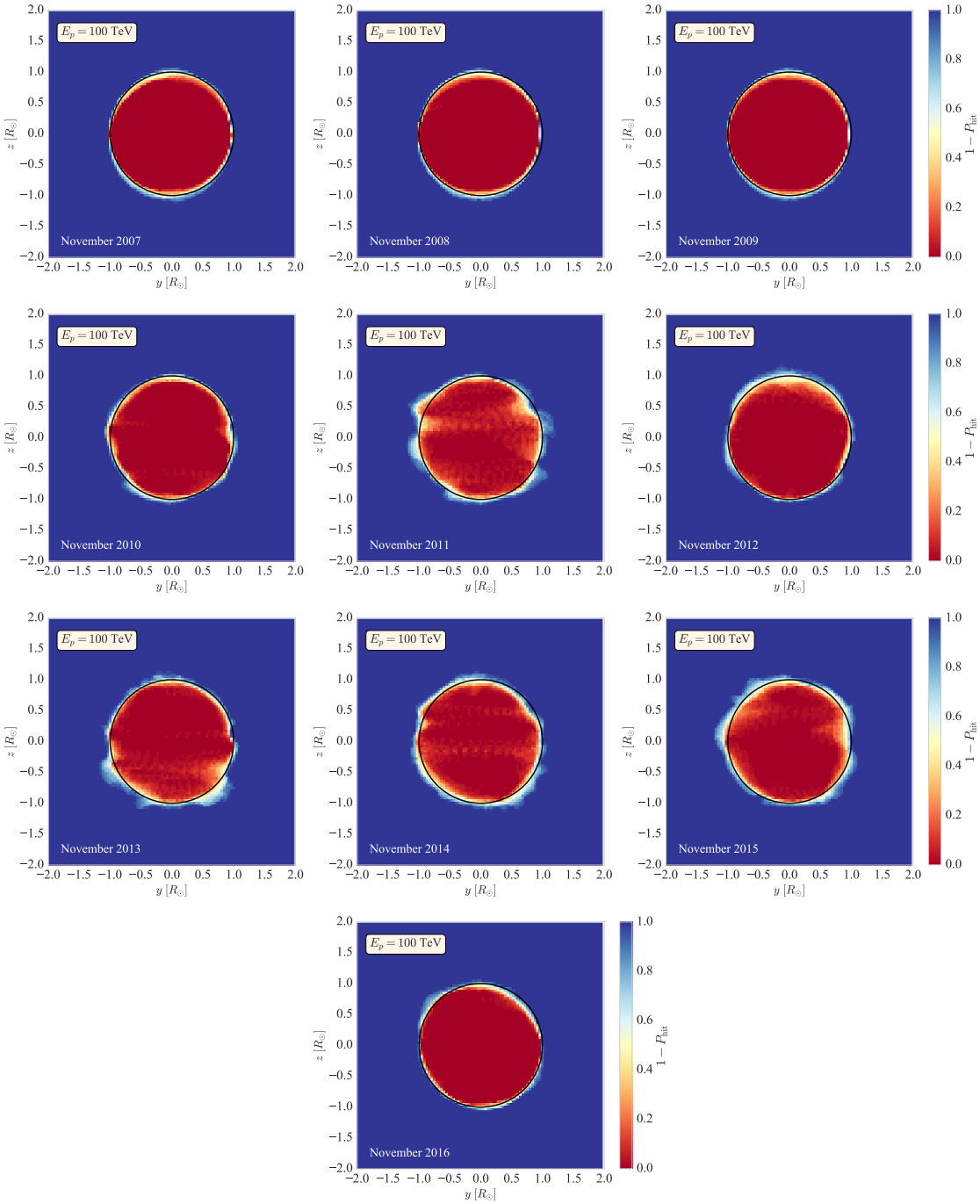

Figure 3: *Figure shows the variation of the cosmic ray Sun shadow at $E_{CR} = 100$ TeV from 2007 through 2016 in November.*

Cosmic ray shadow in January 2008 - 2017

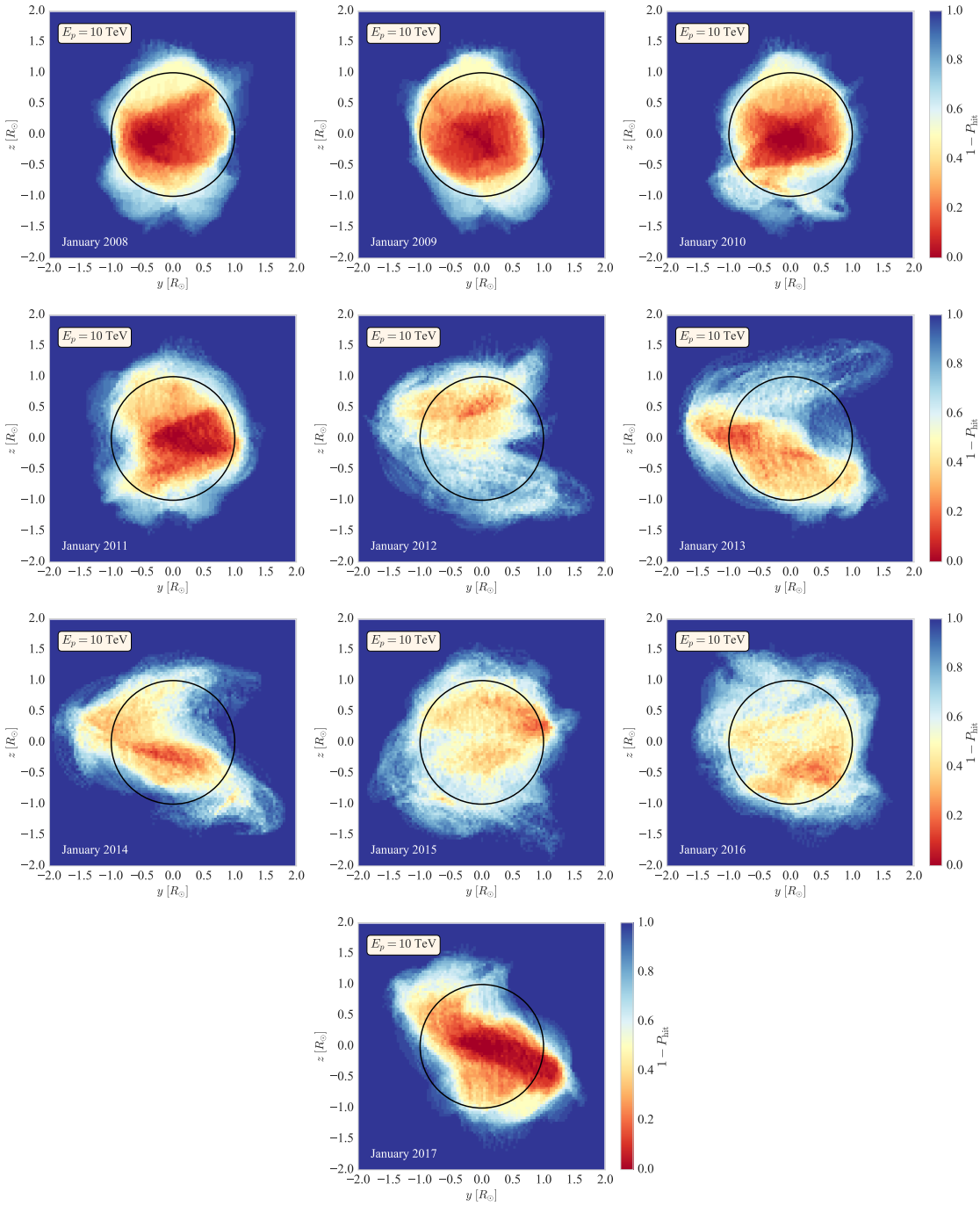

Figure 4: *Figure shows the variation of the cosmic ray Sun shadow at $E_{CR} = 10$ TeV from 2008 through 2017 in January.*

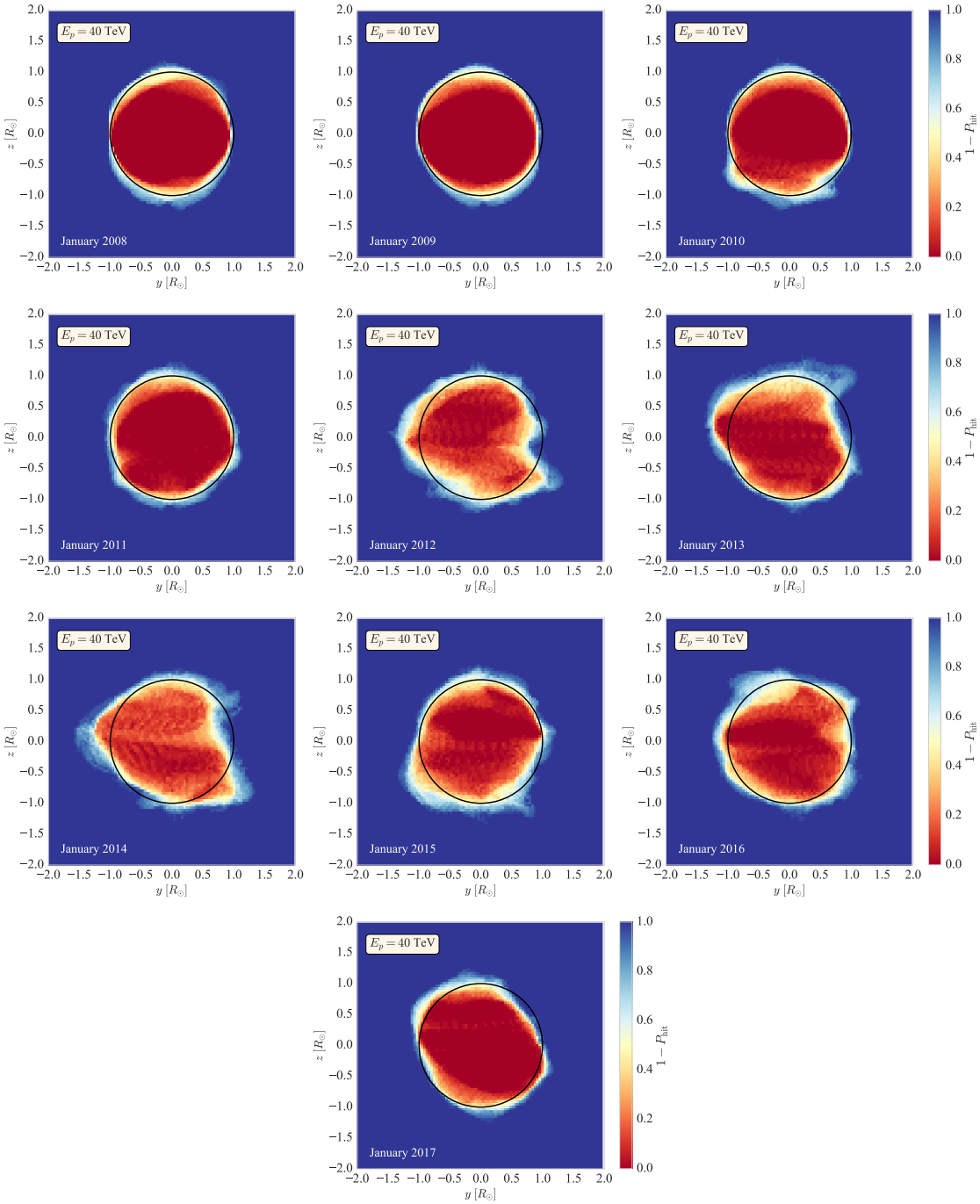

Figure 5: *Figure shows the variation of the cosmic ray Sun shadow at $E_{CR} = 40$ TeV from 2008 through 2017 in January.*

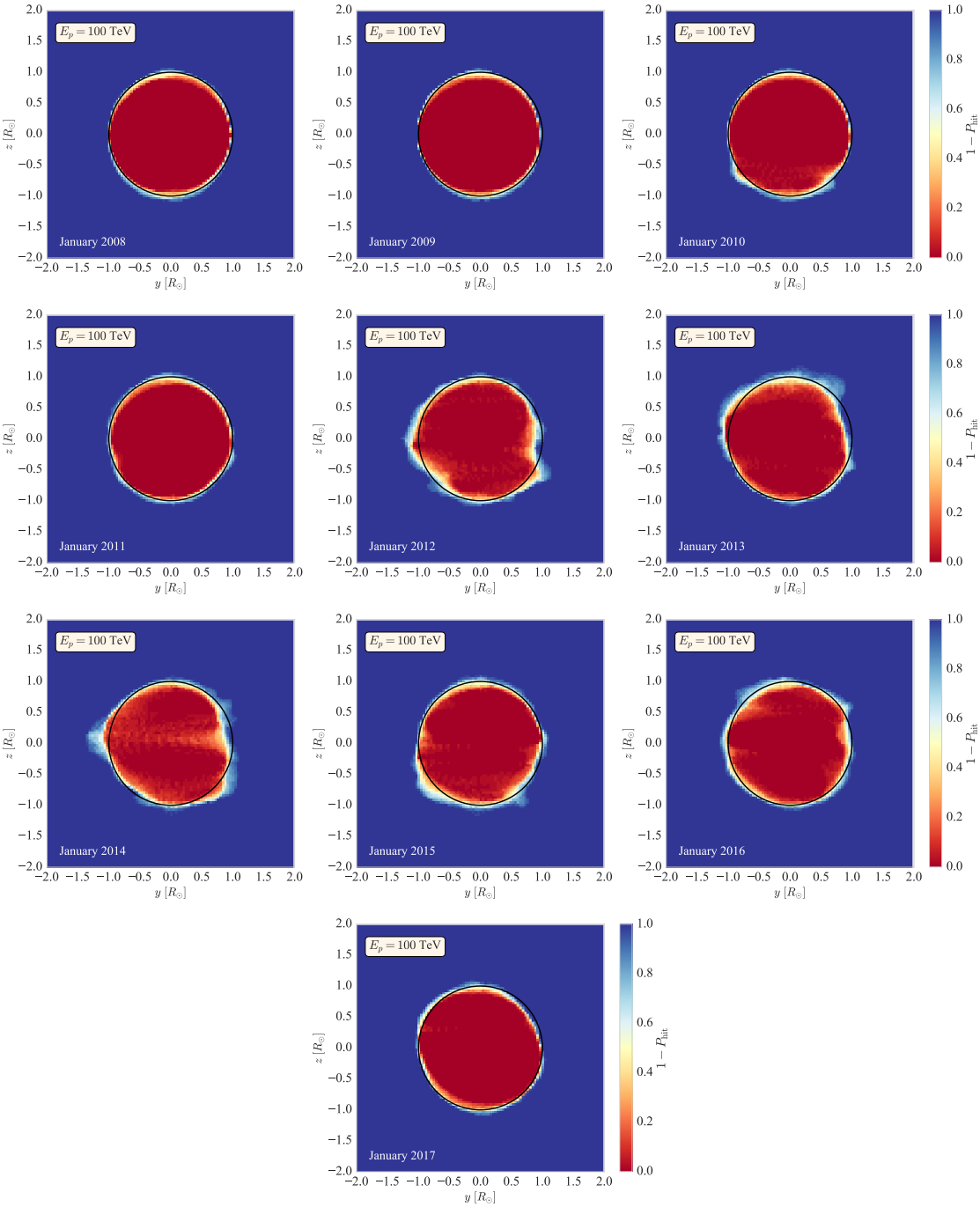

Figure 6: *Figure shows the variation of the cosmic ray Sun shadow at $E_{CR} = 100$ TeV from 2008 through 2017 in January.*

Cosmic ray shadow in February 2008 - 2017

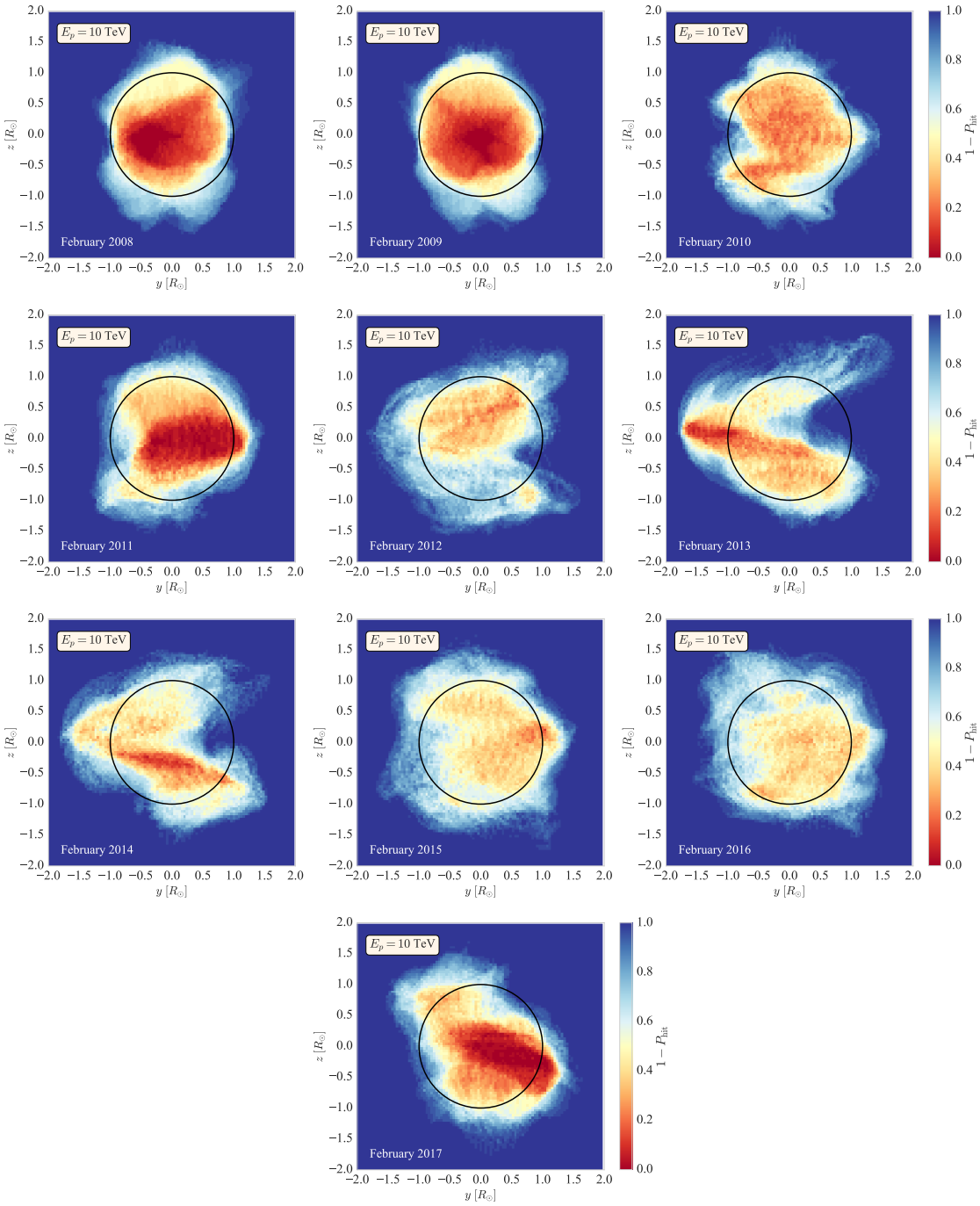

Figure 7: *Figure shows the variation of the cosmic ray Sun shadow at $E_{CR} = 10$ TeV from 2008 through 2017 in February.*

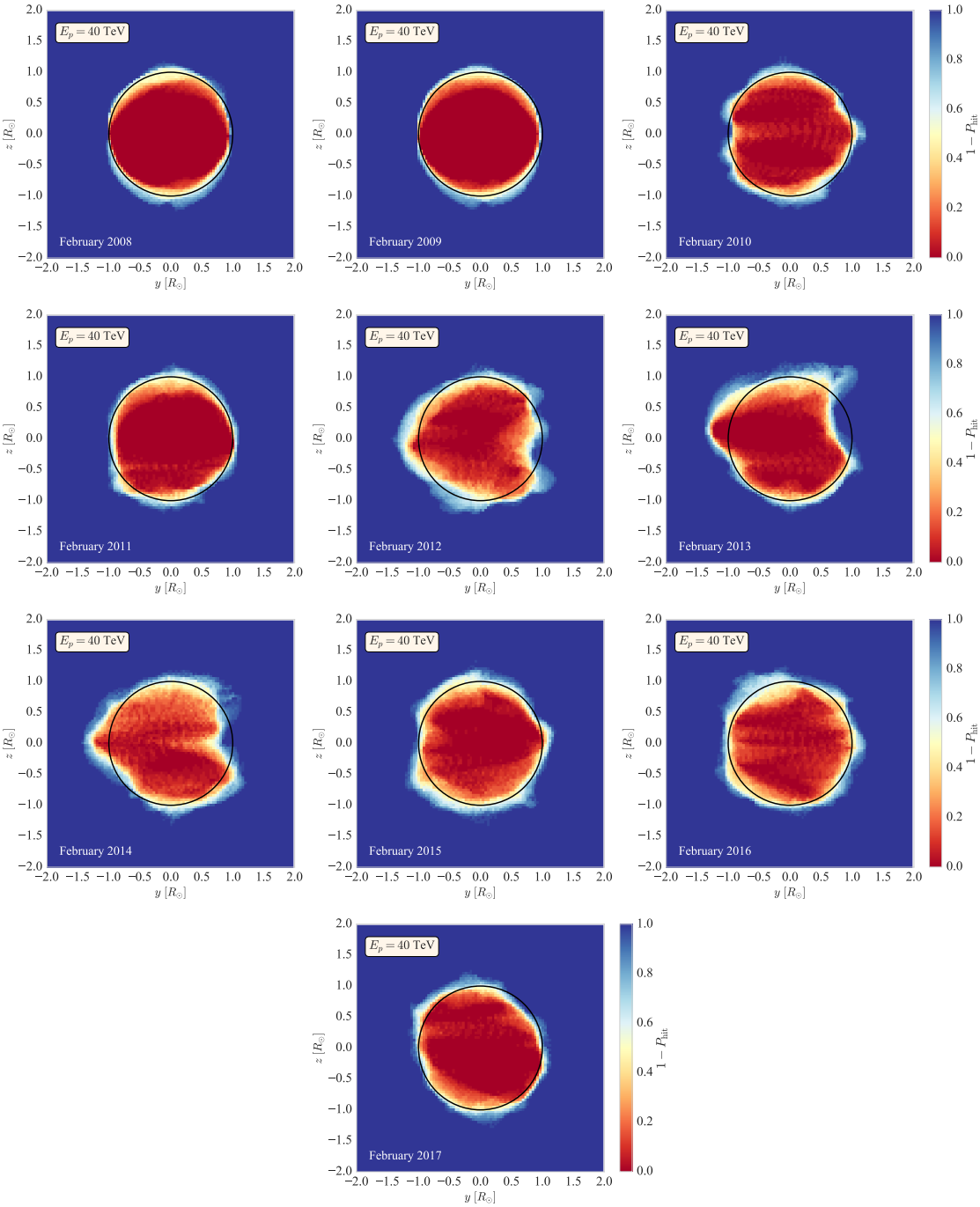

Figure 8: *Figure shows the variation of the cosmic ray Sun shadow at $E_{CR} = 40$ TeV from 2008 through 2017 in February.*

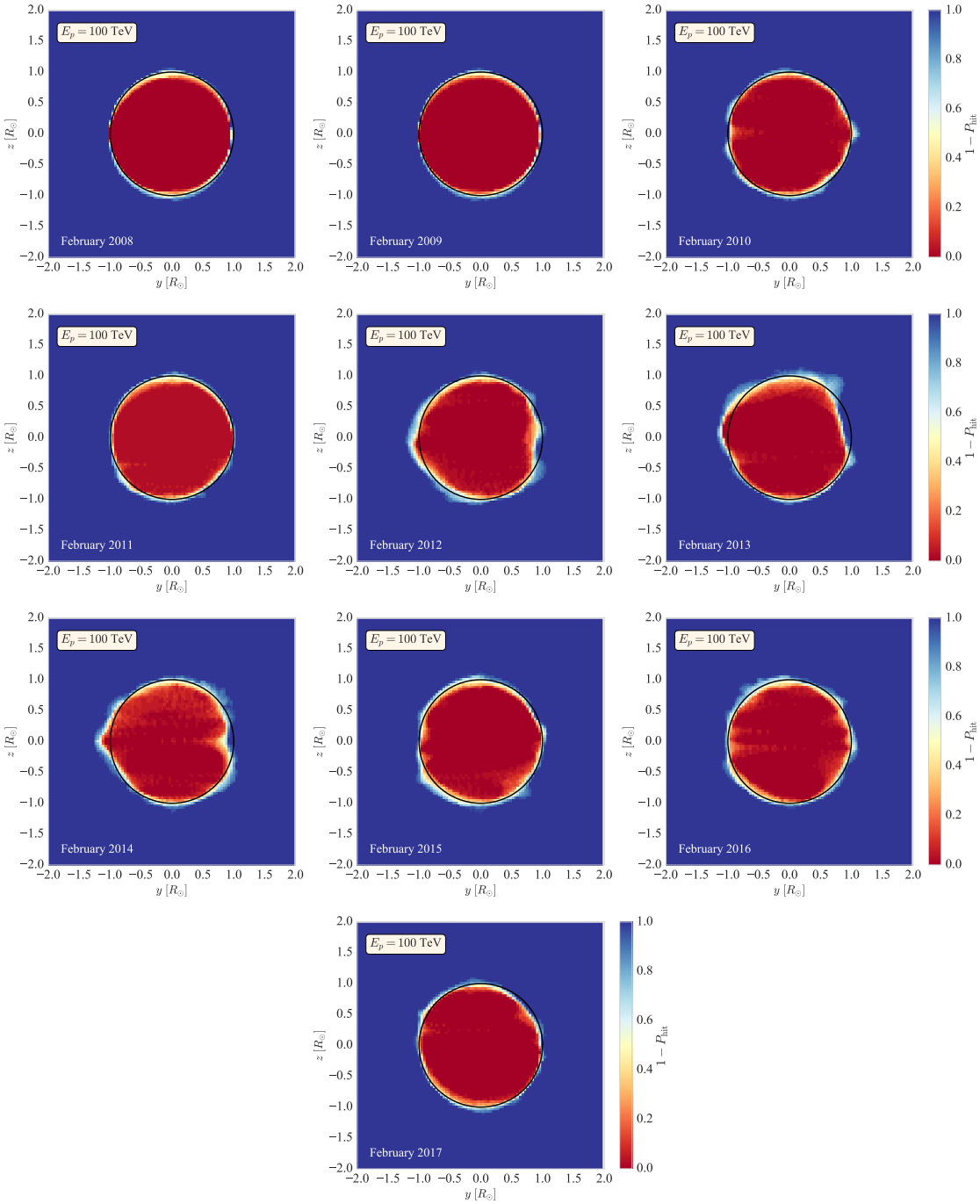

Figure 9: *Figure shows the variation of the cosmic ray Sun shadow at $E_{CR} = 100$ TeV from 2008 through 2017 in February.*

Deficit from November through February

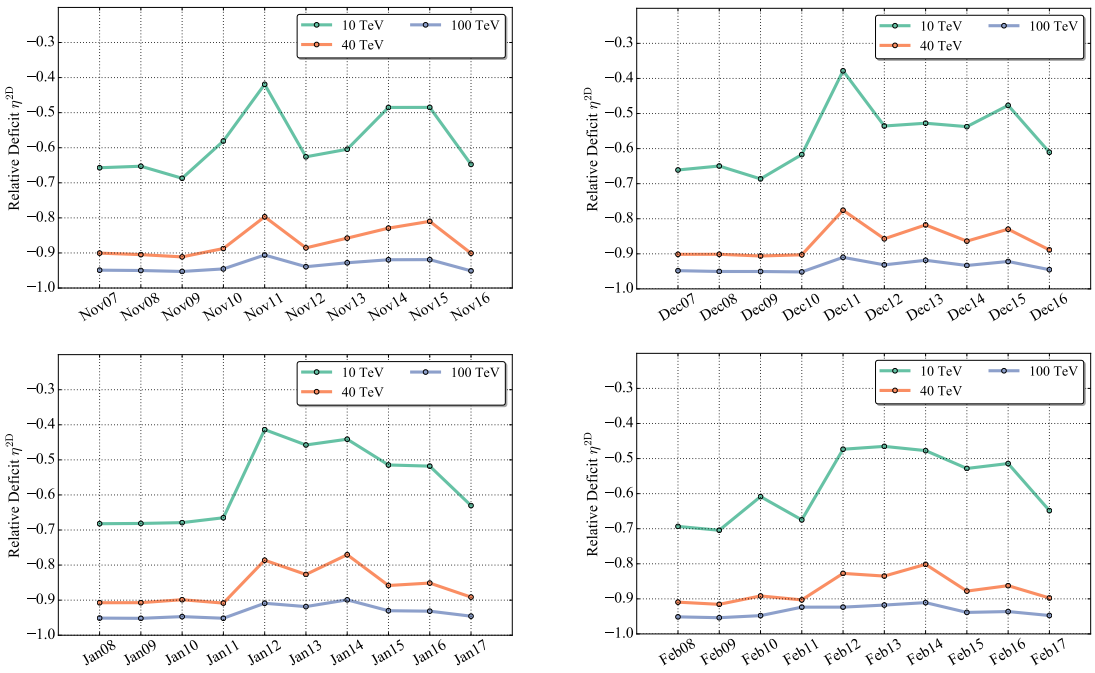

Figure 10: *Figure shows the individual total deficit values resolved for each month from 2007 through 2016 (November and December), and 2008 through 2017 (January and February), respectively.*

Total Absorption from November through February

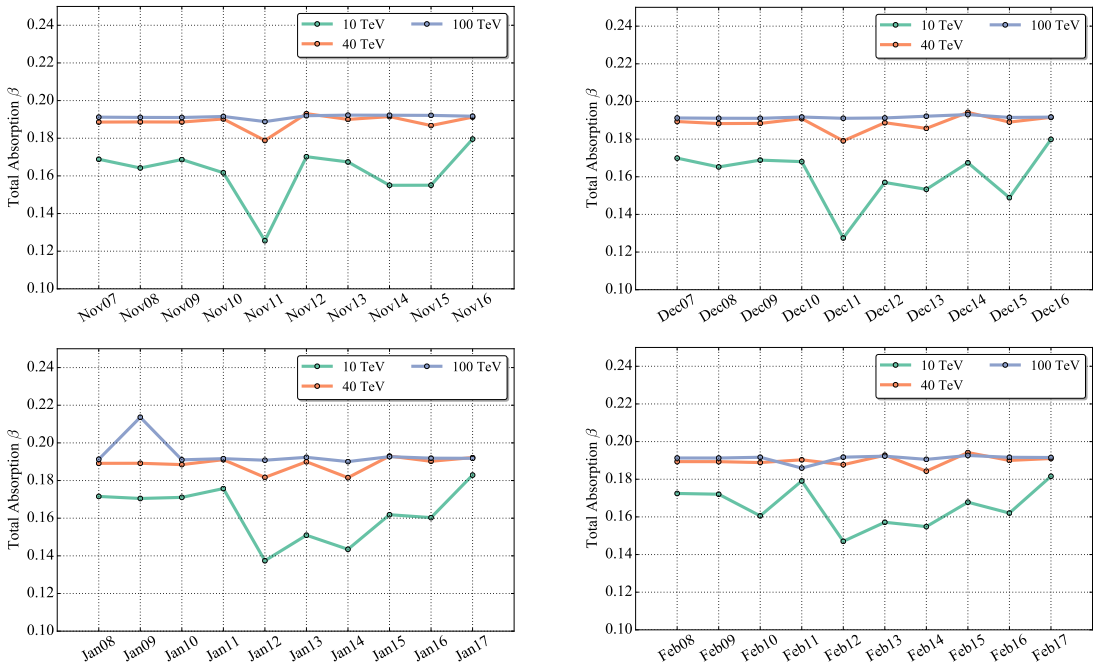

Figure 11: *Figure shows the individual absorption rates resolved for each month from 2007 through 2016 (November and December), and 2008 through 2017 (January and February), respectively.*

One-dimensional analysis: November 2007 - 2016

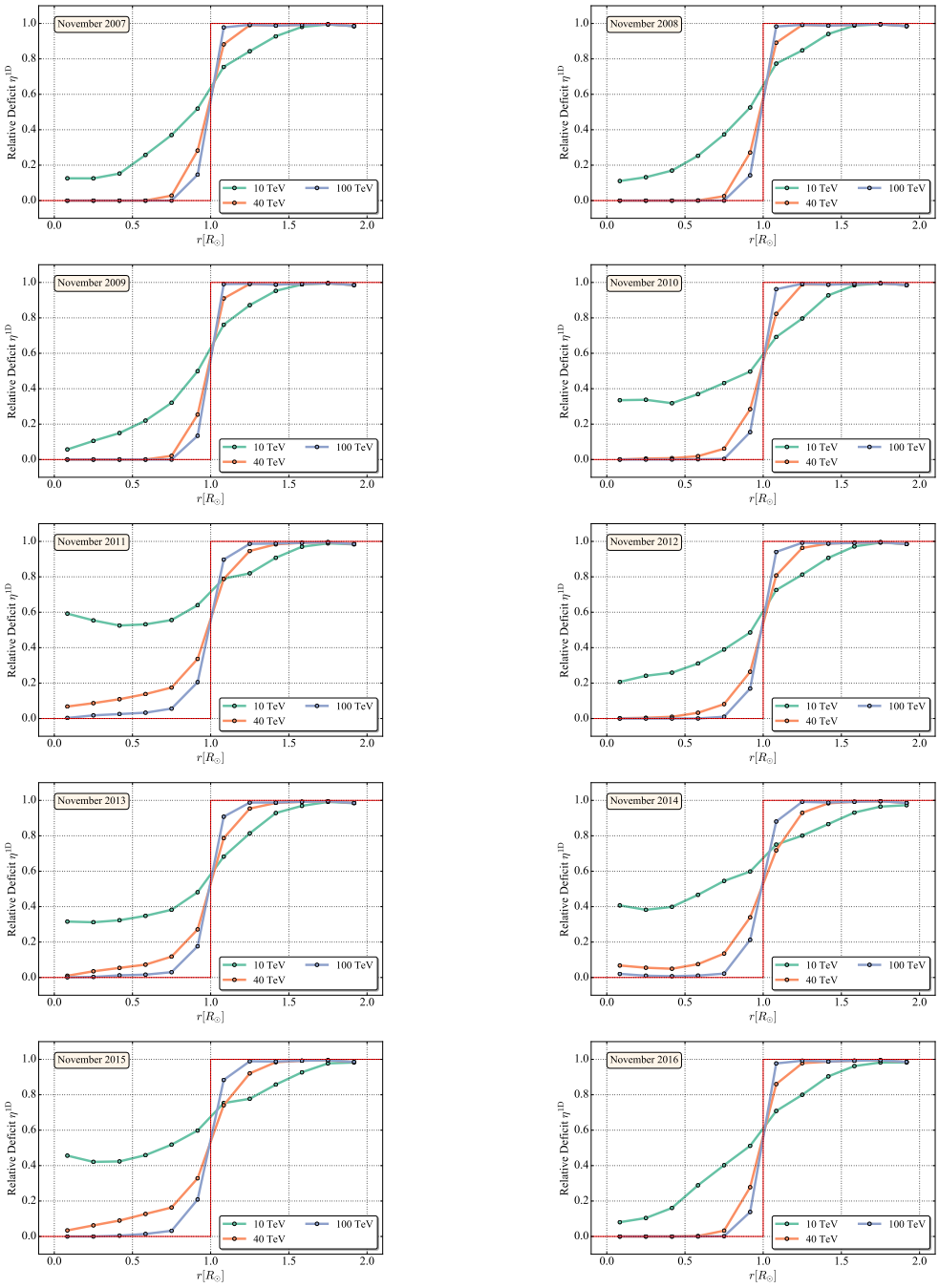

Figure 12: *Figure shows the one-dimensional analysis. The bins are arranged concentric around the center of the Sun.*

One-dimensional analysis: December 2007 - 2016

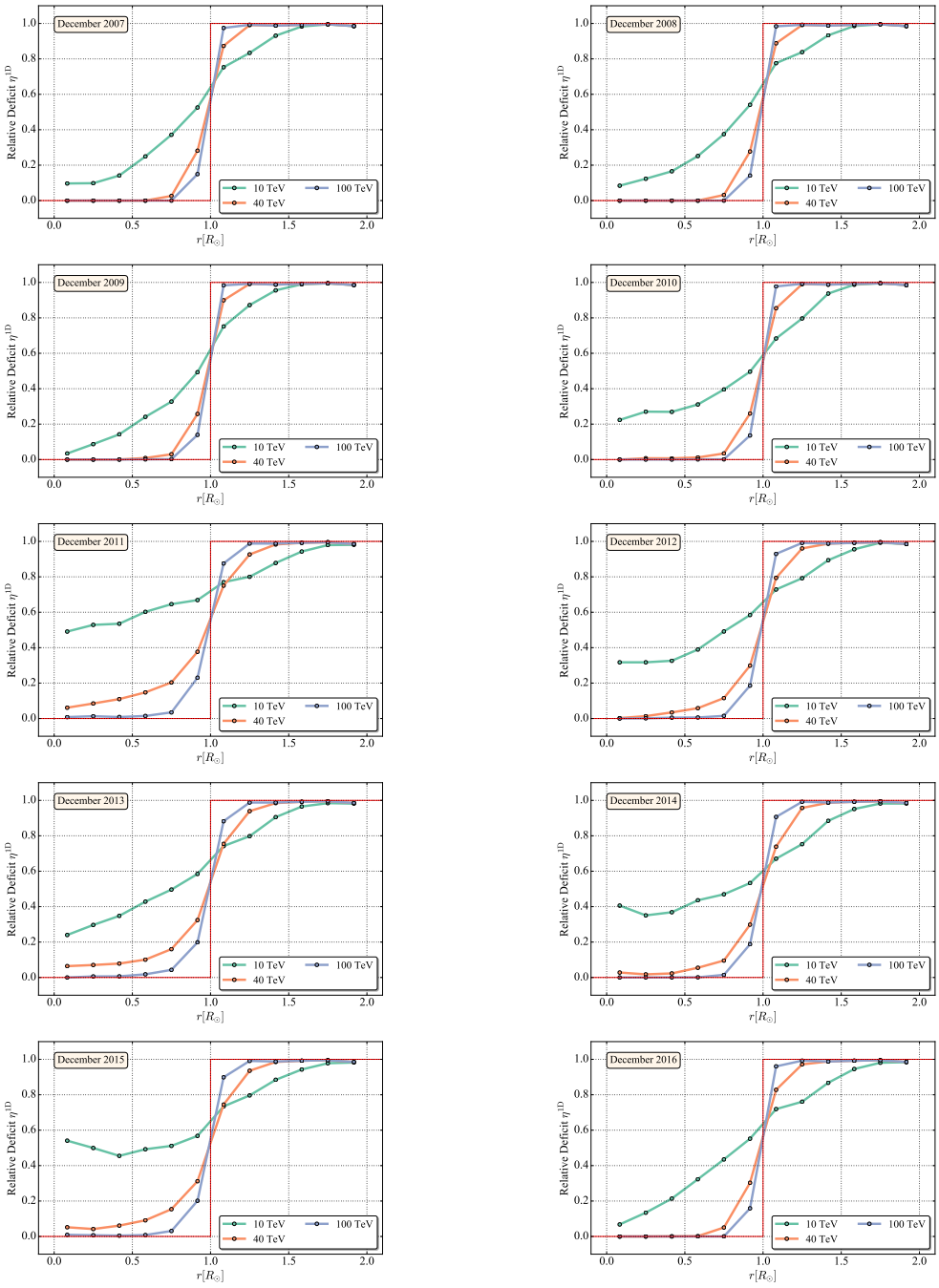

Figure 13: *Figure shows the one-dimensional analysis. The bins are arranged concentric around the center of the Sun.*

One-dimensional analysis: January 2008 - 2017

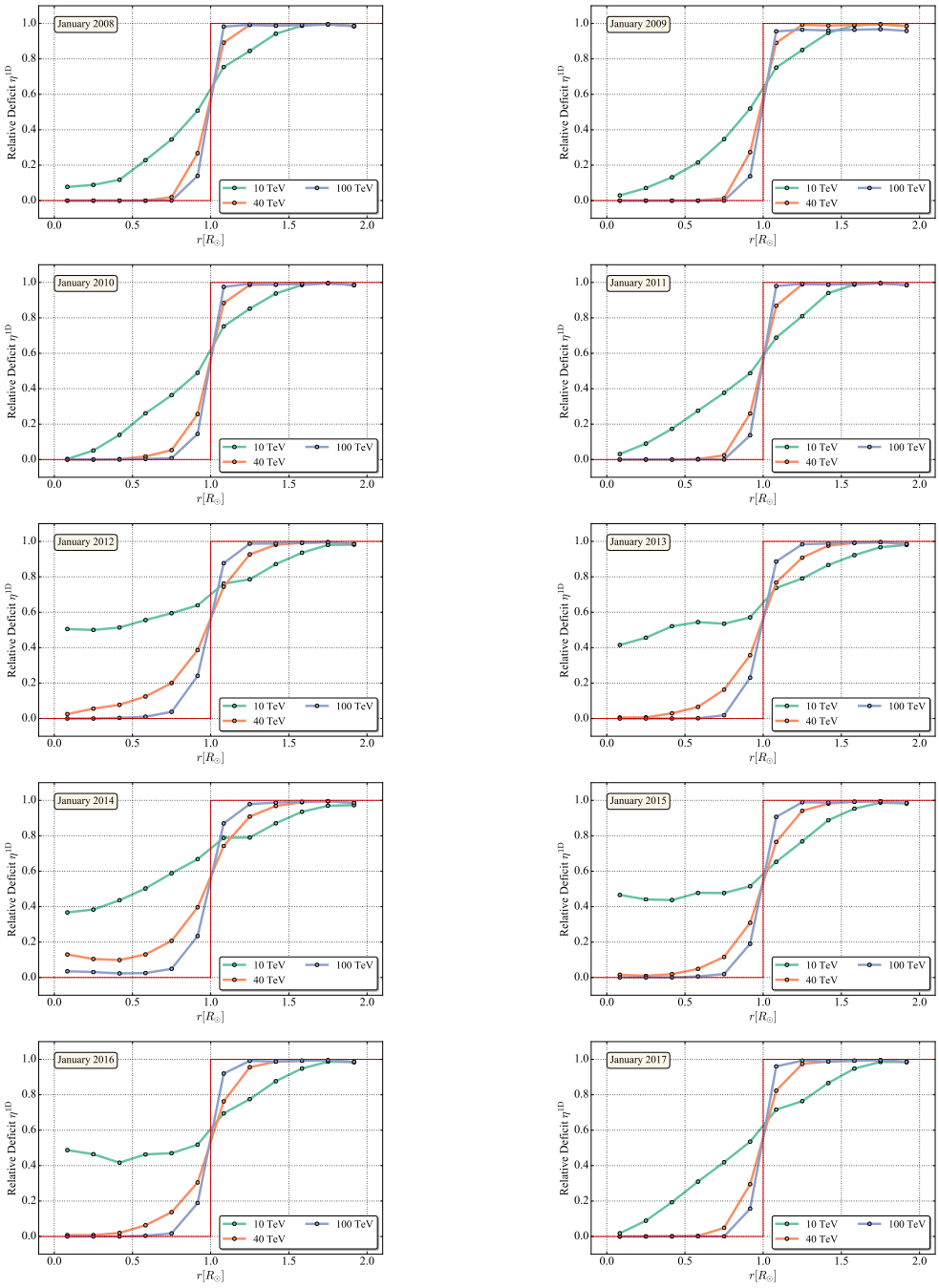

Figure 14: *Figure shows the one-dimensional analysis. The bins are arranged concentric around the center of the Sun.*

One-dimensional analysis: February 2008 - 2017

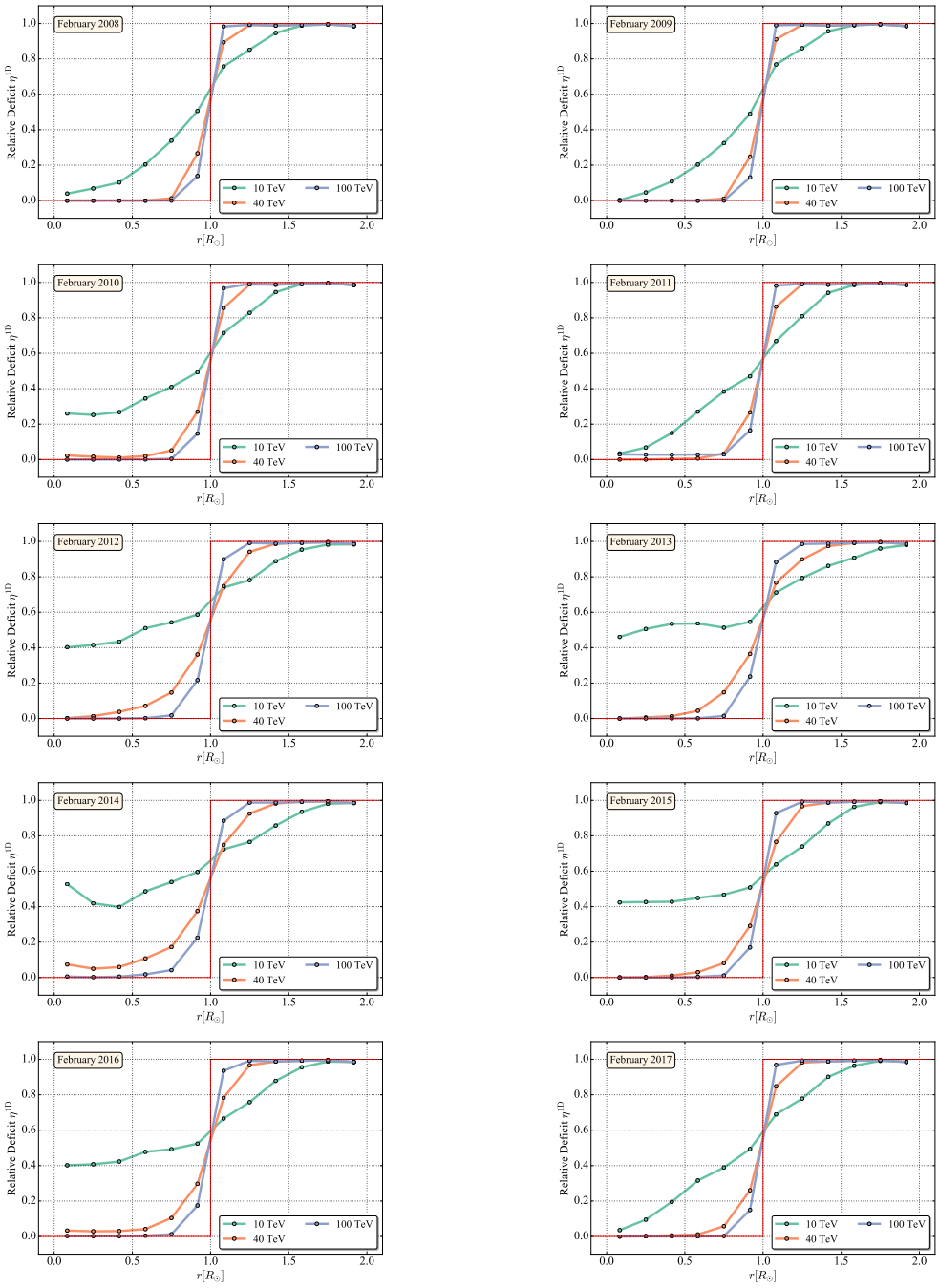

Figure 15: *Figure shows the one-dimensional analysis. The bins are arranged concentric around the center of the Sun.*